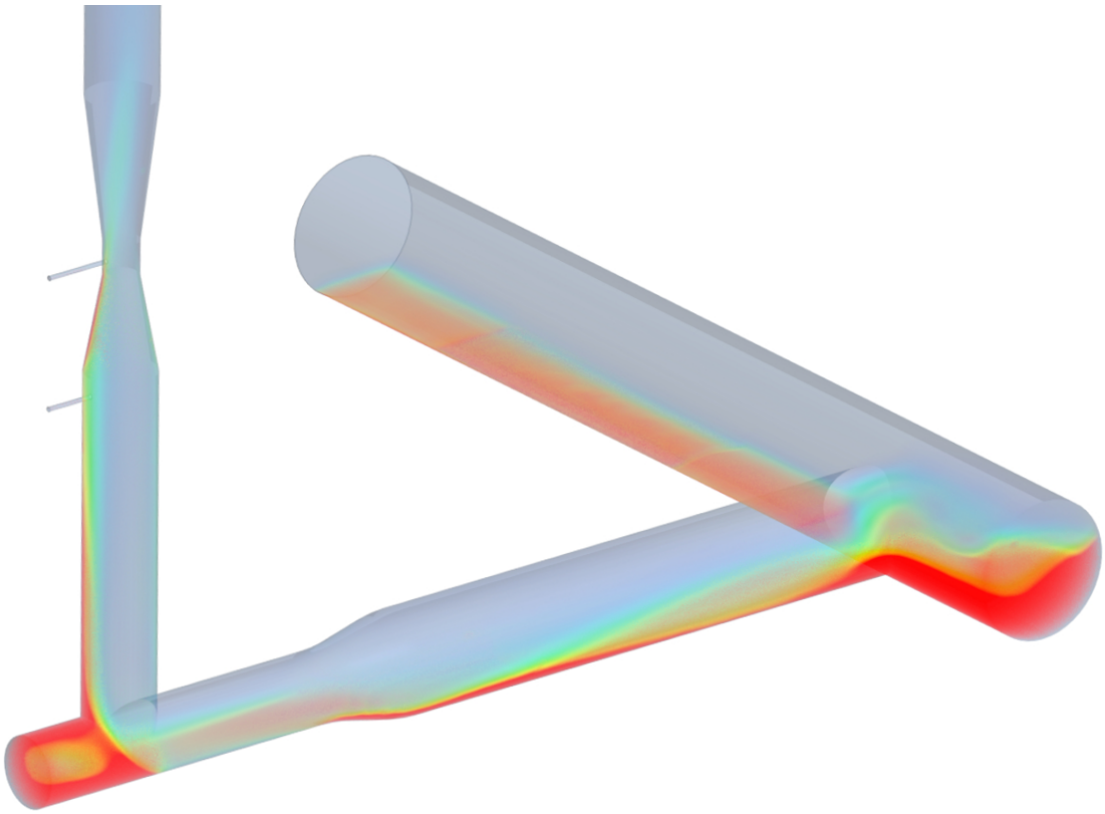

CFD-Based Sensitivity Study of Flow and Design Parameters in Multiphase Flow Meters

Analyzing the Impact of Variable Conditions on Homogeneity and Measurement Accuracy

Master's thesis in Sustainable Energy Systems and Mobility Engineering

Elias Nilsson & Maria Vassilev

DEPARTMENT OF MECHANICS AND MARITIME SCIENCES
CHALMERS UNIVERSITY OF TECHNOLOGY
Gothenburg, Sweden 2025
www.chalmers.se

Master's thesis 2025

CFD-Based Sensitivity Study of Flow and Design Parameters in Multiphase Flow Meters

Analyzing the Impact of Variable Conditions on Homogeneity and Measurement Accuracy

ELIAS NILSSON, MARIA VASSILEV

CHALMERS
UNIVERSITY OF TECHNOLOGY

Department of Mechanics and Maritime sciences
Division of Fluid Dynamics
Chalmers University of Technology
Gothenburg, Sweden 2025

CFD-Based Sensitivity Study of Flow and Design Parameters in Multiphase Flow Meters
Analyzing the Impact of Variable Conditions on Homogeneity and Measurement Accuracy
ELIAS NILSSON, MARIA VASSILEV

Supervisor: Martin Johannes Orphanides, Specialist CFD Engineer
Examiner: Henrik Ström, Department of Mechanics and Maritime Sciences

Master's Thesis 2025
Department of Mechanics and Maritime sciences
Division of Fluid Dynamics
Chalmers University of Technology
SE-412 96 Gothenburg
Telephone +46 31 772 1000

Cover: Liquid distribution in a pipe section

Typeset in LaTeX
Printed by Chalmers Reproservice
Gothenburg, Sweden 2025

CFD-Based Sensitivity Study of Flow and Design Parameters in Multiphase Flow Meters
Analyzing the Impact of Variable Conditions on Homogeneity and Measurement Accuracy
NILSSON ELIAS, MARIA VASSILEV
Department of Mchanics and Maritime Sciences
Chalmers University of Technology

Abstract

In subsea oil- and gas applications, multiphase flow meters (MPFM) are used to measure volumetric flow rates of oil, gas and water produced from a well, without first separating the phases. When well productions decline the flow may become unstable, requiring additional controls. In these cases MPFMs are useful instruments to detect well instability, blockages and disturbances so that the well can be controlled and stabilized in real time. Variations in flow regime and homogeneity in the Venturi-based MPFM may affect the accuracy of measured volume flow. Additionally, understanding slip velocity between phases is crucial for formulating an accurate slip model to compute phase volume flow rates.

In this project, the sensitivity of the MPFM to flow- and geometrical parameters is studied by modeling and simulating the MPFM using CFD. This gives insight into how MPFM design and operating conditions influence measurement certainty on a macroscopic scale, while also allowing for the investigation of smaller scale phenomena. Time-averaged mean values and periodic behaviors of the flow parameters are evaluated to give insight into the flow behavior and the MPFM sensitivity to flow and design parameters. The homogeneity and mixing of the flow before entering the MPFMs is evaluated, to understand how operating conditions and geometry changes affect the flow characteristics considering MPFM accuracy. Additionally, a suitable CFD modeling technique is found to aid in the design and development of future MPFMs. The modeling technique is evaluated in terms of accuracy, quality and computational expense.

In this study, a suitable modeling method was identified using Eulerian Multiphase models. These models have high accuracy and is effectively capturing the flow behavior while being computationally efficient. The slip-ratios evaluated showed that for increased pressure and viscosity the liquid film, dispersed, and overall slip decreased while for design changes the slip had more mixed results. The sensitivity study revealed that the MPFM's sensitivity to geometrical parameters, such as blind-T depth and vertical entrance length, was minimal. Operating conditions, especially pressure and liquid viscosity, play a major role in shaping the flow regime and phase mixing. These factors can significantly affect MPFM accuracy if they are not properly accounted for in the interpretation models.

Keywords: multiphase flow metering, multiphase, computational fluid dynamics, sensitivity study, Eulerian multiphase

Acknowledgements

The authors would like to extend their gratitude to Rolf Rustad, Harald Solheim and Martin Orphanides for sharing their expertise with us and for their relentless support and guidance. Your interest in this project has been really inspiring and very motivating for us. The authors have greatly appreciated the close collaboration.

Our gratitude is also extended to all fellow engineer's at Company, for the support and helpful advise. Your counsel and encouragement has helped us tremendously in overcoming the biggest challenges in this project. Special thanks is also extended to Anton Riström, CFD Department Manager at Company, for facilitating this project and for his encouragement and care.

The authors also want to thank the Examiner Henrik Ström, Professor at the Division of Fluid Dynamics at the Department of Mechanics and Maritime Sciences at Chalmers University of Technology, for his support and interest in this project.

List of Acronyms

Below is the list of acronyms that have been used throughout this thesis listed in alphabetical order:

API	American Petroleum Institute
CAD	Computer Aided Design
CFD	Computational Fluid Dynamics
CPU	Central Processing Unit
DFT	Discrete Fourier Transform
EMP	Eulerian Multiphase
FFT	Fast Fourier Transform
GVF	Gas Volume Fraction
ID	Inner Diameter
LVF	Liquid Volume Fraction
MPFM	Multiphase Flow Meter
PVT	Pressure-Volume-Temperature Diagram
RANS	Reynolds-Averaged Navier-Stokes
RMS	Root Mean Square
SST	Shear Stress Transport
SR	Slip Ratio
VEL	Vertical Entrance Length
URANS	Unsteady RANS

Nomenclature

Below is the nomenclature of indices, sets, parameters, and variables that have been used throughout this thesis.

V	Velocity
p	Pressure
σ	Surface Tension
T	Temperature
ρ	Density
g	Gravitational Acceleration
h	Height
N	Count Rate
α	Hold-Up
D	Diameter
μ	Mass Attenuation Coefficient
Q	Volume Flow Rate
A	Pipe Cross-Sectional Area
C_f	Form Factor
C_d	Discharge Coefficient
y	Absolute Distance to Wall
y^+	Dimensionless Distance
u_T	Friction Velocity at Nearest Wall
ν	Kinematic Viscosity
ω	Frequency
t	Time
N	Number of Samples
$\dot{m}$	Massflow Rate

Contents

List of Figures

List of Tables

1
Introduction

In this section, the subject matter of this thesis is introduced. Additionally the aim and scope of this project is elaborated.

1.1 Background

In subsea oil- and gas applications, there are many cases in production where the use of multiphase flow meters (MPFM) are very beneficial if not necessary [1]. MPFMs are used to measure volumetric flow rates of oil, gas and water produced from a well, without first seperating the phases. An MPFM measures produced volumetric flow rates of oil, gas and water using a number of different sensors, such as Venturi meters, salinity sensors and gamma-ray attenuation detectors. When well productions decline the flow may become too unstable, requiring additional controls. In this case an MPFM is a useful instrument to detect well instability so that the well can be controlled and stabilized. For long, subsea transport lines an MPFM is a well suited tool to monitor the flow in real time, which is important in order to identify potential blockages or disturbances.

In addition, the MPFM can be used as an allocating meter to reconcile oil, gas and water measurements for all inlets and outlets in the process network. This data can be used in order to prevent economic consequences due to wrongful allocation with regards to taxes and custody transfer. This technique can also be applied when multiple operators use the same processing facility, ensuring accurate financial allocation. Lastly, the MPFM is good for flow assurance and production optimization. Since the meter can deliver real time data of the composition in the production flow, it generates valuable information for the management and for the optimization of the production [2].

Today a typical MPFM piping set-up consists of a horizontal pipe with a blind-T combined with a vertical pipe followed by Venturi section, see Figure 1.1. The blind-T has dual purpose, it mixes the phases and homogenizes the flow before the Venturi section, but it is also used to mount a salinity sensor. The blind-T will normally accumulate liquids, making it an optimal position to place a salinity sensor.

In the Venturi section, a pressure differential gauge as well as a gamma-ray system that measures phase hold-up are mounted. The output from these sensors is post-processed in order to find the mass flow of each phase. Ideally the flow in the

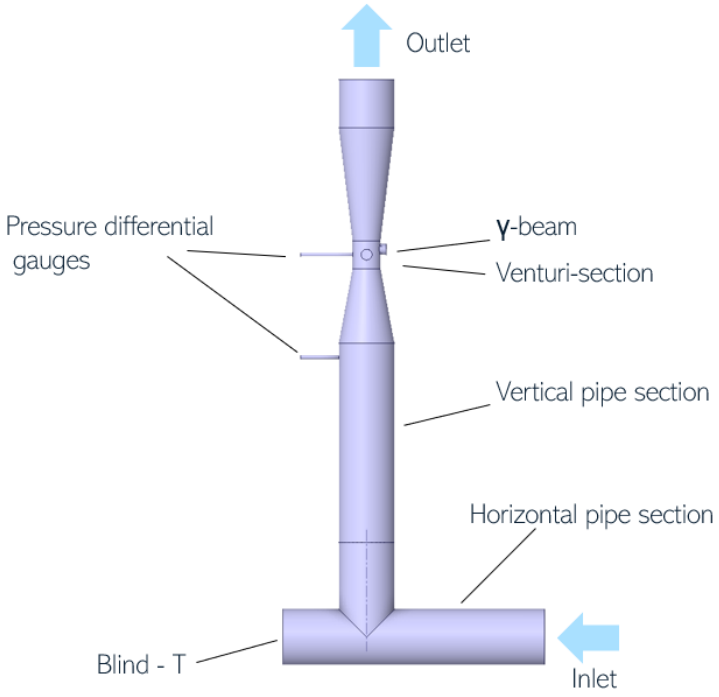

Figure 1.1: Piping in proximity to MPFM

Venturi section of an MPFM should be homogeneous to allow the MPFM to accurately measure phase hold-up [3]. In this context, homogeneous flow means that the phases are well mixed together and have a uniform distribution in the Venturi section. However in practice the flow is not guaranteed to be homogeneous, which may influence uncertainty in the MPFM measurements. The uncertainty of measured phase mass flows has been observed to be dependent on a variety of factors, including multiphase flow topology as well as geometrical parameters. This in turn has an effect on the final phase mass flow measurements.

Computational fluid dynamics (CFD) is an tool used for simulating fluid flows, which is often used in research and development in engineering applications. In contrast to experimental tests, CFD simulations allow information to be extracted from the entire test domain, not just from individual sensors. This can give insight into the simulated flow on a macroscopic scale, while also allowing for the investigation of small scale phenomena. In summary, the CFD tool allows for more freedom when studying fluid flows compared to experimental methods, and is oftentimes comparatively cheaper.

1.2 Societal, Ethical, and Ecological Aspects

The development and further implementation of multiphase flow meters will have an impact on both environment and society. At this time the main application for MPFMs is in the oil- and gas industry. It is very well established that the use of

fossil fuels has a major environmental impact, and the general consensus is that they should be phased out in order to reduce the negative climate impact of fossil fuel combustion. However, as many societal functions are completely dependent on the use of oil- and gas it is thus of high importance that there is continuous research to ensure that the oil-and gas industry remains safe and efficient while also implementing the work to reduce their climate impact.

From an ecological perspective, the MPFM is considered a more sustainable way of measuring multiphase flows instead of using traditional separation processes. This is due to the MPFM eliminating the need for an additional separation of the phases, which is an energy intensive process. The separation of phases has a higher footprint due to construction materials required for the equipment, and it also requires cooling water. In addition to this the separation process consist of several moving parts such as turbines and pumps which are sensitive to failure resulting in increased downtime and higher maintenance costs [4].

1.3 Problem Description

MPFMs are sensitive to operating conditions which may result in uncertainty in measurements [1]. Typically it is also assumed that the influence of the geometry upstream of the MPFM is negligible. However, it is currently not well understood how flow and design parameters influence the fidelity of MPFM measurements, making the validity of this assumption uncertain. The reliability of MPFMs is of great importance in susbea applications. Understanding how the flow regimes influence MPFM measurement accuracy will allow for these instruments to be developed and improved further. This will in turn improve performance of MPFMs, allowing for better control and optimized well production.

Computational fluid dynamics (CFD) is a well established and understood method to simulate single phase flows. However, simulating multiphase flows in CFD is a comparatively young discipline, and there are constantly new advancements in the field. There is a multitude of methods available with different strengths and weaknesses for different flow regimes, and in regards to what information can be extracted from them. It is therefore of great importance how multiphase flows are modeled and simulated, in order to get correct and valuable results.

In this specific application, it is unclear how to best model and simulate flows in and around the MPFM. Currently the most reliable method to evaluate the performance of MPFMs is experimental. This is problematic, since simulations can provide valuable information about a flow that complements measurements from empirical testing. Simulating is a comparatively cheaper method than experimental testing, meaning that if a good simulation method is found the development cost of MPFMs can be reduced. Additionally, in a simulation information can be extracted from anywhere in the domain, in contrast to finite experimental measurement points.

This gives valuable information and understanding about the overall behavior of the flow. Having a good method to simulate the flow will therefore aid in the future development of MPFMs.

1.4 Purpose

This study will continue to develop knowledge and investigate MPFM sensitivity to geometrical parameters and operating conditions. The aim is to evaluate how different flow regimes and geometrical parameters impact the MPFM precision and accuracy. The purpose of this project is therefore to research, analyze and evaluate parameters in regards to design and flow regime that may have an influence on the accuracy of the MPFM measurements. In this study, the slip between the phases is also investigated.

In addition, the purpose is also to find a suitable method to model and simulate multiphase flows typically encountered in an MPFM application using the Eulerian multiphase modeling approach (EMP). Here the aim is to find a good balance between the cost and fidelity of the simulation, such that it can also be applied to other operating conditions than those studied in this project and for further studies in this field.

1.4.1 Scope

This study is completed as a Master's Thesis at Chalmers University of Technology, in collaboration with an industrial partner referred to as "Company" in this report. In this study the flow regime of interest is wet gas, i.e. high gas volume fraction (GVF) flow regimes. A sensitivity study will be completed to evaluate changes in pressure and liquid viscosity as well as geometrical parameters, specifically vertical entrance length and blind-T depth. Additionally, the MPFM's sensitivity to the orientation of the gamma-ray system will be examined, as well as the interphase slip.

1.4.2 Research Questions

- How does upstream pipe geometry influence MPFM accuracy? Design parameters such as vertical entrance length, blind-T depth and gamma-ray system orientation are of interest.
- How does operating conditions influence MPFM accuracy? Parameters such as viscosity and pressure are of interest.
- What is a suitable method to model the multiphase flow in and around an MPFM in CFD using EMP? How accurately can it be modeled?
- What interphase slip can be observed in the flow around an MPFM?

1.4.3 Limitations

The project is initiated second week of January, until end of May 2025. The aim of this project is not to study the MPFM technology in itself, but rather the flow measured by the MPFM in the Venturi section. To be able to complete this study within the time frame some limitations and simplifications have been applied. First of all, any heat exchange between the MPFM, piping, process fluid and surrounding seawater is neglected. In practice, an MPFM typically measures volume flows of 3 phases with oil, water and gas. For this study, this is simplified to a two phase problem with gas and liquid. The liquid phase will either have properties typical of black oil extracted from a well, or water. Some parameters in the pipe design upstream of the MPFM will remain constant. The constant parameters are the pipe diameters and the geometry in the Venturi section of the MPFM. Available software is Star-CCM+, SpaceClaim and a Python interpreter. In addition, data from MPFM performance tests are also available.

1.5 Approach

The project is approached by first creating a CFD model that has an equivalent pipe geometry to an existing MPFM test-loop. The physical test-loop can be seen in Figure 3.1. From the test-loop empirical data is extracted for a few two-phase gas-liquid tests, and CFD simulations are then completed for the same test cases. The results from the experimental test and the CFD simulations are then compared, in order to a find suitable modeling method and validate it. Once a suitable modeling approach has been established in CFD, the geometry and flow regimes will be modified in order to evaluate the sensitivity of the MPFM to varying flow conditions. The results will then be be post-processed so that the results can be analyzed, and the sensitivity study can be concluded.

1.6 Previous studies

In this section previous studies that are relevant to this project are briefly presented. It is explained how results from previous sensitivity analyses and in-house experimental studies have inspired and aided the research completed in this study.

1.6.1 Findings from Company' in-house testing facility

At an in-house testing facility, a test-loop has been set up for studying MPFMs, see Figure 3.1. The test-loop consists of piping with bends and blind-Ts, with an MPFM and additional sensors installed. The measurements generated from the sensors provide valuable data and knowledge on how the system operates. This has been utilized in this thesis as a foundation and as comparison data in order to validate and verify simulation results. The in-house experiments performed at the test-site indicate that the design of the upstream geometry has a small or insignificant impact

on the MPFM accuracy, but it has been concluded that a CFD analysis of the flow in the MPFM is necessary to gain more knowledge. This is the basis for this project.

1.6.2 Influence of design parameters of upstream Venturi pipeline on multiphase flow measurements

A study conducted at the School of Mechanical & Aerospace Engineering, Nanyang Technological University, Singapore evaluated how the vertical entrance length and the blind-T depth affected multiphase flow measurements using a multiphase flowmeter (MPFM). The study showed that phase fraction measurements from the gamma detector indicated an increase in measured phase fractions with longer vertical entrance length, which corresponded better with the cross-sectional phase fractions in the pipe. This was explained by the flow becoming more axisymmetric. This increase was seen for flows with gas volume fractions between 26% to 83%. Additionally, the study assessed how the horizontal length of the blind-T depth affected the MPFM. Results indicated that changing this parameter was insignificant up to three diameters increase. Beyond this point, some additional local vortices and slightly lower liquid tangential velocity were observed. [3].

1.6.3 Characterization of multiphase flow blind-t mixing using high speed gamma-ray tomometry

In order to increase the accuracy of the measurements done by a MPFM it is crucial that the flow is mixed beforehand to make the multiphase more homogeneous. This is usually achieved with a blind-T upstream of the Venturi section in the MPFM. A study carried out to evaluate the effectiveness of a blind-T obstruction in mixing the flow showed that blind-T significantly influenced mixing by disrupting phase separation and improving the homogeneity of the flow. However, the results also showed that downstream of the blind-T the flow started to regain its intermittent nature, meaning phase separation was seen after a short distance after the blind-T. Therefore it was concluded that the blind-T is important for the flow mixing but the distance between the blind-T and the MPFM is as important parameter which needs to be accounted for. The distance was evaluated and the results from this investigation showed that there is not an optimal length between the blind-T and the MPFM due to it being directly influenced by what type of flow that is being measured. [5]

2
Theory

In this chapter, the necessary theoretical knowledge will be elaborated. Multiphase flows, the measuring techniques used in MPFMs as well as modeling approaches in CFD will be covered here.

2.1 Multiphase flow

Multiphase flow refers to fluid flow where multiple phases, such as gases, solids, and liquids, coexist. These flows are complex in nature due to the interactions between the different phases. The phases can exchange mass and momentum and the phasic interfaces are rarely rigid, making multiphase flows difficult to predict. In the offshore oil- and gas industry, the flow produced from a well is multiphase with a mixture of water, oil and gas. When discussing multiphase in an oil-and gas application common metrics are used which will be elaborated further here;

- Gas-volume fraction (GVF), the volume flow ratio of gas to total multiphase fluid.
- Liquid-volume fraction (LVF), the volume flow ratio of liquids to total multiphase fluid.
- Phase hold-up, the ratio of space occupied by the one phase, to the total fluid volume.
- Slip ratio, the ratio between 2 phasic velocities, for example the slip ratio between liquid and gas can be expressed as: $SR = \frac{V_{gas}}{V_{liquid}}$ [1].

In order to understand the flow characteristics they can be categorized in flow regimes. For example, in pipe flow the regime may be segregated, annular or plug. The active flow regime is dependent on the fluid properties, operating conditions and pipe geometry [1].

Working with MPFMs it is important to differentiate between phase hold-up and volume fraction. The phase hold-up relates to the amount of space occupied in the pipe by the phase in a given moment. The phase volume fraction is the fraction of the total volume flow rate accredited to one phase. In this regard, the volume fractions also accounts for the slip between the phases.

2.1.1 Flow Regimes

The flow regime for multiphase flows depends on various characteristics, such as operating conditions, fluid domain geometry, fluid properties, and the flow rates of the different phases. When studying multiphase flows, the flow regime is not necessarily constant but can change throughout the domain of interest, often through gradual transitions at different rates. Flow regimes are primarily studied for gas-liquid multiphase flows, as liquid-liquid effects are generally less pronounced in comparison.

One parameter contributing to the gradual change of regime is the geometry of the fluid domain. Features like convergent or divergent sections (e.g., Venturi sections), sharp bends, or blind-T's can significantly impact the flow regime. Furthermore, when studying the flow regime inside a domain the orientation of the piping will also have an effect. If the flow is traveling in a horizontal pipe, the transition of regimes are mainly a function of the pipe diameter, the difference in density between the phases and the surface tension at the interface between the gas and liquid. This results in horizontal flows to more commonly show stratified behavior. In contrast, in vertical multiphase flows the regime is more dependent on the superficial gas velocity which generally increases compared to horizontal flows, resulting in more plugging and bubbly flows [1].

A simple illustration on how the determination of the flow regime in vertical and horizontal pipes can be achieved is presented below in Figure 2.1, representing horizontal flows, and Figure 2.2, representing vertical flows. By using these graphs, an estimation on what the flow regime might be can be made and proper countermeasures for handling it can be established.

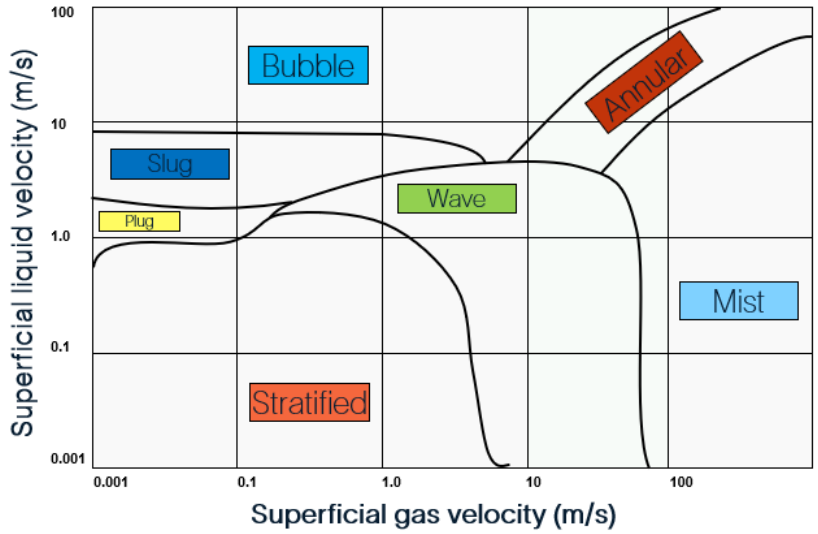

Figure 2.1: Horizontal Flow Regime Map

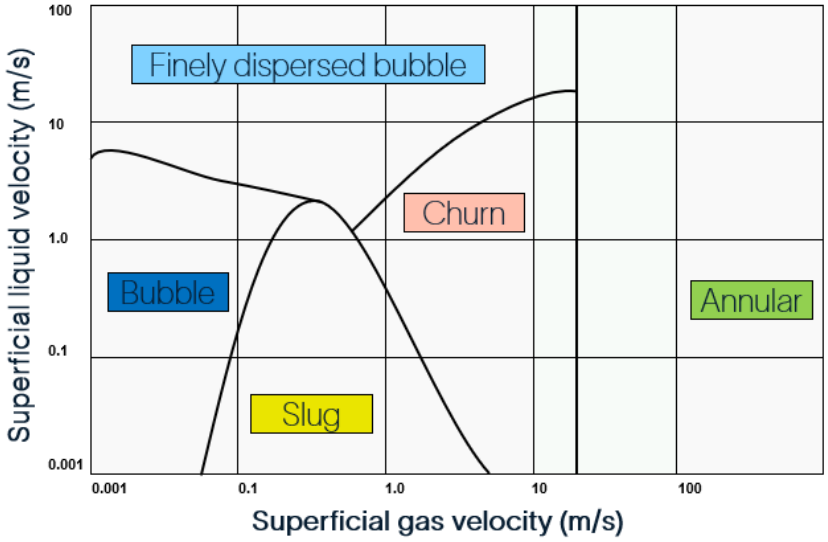

Figure 2.2: Vertical Flow Regime Map

The flow regimes encountered in this project are stratified, plug, and annular. Stratified flows are characterized by the separation between the gas and liquid phases due to gravity, resulting in a clearly defined interface. Plug flow is dominated by liquid or gas plugs, which are large bubbles or droplets with diameters smaller than the piping diameter. In this project, the plug definition is extended to include cases where gas is dispersed within a liquid plug. The annular flow regime features a liquid film traveling along the walls, with gas occupying the bulk at the center of the pipe. Some liquid droplets may be dispersed in the gas. The flow regimes described here are illustrated in Figure 2.3.

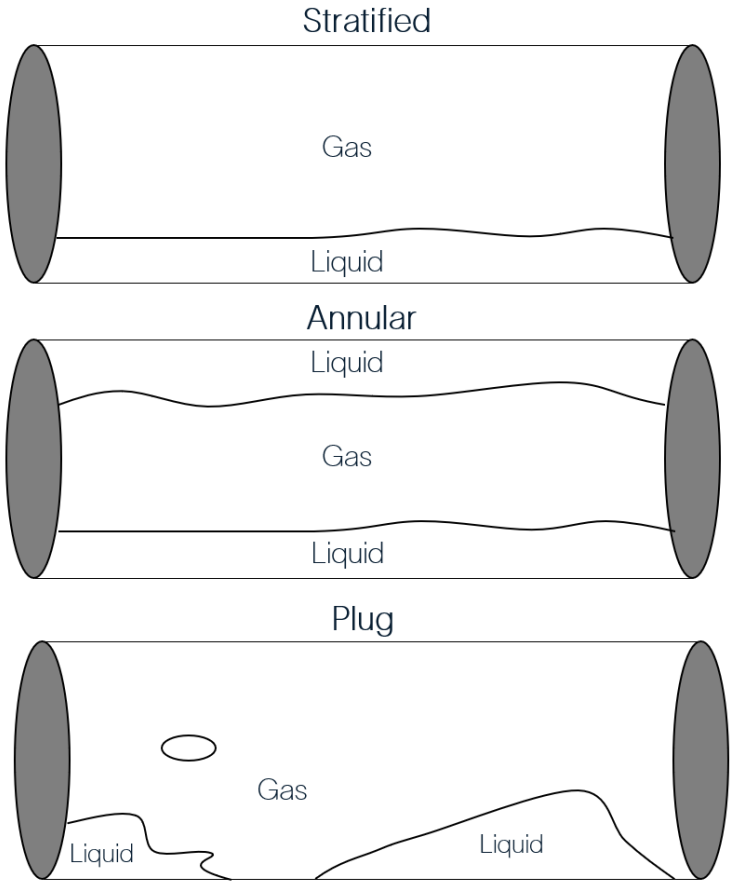

Figure 2.3: Flow regime illustration.

2.1.2 Surface tension

When handling multiphase flows, it is crucial to consider the forces affecting the interface between the immiscible phases. This contact force at the interface is described as surface tension. Surface tension is a scalar property that describes the amount of external force it can resist, effectively acting like an elastic sheet covering the liquid. This elastic sheet exists because molecules in the bulk are drawn in all directions by neighboring molecules with equal force, resulting in a net zero force. However, at the interface, molecules lack neighbors in all directions pulling with equal force, causing them to be pulled inward toward the bulk. This creates internal pressure that forces the interface to shrink, forming an elastic membrane facing the gas. Depending on the surface tension, the interactions between phases are thus significantly affected[6].

The value of surface tension can be a property that is not well tabulated and will instead need to be computed. There are several correlations based on experimental data, and for oils there is a commonly used correlation which follows:

$$\sigma = 0.00221\,(42.4 - 0.047(T - 460) - 0.267(^{\circ}\text{API}))\,e^{-0.0007p} \tag{2.1}$$

Where the surface tension is dependent on the operating pressure p and temperature T. In addition to this, it is dependent on the API gravity, which is a measurement from the American Petroleum Institute that relates how heavy or light the oil is in comparison to water [6].

2.1.3 Interphase Interactions

Interphase interactions describe ways in which individual phases interact with each other in multiphase flows. These phenomena are important to consider in order to understand why a multiphase flow behaves the way it does. The interphase interactions are very dependent on flow regime, operating conditions as well as the properties of the individual phases. In this project, interphase interactions that influence mixing and homogeneity are of interest and are developed further in this section.

Interphase Drag

Interphase drag refers to the force in a continuous fluid that opposes the relative motion of the dispersed phase. In high GVF gas-liquid flows, the interphase drag describes resistance exerted by the gas on the droplet's relative motion [7]. There are many factors that influence the drag that a droplet experiences, such as shape, gas- and liquid viscosity, density ratio etc.

Density

The ratio of densities in a mixture is an important factor when it comes to segregation and separation of the phases. The more difference in density in the phases, the more separation will be induced by gravitational effects and flow curvature. Conversely, the closer the densities are, the easier the flow is homogenized and mixed.

2.2 The Multiphase Flow Meter

Multiphase flow in oil and gas applications generally consists of three different phases: oil, gas, and water. To evaluate the individual phase volumetric flow rates, the phase fractions and pressure drop over the Venturi section need to be established. The meter is designed to measure the volume fractions of two of the three incoming phases, as their fractional sum should equal one. With the phase densities known from PVT data, and the phase fractions and pressure drop measured by the MPFM, the phasic volume flow rates can be determined. [1].

The key components of the MPFM are the Venturi throat, gamma-beam, and pressure sensors, as indicated in Figure 2.4. It is of great importance that the flow is homogeneous in the throat, so that the gamma-beam correctly captures the phases

that occupy the throat. In the MPFM studied in this project, the beam is oriented orthogonally to the pressure sensors.

2.2.1 Measurements

The quantities measured by the MPFM using sensors are the pressure drop over the Venturi section as well as the phase fractions, or hold-up in the venturi section. In this section the measurements made by the MPFM are explained in more detail.

Dynamic pressure drop

The pressure drop is measured using 2 manometers, one just before the converging section of the Venturi pipe section, and one in the throat, as shown in Figure 2.4. Knowing the height h of the Venturi section, the dynamic pressure drop in over the converging section can be deduced as shown in Equation2.2 below, assuming no losses:

$$\Delta p_{dyn} = \Delta p - \rho_{mixture} g h, \tag{2.2}$$

where p is the pressure and g is the gravitational acceleration. $\rho_{mixture}$ is the mixture density, and is determined once the composition of the fluids occupying the pipe is known. The process for the determining the fluid composition and $\rho_{mixture}$ in the pipe is described below.

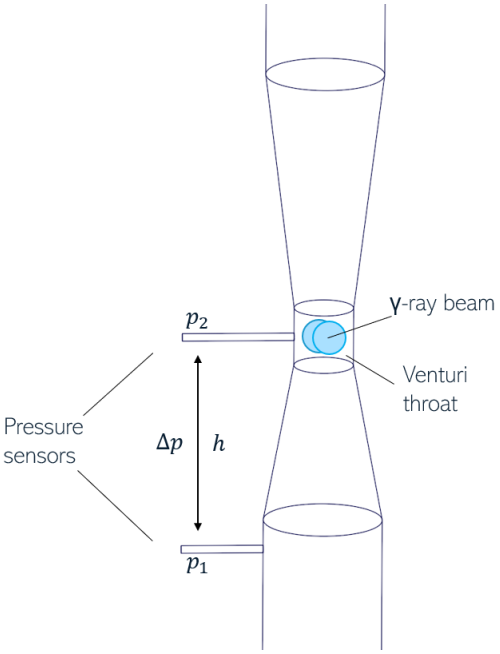

Figure 2.4: MPFM overview

Volume Fractions, Hold-up

There are several different technologies for determining the phase fraction in a multiphase flow. In this project, the MPFM studied utilizes gamma-ray absorption, and thus this section will only focus on this technique. In theory, the gamma-ray method

is applicable for all two or three-phase flows, independent of the combination, with a water cut of 0-100% and a gas volume fraction of 0-100%. From a nuclear source such as Barium-133, gamma-rays generated from the radioactive decay traverse the fluid of interest. The rays interact with the fluids occupying the pipe, causing a reduction in intensity or total absorption of intensity for an energy level. These two different phenomena are called the photoelectric effect, for total absorption of photon and the Compton effect, scattering of a photon by an electron. For Barium-133, the gamma-ray energy levels of interest are 32 keV and 81 keV [8]. An illustration of this process is shown in Figure 2.5.

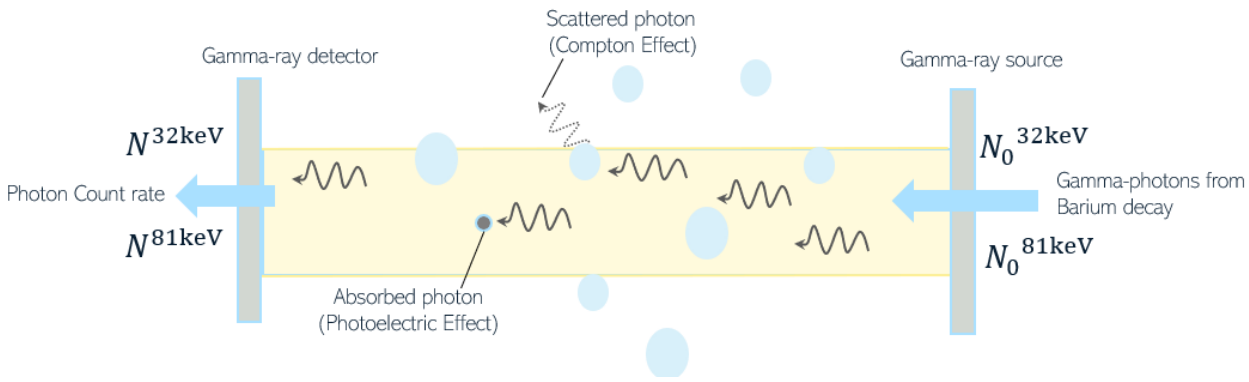

Figure 2.5: Illustration of γ beam

In order to find the fluid interaction with the gamma-rays, it is also necessary to know the empty pipe absorption rate N_0. Water, oil and gas all interact differently with these gamma-ray energy levels, and based on the count rates N^{32keV} and N^{81keV} returned on each energy level, the hold up of each phase can be deduced using triangulation. On the opposite side of the Barium-133 source a gamma-ray source a detector is placed, which measures the intensity reduction of the gamma-rays by evaluating the incoming photon count rate N for each energy level. This phenomena can easily be described with the energy spectrum for Barium-133 shown in Figure 2.6.

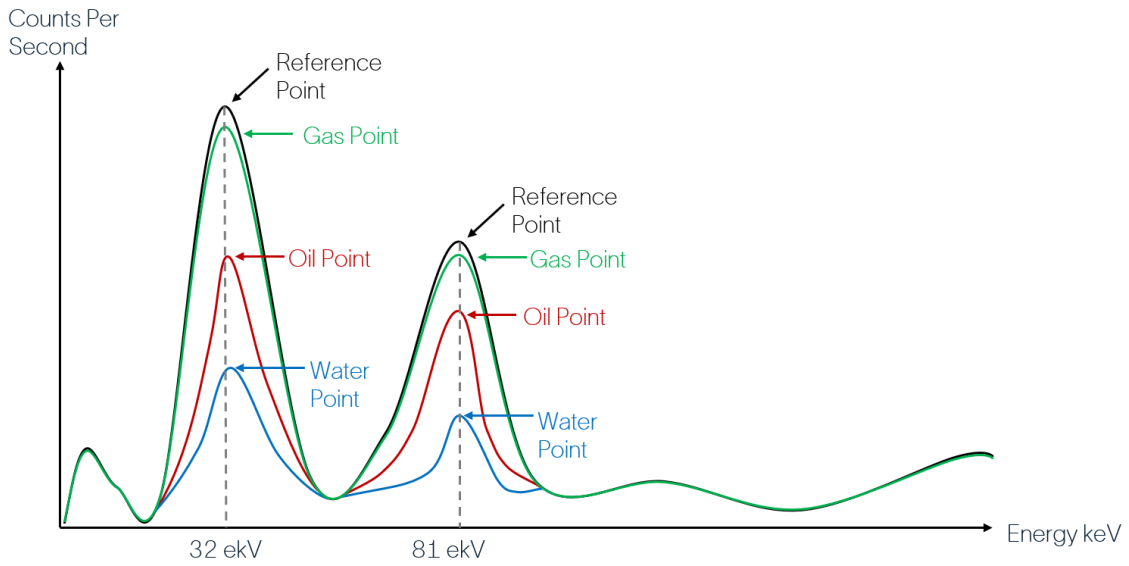

Figure 2.6: Energy spectrum for Barium-133.

The spectrum shows at what energy levels Barium-133 emits gamma rays. The x-axis represents the energy each photon carries, while the y-axis represents the intensity in counts per second. The reference point is the expected intensity of photons if the pipe were to be evacuated, and thus the rays do not traverse through any material. The green, red, and blue graphs represent how much lower the detected intensity changes when they interact with a multiphase flow. From the graph, it is possible to see that gas has a lower reduction on the count rate compared to water, and thus the different materials can be recognized. The detector is able to characterize the fluid by utilizing the mass attenuation coefficient μ, which is a quantity expressed in terms of unit area per mass (cm^2/g). The mass attenuation coefficient relates to how well electromagnetic radiation is able to travel through a material. This quantity is intrinsic to each material and gamma photon energy level and is directly proportional to the atomic number [1][9]. With the known mass attenuation coefficient and registered decrease in radiation from the detector, it is possible to evaluate the phase fractions and composition of the multiphase fluid.

2.2.2 Processing

In this section it is described how the sampled quantities from the MPFM are processed into phase volumetric flow rates.

Prerequisites

In order to obtain the volumetric flow rates, phasic velocities and other flow quantities, some processing is required of the measurements. First of all, the densities ρ of the fluids in the MPFM must be known in advance, as these are used as input information for processing. Additionally, the mass attenuation coefficients μ of the phases must be known, as well as the empty pipe count rate N_0. Since the pressure drop over the Venturi section can be significant, compressibility effects should not

be neglected. Specifically, the gas density needs to be corrected for the pressure [1].

Processing

When handling 3-phase flows in the Venturi pipe, the following system of equations is used to find the hold-up of each phase from the measured count rate N of each gamma ray energy level monitored:

$$N^{32keV} = N_0^{32keV} e^{-D[(\mu_{oil}^{32keV}\rho_{oil}\alpha_{oil})+(\mu_{water}^{32keV}\rho_{water}\alpha_{water})+(\mu_{gas}^{32keV}\rho_{gas}\alpha_{gas})]} \tag{2.3}$$

$$N^{81keV} = N_0^{81keV} e^{-D[(\mu_{oil}^{81keV}\rho_{oil}\alpha_{oil})+(\mu_{water}^{81keV}\rho_{water}\alpha_{water})+(\mu_{gas}^{32keV}\rho_{gas}\alpha_{gas})]} \tag{2.4}$$

$$\alpha_{oil} + \alpha_{water} + \alpha_{gas} = 1 \tag{2.5}$$

where D is the inner diameter of the pipe, and α is the phasic hold-up, which is the quantity solved for in this equation. The hold-up is a measure of how much space of the pipe is occupied by each phase in one instant [8].

For a 2-phase flow, which is what is analyzed in this project, the following simplified equation can be used. In this case, only the attenuation on the 81keV energy level is used to compute the gas hold-up.

$$\alpha_{gas} = \frac{\rho_{liquid}\mu_{liquid} - \frac{ln(\frac{N_0^{81}}{N^{81}})}{D}}{\rho_{liquid}\mu_{liquid} - \rho_{gas}\mu_{gas}} \tag{2.6}$$

The Equation 2.5 can be used to find the liquid hold-up. With the known phase hold-ups occupying the pipe, the mixture density can be found using Equation 2.7.

$$\rho_{mixture} = \alpha_{gas}\rho_{gas} + \alpha_{liquid}\rho_{liquid} \tag{2.7}$$

The mixture volume flow rate can be found using Equation 2.8:

$$Q_{mixture} = C_d C_f \frac{A_1}{\sqrt{(\frac{A_1}{A_2})^2 - 1}} \sqrt{\frac{2\Delta p_{dyn}}{\rho_{mixture}}}, \tag{2.8}$$

where C_d is the discharge coefficient, and C_f is a form factor. In this project $C_d = 0.98$ and $C_f = 1$. $A_1$and A_2 are the pipe cross-sectional areas just before the Venturi section and in the Venturi throat respectively [8]. The dynamic pressure drop is found using Equation 2.2. The volume fractions of each phase is found using Equation 2.9 and 2.10

$$GVF = \frac{SR \cdot \alpha_{gas}}{(1 - \alpha_{gas} + SR \cdot \alpha_{gas})} \tag{2.9}$$

$$LVF = 1 - GVF \tag{2.10}$$

where GVF is the gas volume fraction, LVF is the liquid volume fraction and SR is the gas-liquid slip ratio defined as $SR = \frac{V_{gas}}{V_{liquid}}$. The slip-ratio between the phases

is typically extracted from a model. Now finally, the phasic volume flow ratios can be found as shown in Equation 2.11 and 2.12

$$Q_{gas} = GVF \cdot Q_{mixture} \tag{2.11}$$

$$Q_{liquid} = LVF \cdot Q_{mixture} \tag{2.12}$$

The superficial velocity is the velocity any phase would have if the pipe flow were single phase [8]. The superficial velocity can be found using 2.13:

$$V_{s,phase} = \frac{Q_{phase}}{A_{venturi}} \tag{2.13}$$

The phasic velocity is calculated using Equation 2.14:

$$V_{phase} = \frac{V_{s,phase}}{\alpha_{phase}} \tag{2.14}$$

2.2.3 Error contributors

When measuring multiphase flows using gamma-ray systems, there are multiple sources of error that should be considered. Of course, some accuracy and precision error should be expected from all instruments, but this will not be covered in depth here. The main sources of error in multiphase flow metering are due to the natural decay of the Barium, the homogeneity of the flow and slip-modeling. These error sources will typically manifest as noise in the measurements, and averaging is required to obtain meaningful results.

Natural Decay

Since the natural decay of the Barium is a random process, the count rate of gamma-rays traversing the pipe is never fully known for short time periods. Since the gamma-ray detector only measures the incoming photons, the count rate of absorbed photons also cannot be known. But in order to compute the phase fractions it is the absorbed photons that are of interest. Therefore, the natural decay becomes a source of error for the phase fraction measurements. When averaging the measurements over a period of time, the influence of this error source is reduced.

Homogeneity

In order for the gamma-ray beam to measure correctly, it is required that the phases are well mixed in the throat, and that they are homogeneously distributed over the pipe cross-section. In reality this is rarely the case, and depending on the flow-regime the liquid phases can stick to the walls in a non symmetric way. This might influence the measurement accuracy of the phase volume fractions. In this project, this source of error will be investigated further.

Slip-modeling

In order to determine the phase volume fractions from the phase hold-up a slip-model is used. These models are difficult to formulate, since they require detailed

and extensive knowledge about the flow regimes, which may also vary with time. Another difficulty when formulating the slip-model is the topology of the liquid phase. In high GVF applications, the flow is typically annular dispersed. The liquid phase may appear as a continuous phase sticking to the wall, or as droplets dispersed in the gas. The velocity of the dispersed and continuous liquid phase greatly differs, making it difficult to formulate a slip-model, since that would additionally require knowledge on how much of the liquid phase is continuous or dispersed.

2.3 CFD

In this chapter, theory related to CFD modeling of the flows in the MPFM will be developed. Here topics such as multiphase modeling, boundary conditions and meshing will be covered.

2.3.1 Meshing

The mesh is one of the most crucial parts of simulating fluid flows with CFD. Generally when faced with issues such as failing simulations, the mesh is at fault. This is due to convergence and quality of the simulation being directly dependent on the quality of the mesh through the spatial discretizations [10]. Creating a mesh for CFD is generally a complicated procedure that involves a commercial software package for mesh generation. For unstructured 3D meshing the grid is built from tetrahedral, hexahedral, pyramids, prisms and dodecahedra elements which all serve a different purpose for the discretizations. Close to the walls the importance of element choice is significant for numerical reasons. Thus, the mesh is generally built from the domain boundary surfaces and into the freestream volume. Depending on the size of the mesh, the CFD solver is able to resolve the flow structures correctly only if the cells are sufficiently small enough. However, when simulating Eulerian multiphase flow, the mesh must also be coarse enough to conform to the continuum assumption. In other words, there must be sufficient particles of the dispersed phase so that averaging within the control volume provides a good approximation of the dispersed phase as continuous. Additionally, a too refined mesh becomes very costly, thus a trade-off between accuracy and simulation time is necessary.

To ensure that the mesh captures the relevant physics in the domain, a mesh convergence study should be performed. This avoids simulation divergence and ensures that the physics is sufficiently resolved while maintaining good simulation economy. Regions with boundary layer flow, near a wall require a fine mesh. This is due to the substantial gradients near the wall, while the freestream flow away from the wall doesn't require to be resolved in such detail. However, the quality of the mesh and how it is built up is determined by the level of accuracy, the computational models utilized and previous knowledge and is therefore something that changes over time within a project. Therefore, it is important to continuously evaluate the mesh quality [11]. It is possible to check the mesh quality by evaluating several different parameters. In this project mainly 4 different quantities are used: The skewness angle, face validity, cell aspect ratio and volume change. These quantities

are described briefly below.

Skewness angle

The skewness angle is a measurement which tells us how much a computational cell deviates from an ideal shape. It's the angle between the face normal vector and the vector which is connecting the two cells centroids. The angle between the face of two cells affect wether diffusion of quantities will be bounded or not, and is thus a very important parameter to consider. The value of the skewness should never be above 85° since angles greater then this will have an impact on the robustness and cause numerical and convergency issues. If the value of the skewness is zero it means that the mesh is perfectly orthogonal [12].

Face Validity

Another key parameter which determines the mesh quality is the face validity. The face validity describes the correctness of a cell by evaluating the face normal relative the centroid they are attached to in the cell and is an area-weighted parameter. A cell is considered good if the value of the face validity is equal to 1 which occurs when all face normals point outwards of the cell from the centroid point. If the cell shows some kind of concavity this will result in face normals pointing inwards and the value of the face validity be computed to be below 1 [13].

Cell aspect ratio

The aspect ratio is the ratio between the longest length of the cell compared to its shortest. It is desired to have a value as close to 1 as possible but there are cases where a higher value can be favorable. When wanting to save computational time one can stretch the cells such that they align with the flow, but the value should not exceed 5. Bad aspect ratios might cause gradients to not be accurately captured in the cell as well as convergence issues [11].

Volume change

Lastly, volume change describes the relation between a cells volume compared to its biggest neighbors cell. One strives to have a conformal mesh where the cell volume does not expand or contract rapidly, i.e having a smooth transition between coarse and refined mesh regions. This helps maintaining the accuracy and stability of the simulation. If the cells volume compared to its biggest neighboring cell is equal, the ratio will be 1. However, if the surrounding cells are significantly lower, the ratio will be much smaller than 1 causing instability and solver issues [13].

2.3.2 Upwind differencing schemes

In order to solve the governing equations using CFD, they must be discretized by meshing the domain and using finite differencing [11]. This is so that the temporal and spatial derivatives of the governing equations can be approximated using

Taylor series. There are many ways to do so, such as central differencing schemes and upwind schemes. When selecting a discretization scheme, desired attributes are conservativeness, boundedness and transportiveness [14].
Boundedness means that the calculated cell face values are neither larger or smaller than its neighbouring node values used to calculate it. Transportiveness means that the discretization scheme accounts for the direction in which information travels in the domain.

The selection of discretization scheme depends on the flow characteristics. A suitable discretization scheme for flow characterized by strong convection are upwind schemes [11], which are widely used in engineering applications due to their simplicity. These differencing schemes complete the discretization using upstream conditions, which make these schemes transportative. It can also be shown that these schemes are conservative and bounded [14] which are positive attributes, however the upwind schemes are sensitive to nummerical diffusion.

2.3.3 Boundary conditions

In order to fully define and solve a CFD problem, boundary conditions must be applied. They prescribe fluid characteristics at the boundary of the domain, and their nature depends on the type of boundary. The boundary conditions relevant to this project are elaborated below.

Wall Boundary condition

When a fluid encounters a wall, typically the no-slip condition applies. This means that the fluid at the boundary is assigned the same velocity as the wall (usually 0). Moving away from the wall, the fluid velocity approaches the free-stream velocity. Additionally at the walls, heat transfer should also be defined. If wall heat transfer is neglected the wall is assumed to be adiabatic, meaning that there is no heat transfer between fluid and wall.

Inlet boundary conditions

Velocity inlet is a commonly used boundary condition for inlets, applied to simulations where the velocity profile at the inlet is known. As a default the velocity profile is assumed uniform but other profiles are possible to implement as well. The velocity inlet is defined by the velocity vector and scalar properties for the fluid at the boundary. The boundary is intended to use for incompressible flow and the stagnation properties vary to satisfy the velocity profile distribution [15].

Outlet boundary conditions

A pressure outlet is a boundary condition in which the static pressure for the outflow is defined. A common assumption associated with this boundary condition is that the static pressure is constant at the outlet [15].

2.3.4 Turbulence modeling

In many fluid flows, turbulence has a great influence on flow characteristics. In multiphase applications, the turbulence will influence the mixing and dispersion of the fluid phases. Turbulence adds a great deal of complexity to a fluids problem, and although turbulent eddies can be resolved, it is usually preferred to model the effects of turbulence. There are many ways to model turbulence, and also sub-adaptations of those models. When modeling turbulence, 3 main parameters are used;

- k - the turbulent kinetic energy
- ω - the turbulent specific dissipation rate
- ϵ - the turbulent dissipation rate

All of these models assume isotropic turbulence. In this chapter, models relevant to this study are elaborated.

$k - \epsilon$ model

The 2 - equation $k - \epsilon$ model models the transport equations of turbulent kinetic energy and dissipation [16]. This model is popularly used, and is a good compromise in terms of computational cost and generality [11]. However, this model typically over-predicts the shear stress in adverse pressure gradients. Therefore, this model is best used in free-stream regions with smaller pressure gradients.

$k - \omega$ model

The $k - \omega$ model is a 2 - equation transport model of kinetic energy and specific dissipation for turbulence [16]. It performs well in regions with lower Reynolds number and turbulence. As a result, it is useful in close proximity to walls in the viscous sub-layer [11], in contrast to the $k - \epsilon$ model.

Shear Stress Transport (SST) model

The SST model is a combination of the $k - \omega$ and $k - \epsilon$ models, in order to capture their strengths in different regions of the flow [17]. The $k - \omega$ model is used in the boundary layer, while the $k - \epsilon$ model is used in the free stream region of the flow. In order to achieve a smooth transition between the $k - \epsilon$ and $k - \omega$, a blending function is applied. This turbulence model is especially useful in areas with adverse pressure gradients and separating flow. In order to accurately apply SST model, a fine mesh near the wall is required [11].

2.3.5 Wall treatment and y+ approach

For geometries containing solid walls in the modeling domain, there are significant flow gradients in the boundary layers close to the walls. The boundary layer requires special attention when modeled and simulated. A common way to tackle this is to utilize the dimensionless distance called y^+ in order to express the sub-layers physical length. y^+ is defined in Equation 2.15 below

$$y^+ = \frac{yu_\tau}{\nu} \tag{2.15}$$

where y is the absolute distance to the wall, u_τ the wall friction velocity and ν the kinematic viscosity. Using the value of y^+, it is possible to categorize the fluid regions near a wall accordingly. The classification is divided into three categories, a viscous sub-layer with $0<y^+<5$, buffer sub-layer with $5<y^+<30$ and fully turbulent sub-layer with $30<y^+<400$ [11]. Using these layers it's possible to describe the dissipation and production of turbulent kinetic energy. Close to the wall, the dissipation reaches its peak value due to the absence of turbulent kinetic energy while the production reaches its peak within the buffer layer where Reynolds stress and viscous stress are equal. A consequence of these large gradients formed close to the wall is that the mesh will have to be dense in order to resolve the flow. Otherwise, wall functions can be used instead to solve these areas.

Wall functions can be utilized to avoid having a very fine mesh. Additionally, these functions are sometimes required if the turbulence models used are not valid in the near-wall region. These functions are semi-empirical rules which are constructed from the logarithmic law of the wall [11].

2.3.6 Multiphase modeling

The main challenge with multiphase simulations is the numerous degrees of freedom that must be defined, requiring extensive knowledge of the individual phases and their interactions. In order to simplify this, many simulation methods make major assumptions that in some cases are not representative of the actual flow. Therefore great care must be applied when selecting a multiphase model, so that the flow is correctly represented in the model and accurate results can be extracted.

When simulating multiphase flows there are many modeling options. The popular models for engineering applications can be divided into 2 main subgroups, Eulerian- and Lagrangian type frameworks. The Eulerian strategy is to model all phases as continua, while the Lagrangian method tracks the motion of the dispersed phase as individual particles, droplets or bubbles in a continuous (Eulerian) carrier phase. For this project models of the Eulerian type framework will be used, as they provide a macroscopic, system level view of the problem. In this case, the motion and forces acting on individual particles are not of interest, making Lagrangian frameworks unsuitable for this project [7].

Eulerian Multiphase model

The Eulerian multiphase model treats both phases as continua, and this model is derive by applying volume- or ensemble averaging [11]. In single-phase fluid mechanics, the random motion of molecules is averaged over a control volume in order to describe the fluid as a continuum. In a similar way, the Eulerian multiphase framework averages both phases over a control volume. This means that in the Eulerian approach, both carrier- and dispersed phases are treated as continua. In this model, one set of transport and continuity equations are solved for each phase. As consequence of the averaging, some additional unclosed terms are introduced.

These terms can be summarized to describe the phase interactions which require modeling [18].

Phase Interaction Topology

For two-fluid models such as the Eulerian Multiphase model, STAR-CCM+ has a range of closure relations for the modeling of dispersed, mixed and stratified flows. For a known pair of phases STAR-CCM+ is able to model mainly two types of topology, continuous-dispersed topology and multiple topology.

Continuous-dispersed topology is based on the assumption that one of the phases always is considered as the dispersed phase and the other phase as constant continuous. By utilizing this it enables to model the interaction between the phases. This choice of topology is especially good for flows which have either high GVF or high LVF since it is a time saving topology approximation. However, for more complex flows an extension of the continuous-dispersed topology can be implemented, the multiple topology. This model better predicts and evaluates the interaction for varying phase compositions, flows containing large amount of bubbles, droplet or particulates. In short, this model utilizes a volume-fraction based approach in order to evaluate if the phase should be treated as a continuous phase or dispersed phase. In order to use this model, the phases must instead be defined as primary and secondary phase. The flow regimes can thus be defined as first disperse regime, intermediate regime and second dispersed regime. This entails that for the first dispersed regime, the secondary phase is dispersed in the primary phase and the opposite for the second dispersed regime. In the intermediate regime, neither phases is considered to be dispersed in the other phase and thus models the mixed flow instead [19].

2.4 Signal Processing and Spectral Analysis

When analyzing data, it is important to consider not only mean values but also fluctuations and oscillations. Spectral analysis is a valuable tool for signal processing and analyzing data in the frequency domain. In multiphase flow applications, it is useful in order to characterize the flow dynamics in terms of flow regime, turbulence, plugging etc. Spectral analysis together with CFD can give good insight into flow instabilities and their underlying causes. In addition, to evaluate the performance and accuracy of the CFD model, spectral analysis can be used to compare it to the experimental measurements from the test loop.

The Fourier transform, where a signal in time is transformed to the frequency domain, is the basis of spectral analysis and will be developed further in this chapter. Furthermore, applications and other signal processing techniques will also be elaborated in this chapter.

2.4.1 Fourier transform

The Fourier transform is a coordinate transformation, which is useful for representing oscillating signals. It is a mathematical tool which transforms a signal from time to a frequency domain representation [20]. An arbitrary periodic signal can be approximated as a sum of sines and cosines of increasingly high frequency, the concept is visualized in Figure 2.7. In other words, the arbitrary signal f can be decomposed to a sum of sines and cosines of varying frequency and phase angle by projecting f on orthogonal complex functions on the format $e^{i\omega t}$, where ω is a frequency, and t is time.

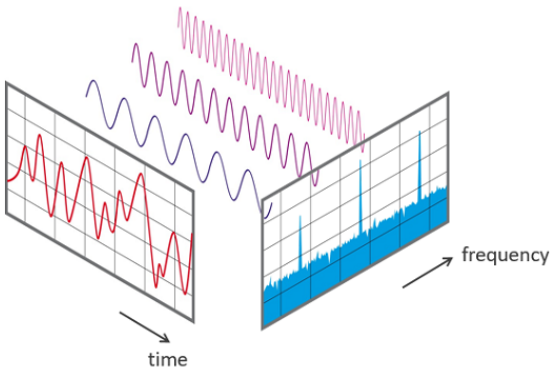

Figure 2.7: Visualization of a signal in the time- and frequency domain, used with permission from [21]

The arbitrary function $f(t)$ in time, can be represented in the frequency domain as $\hat{f}(\omega)$ using the Fourier transform operator F as shown in Equation 2.16

$$\hat{f}(\omega) = F(f(t)) = \int_{-\infty}^{\infty} f(t) \cdot e^{-i\omega t}\, dt \tag{2.16}$$

Typically, measurement data is not represented as analytic functions, but as measurements at discrete locations in time [20]. In order to adapt the Fourier transform to discrete data points, the Discrete Fourier transform (DFT) is used. Let f be a vector containing discrete data points, then $\hat{f}$ is represented as a vector of complex coefficients that indicate the amplitude of the corresponding frequency component in the signal. Let N be the number of samples and n a sample index, then the k:th Fourier coefficient $\hat{f}_k$ is computed as shown in Equation 2.17.

$$\hat{f}_k = \sum_{n=0}^{N-1} f_n \cdot e^{-i\frac{2\pi nk}{N}}, \tag{2.17}$$

The Fast Fourier Transform (FFT) is an algorithm used to compute the DFT that is particularly efficient to calculate in a computer [20]. FFT is the algorithm that is typically used in engineering applications and built in most programming languages, and is therefore synonymous to the DFT. Depending on the specific implementation and scaling of the FFT algorithm, the method for extracting the amplitude from the resulting vector of complex numbers $\hat{f}$ may differ. Typically it involves taking

the absolute of $\hat{f}$ and normalizing the result with the number of samples [22].

It is common to visualize the results from the FFT in a spectrum, and there are many ways to select the y-scale when it comes to signal power or magnitude. In this project, the selected y-scale is in root mean square (RMS) which is defined as follows [23]:

$$RMS = \sqrt{\frac{1}{N}\sum_{n=0}^{N} g_n^2}, \tag{2.18}$$

where g is an arbitrary sinusoidal signal. It is an intuitive measure of the mean power or amplitude of a signal and can be selected as an output format in the built-in FFT algorithms available in most programming languages.

2.4.2 Windowing

The FFT algorithm assumes that the signal processed is one period of a periodic signal. In other words, it is assumed that the ending data point smoothly and continuously transitions to the first data point, interpreted as if these data points are connected together circularly. In practice, the start and ending points of the data set are likely discontinuous, and it is very rare for the data set to conform to this assumption. This discontinuity acts similarly to a square wave, and causes the presence of artificial high frequencies in the FFT that also alias in the lower frequencies, so called spectral leakage. The resulting spectrum becomes noisy and difficult to work with [24].

In order to de-noise the FFT and improve clarity, window methods can be used. Windowing reduces the amplitude in the beginning and end of the signal, as shown in Figure 2.8. This reduces the noise caused by the discontinuity, and clarifies the resulting FFT spectrum. There are many different types of windows that can be used, with different advantages and disadvantages. One commonly used window is flat top window, which is more accurate at approximating the signal amplitudes in the spectrum compared to other window types. The penalty for using this type of window is reduced frequency resolution, but if the sample frequency is high the spectrum frequency resolution may still be sufficient [25].

2.4.3 Welch's method

In order to further reduce the noise and smooth the frequency spectrum, Welch's method can be used. It divides the signal into overlapping segments, applies windows and then computes a modified periodogram for each segment. Then the periodograms are averaged [26] to get the final smoothed spectrum. The penalty for the smoothing is reduced frequency resolution and precision, but with a high sampling frequency the resolution may still be satisfactory. Welch's method is a built- in function in most programming languages, and the generalized method is summarized below [27]:

1. In the time domain, the signal is divided into overlapping segments. The amount of overlap may vary, but typically 50%.

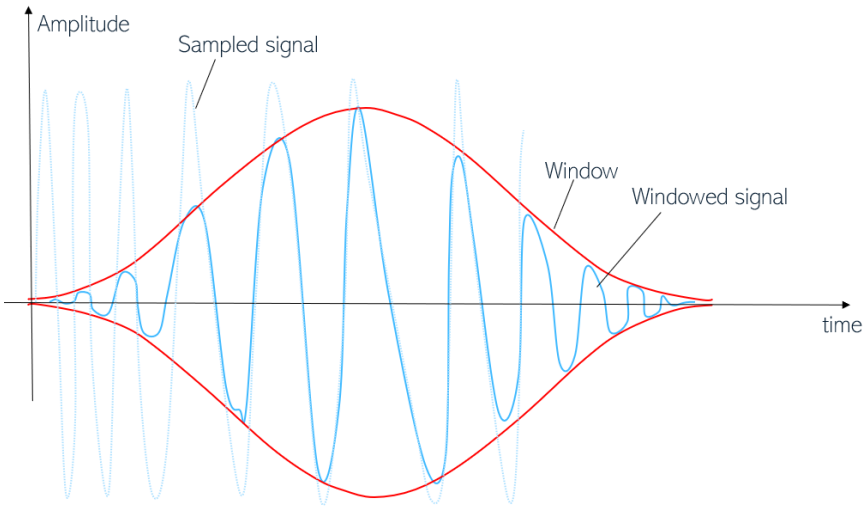

Figure 2.8: Visualization of windowing a signal

2. On each sample segment, the selected window is applied.
3. Each segment is transformed using FFT to get a signal segment spectrum in the frequency domain
4. All segment spectrums are averaged together to yield the final spectrum for the entire signal sample.

3
Methods

In this chapter, the methodology of the thesis will be explained and elaborated. The general approach was to first model the pipe-geometry such that it resembles the physical test-loop. Flow in this test loop was simulated in CFD, and then compared to empirical data for the same test cases. The comparison was used to evaluate, validate and subsequently find the most suitable modeling approach. Once this was completed, the MPFM sensitivity to design parameters and flow regimes could be investigated, by completing simulations for varying geometries and boundary conditions. The post processing and analysis of the results then complete this study.

The methodology used for this project can be summarized in the following steps. These will be elaborated further in this chapter

1. Literature survey
2. Review of experimental data
3. Model set-up
4. Simulation Validation
5. Design Simulations
6. Post processing

3.1 Literature survey

To establish a foundation for this thesis a literature survey was completed. Since this study focuses on evaluating sensitivities of the MPFM, the main purpose of the literature survey was to review previous studies, methodologies, results on the topic. The relevant information gained from this research was summarized in section 1.6.

3.2 Review of experimental data

In this section, the method for post processing raw MPFM-data to test-loop flow quantities is explained. This information will later be used to validate the CFD simulations. In addition, a spectral analysis of the experimental data was completed to gain insight into the expected flow regime in the test cases. This analysis will clarify the type of flow behavior anticipated for the selected cases in the CFD simulations. Furthermore, this information was used to compare the flow behavior in the CFD model with the experimental case and evaluate how well the CFD model captures the flow regime.

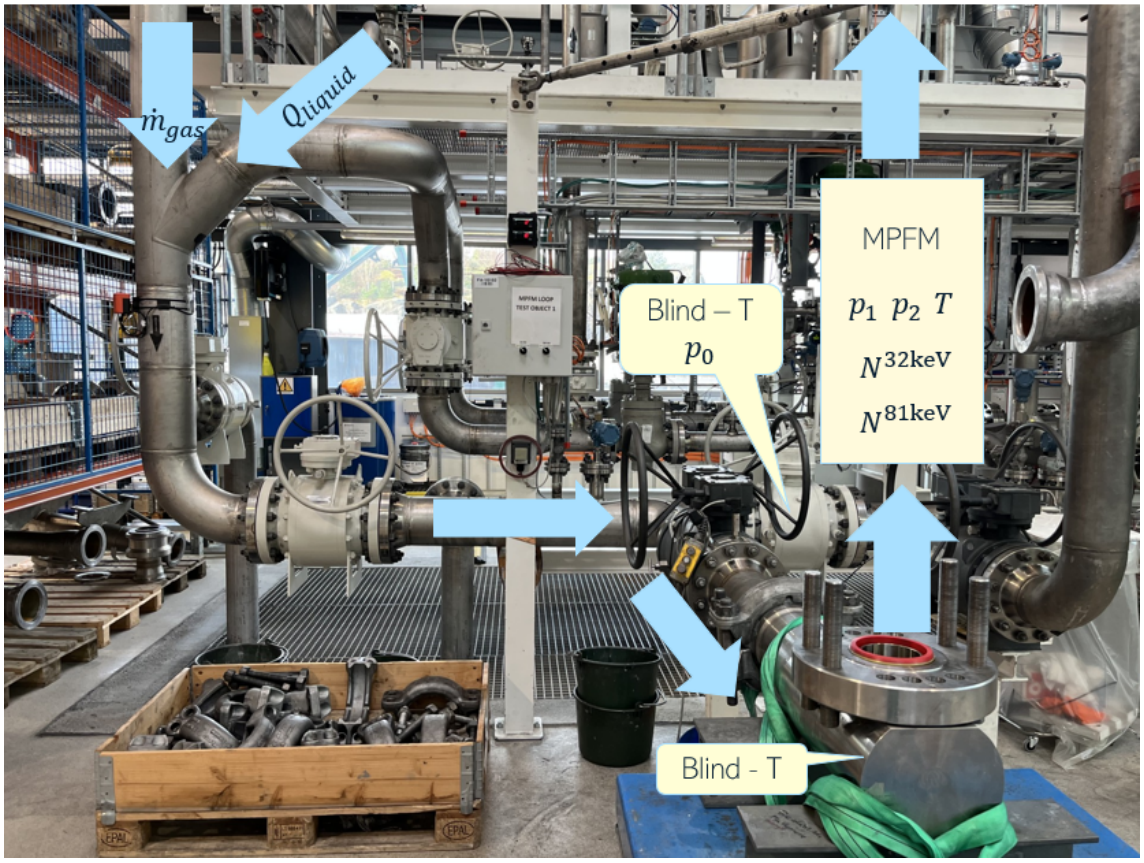

Figure 3.1: MPFM test loop at Company's testing facilities

3.2.1 Selection of Experimental Data

Before completing the simulations with varying flow- and design parameters, the CFD model had to be validated. In order to validate the CFD model, its results were compared to measurements from the physical test loop. 3 experimental test-cases were selected with 2-phase flow and GVF in the interval 90-98%, since wet-gas flow regimes was of interest in this project.

3.2.2 Extracting flow data

At Company's testing facilities, the MPFM studied in this project was experimentally evaluated in a test-loop. In this test-loop, pressure was measured at one additional location beyond the MPFM, in the most upstream blind-T. The test-loop is shown in Figure 3.1. Downstream of the MPFM, the mixture flows down a long outlet pipe straight, into a separator unit. The sensor locations, and by extension the available empirical data from the test-loop, are summarized in the list below, and they are also illustrated in the physical- and simulated domain in Figures 3.1 and 3.2 respectively.

- Gas mass flow rate at inlet $\dot{m}_{gas}$, 0.2 Hz sampling frequency
- Liquid volume flow rate at inlet $\dot{Q}_{liquid}$, 0.2 Hz sampling frequency
- Pressure gauge 0 p_0, upstream blind-T, 0.2,Hz sampling frequency
- Pressure gauge 1 p_1, just before convergent piping section, 1 Hz sampling rate

- Gamma-ray detector measuring photon count rates N^{32keV} and N^{81keV}, Venturi section, 45 Hz sampling frequency
- Pressure gauge 2 p_2, Venturi throat, 1 Hz sampling rate
- Temperature gauge T, upstream blind-T, 1 Hz sampling frequency

During a test, the data from these sensors was recorded once the test fluid has reached steady conditions. The empirical data was then post-processed as described in section 2.2.2 in order to extract information that can be used to validate the results and review the simulation set up of the test loop. Note that since only 2-phase gas-liquid flow is simulated in this project the selected test scenarios for the validations are also limited to 2 phases. Therefore Equation 2.6 is used to compute the gas hold-up. The data that could be extracted from the test-loop and used to validate the CFD model is summarized below:

- Gas- and liquid volume fractions, GVF and LVF
- Gas- and liquid volume flow rates, $\dot{Q}_{gas}$ and $\dot{Q}_{liquid}$
- Mixture density, ρ_{gas}
- Pressures from pressure gauges, p_0, p_1 and p_2

Note that volume fraction and volume flow rate at the Venturi throat are as measured by the MPFM. They do not necessarily indicate the true quantities, for reasons discussed in section 2.2.3. For indications of true volume flow rates at the Venturi throat, the inlet volume- and mass flow rates of liquid and gas were corrected for the Venturi throat pressure. However, these quantities were not corrected for the delay in time, i.e the time it takes for the fluids to travel from inlet to the Venturi throat. From the current test-loop it can therefore never be fully known the true hold-up or volume fractions in the Venturi throat at an instant, only estimations can be made.

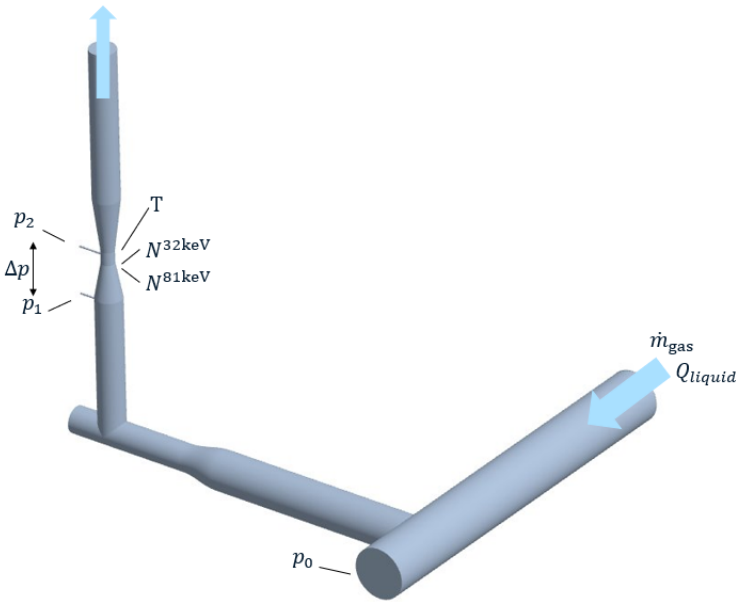

Figure 3.2: Sensor locations in test loop, represented in CFD domain

3.2.3 Spectral Analysis

Spectral analysis was completed for the GVF measured in the test-loop, sampled at 45Hz and measured for 30 minutes once the test loop flow has stabilized. Welch's method with flat top windows was applied to the 45 Hz data, producing RMS outputs. The number of segments was chosen to ensure a smooth spectrum without excessive smearing.

The resulting spectrums could now be evaluated in order to determine the behavior of the flow in the experimental cases. This gave an indication of what type of behavior that was interesting to investigate further in the CFD simulations.

3.3 Model set up

In order to simulate the flow in the MPFM, a model in commercial the CFD code STAR-CCM+ was prepared. In this program the geometry is parametrized, meshed and then modeling techniques and boundary conditions are applied. These steps are described in more detail below.

3.3.1 Geometry, surface preparation and parametrization

Since this study neglected any heat transfer between the multiphase fluid and the piping, all external geometry of the test-loop which would not affect the internal flow conditions could be removed from the simulation domain. The clean-up process consisted of removing small faces and simplifying some structures which have negligible impact on the simulation results. It is always a trade-off between to what extent small details can be kept at the expense of the simulation time.

Before the meshing process could begin, further simplifications were necessary beyond cleaning the external geometry. This was due to extremely small surfaces and complex geometry present at the sensors and detectors in the Venturi section. These features were therefore removed. This was deemed a valid simplification since the very small surfaces would not cause a significant flow disturbance and thus not affect the computation.

One of the main sensitivities for this project was to evaluate the impact of the upstream design of the test-loop. In the model as seen in Figure 3.3, the domain considered upstream is the geometry situated before the Venturi section. To evaluate different design options, the vertical length of the upstream piping between the Venturi and the blind-T was parametrized. This length will henceforth be titled the vertical entrance length (VEL). In addition to this, the depth of the downstream blind-T was parametrized.

Lastly, since the outflow conditions where unknown the outlet boundary had to be situated far away from the region of interest. Thus an additional vertical downstream length of 10 inner diameters (ID), was added. The final, cleaned-up flow

domain imported to STAR-CCM+ can be viewed in Figure 3.3 where the blue parts are the computational domain and the transparent volumes are external geometry to be ignored in the simulation.

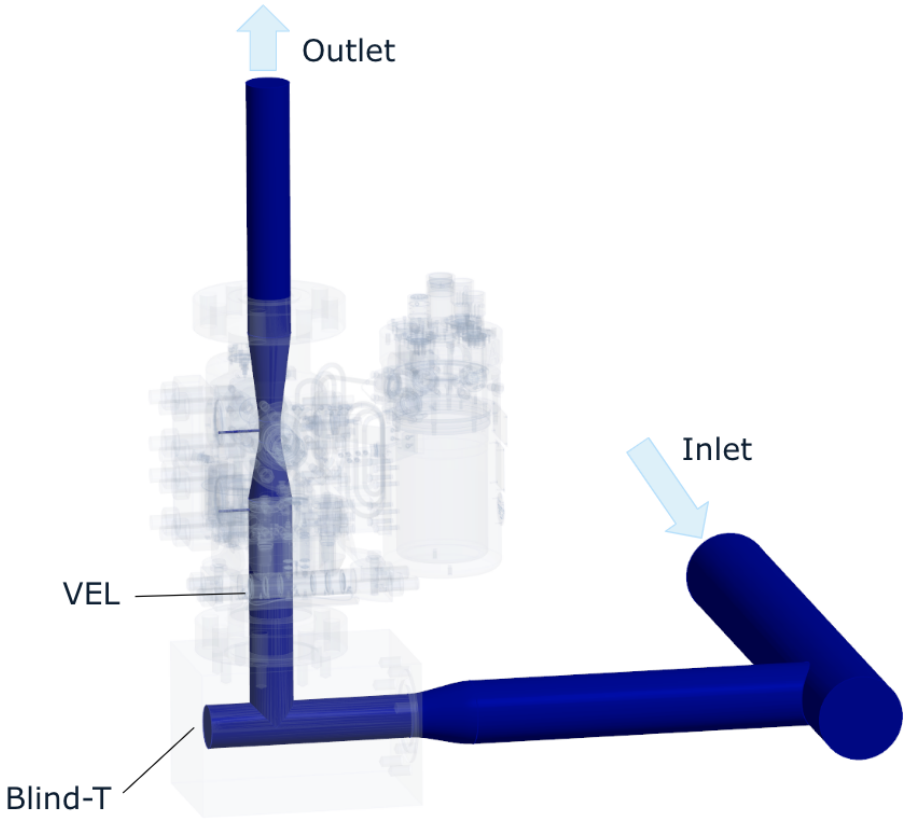

Figure 3.3: Cleaned geometry in STAR-CCM+

3.3.2 Solver Set-Up

Table 3.1 is an overview of the different models that were implemented in the set-up of the CFD model used in this project.

Table 3.1: Models used in STAR-CCM+

Time Solver	Implicit Unsteady
Flow Solver	EMP, Segregated URANS
Turbulence Models	RANS (k-ω, SST k-ω) + Wall Treatment
Thermal Solver	Segregated Fluid Isothermal
Phase Interaction	Continuous-Dispersed Topology
Material Properties	Gas: Ideal Gas, Liquid: Constant Density

In the test loop, the multiphase flows were affected by uneven geometries such as

blind-Ts, as well as convergent- and divergent pipe sections. Therefore, the implicit unsteady solver was implemented as it is suitable for capturing transient phenomena in multiphase flows. In the implicit unsteady solver, the time step could be set. Test simulations showed that this parameter was extremely important for the stability of the CFD solution. The chosen time step for the time model solver was found to be critical. A range of different time step values were tested, and a stable one found was 1.0E-4s.

The Eulerian Multiphase model was used because it is a well-proven, robust multiphase model widely utilized in the industry. It is effective at simulating flows where the phases interact with each other and for continuous-dispersed flows where distinct changes in the dispersed phase is common throughout the simulation. The URANS solver offers a practical compromise between accuracy and computational cost, making it a suitable choice for capturing the unsteady dynamics of turbulent multiphase flows. Another important parameter considered was the interaction between the dispersed and the continuous phase in the multiphase flow. For this project, the GVF values were kept very high at all times, and thus, the continuous-dispersed topology was considered sufficient.

The turbulence models listed in Table 3.1 were implemented because they are widely recognized for their accuracy in predicting turbulent flows, especially in near-wall regions and for flows significantly affected by pressure gradients. Additionally, the SST model utilizes a combination of k-ω and k-ϵ, making it favorable for boundary layer simulations.

For the material properties, the gas was modeled as an ideal gas to ensure its density would be calculated based on the local pressure, given the significant and rapid pressure changes in the Venturi section. This approach ensured that the gas behaves realistically. However, since the density and viscosity of liquids typically do not show significant effects from pressure changes, these parameters were kept constant for each simulation, thus applying a constant density. The ideal gas model requires a thermal model to compute the gas density, so a segregated fluid isothermal solver was used. Since heat transfer was not of interest for this study, this model was suitable to support the ideal gas solver.

3.3.3 Boundary conditions

The settings used for the solver in the CFD model and the boundary conditions enforced correspond to the options available in the commercial CFD modeling software STAR-CCM+. In this section, the boundary conditions used will be elaborated.

Inlet

In order to adapt the simulation inlet conditions to more accurately represent the physical test-loop a blended inlet was constructed. As can be seen in Figure 3.1 the mixing of the gas and liquid happens at a vertical section of the inlet pipe. In the CFD simulation, the inlet starts further downstream in the horizontal pipe section

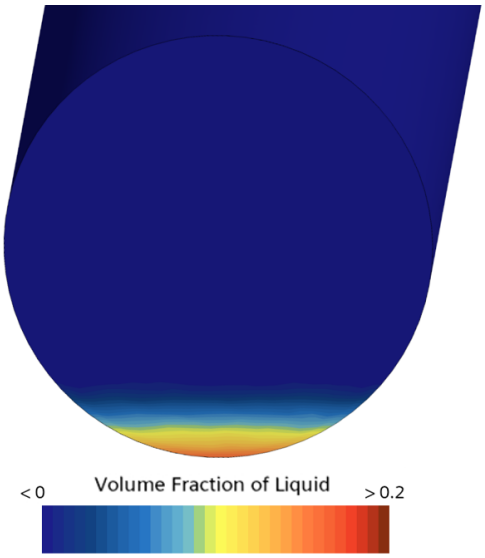

Figure 3.4: Blended Inlet

as can be seen in Figure 3.2. At the horizontal section the flow was assumed to be stratified, although some mixing was still expected since the liquid had dropped down the vertical section of the pipe. The blended inlet assumes a liquid hold-up of 0.8 at the bottom of the pipe, which then linearly decreases to 0 at the liquid-gas interface. The height of the liquid-gas interface was determined such that the desired liquid volumetric flow rate at the inlet was satisfied, given an assumed gas-liquid slip-ratio of $SR = 1.3$. The blended inlet function can be summarized as follows:

$$\begin{cases} \alpha_{liquid} = kh + 0.8 \ , \ 0 < h < h_{inerface} \\ \alpha_{liquid} = 0 \ , \ h = h_{inteface} \\ \alpha_{liquid} = 0.8 \ , \ h = 0 \end{cases}$$

where k is a coefficient and h is the height distance away from the pipe bottom. An example of a blended inlet implemented in star-CCM+ is shown in Figure 3.4

The boundary at the inlet was set to a mass flow inlet, enabling each phase to have a constant flow input. This allowed for precise control of the mass flow rates, which ensured good stability for the simulation. Additionally, the blended inlet function was used as a volume fraction field function for the physics value of the volume fraction boundary, allocating were each phase's mass flow should be situated.

Lastly, the surface tension was dependent on the operating conditions in terms of pressure and temperature. Thus, it had to be recalculated when the named quantities changed significantly. The equation used form the prediction of the surface tension was Equation 2.1.

Pipe wall surfaces

For the walls in the model, the boundary type was set to adiabatic wall with no-slip condition. The wall boundaries are crucial for capturing the flow behavior near the walls. This ensures that the boundary layer effects are captured.

Outlet

The outlet was set to a pressure outlet because it has proven to be a good boundary for flow stability. It effectively handles reversed flows, which are common in multiphase flow simulations. This boundary makes it easier to control the flow behavior and ensure that the simulation remains stable.

3.3.4 Mesh

In this study, mesh generation was hard and time-consuming due to the unpredictable dispersed phase behavior, as well as the unknown flow regime inside the test-loop. Due to this, a relatively fine mesh was used from outset and later on a grid independence study was conducted to evaluate if the mesh could be coarsened while maintaining adequate fidelity.

For this study, the mesh for the whole domain was generated using polyhedral elements. The reason for choosing polyhedral elements is due to their superior resolution of gradients. Polyhedral cells have more neighbors which results in better approximation of the gradients. This is highly desirable for this study, as large gradients are expected at the walls of the test loop, and the rapidly changing flow conditions cause the flow to not align with the mesh grid. Additionally, these element shapes require less time to generate an accurate solution compared to, for instance, a tetrahedral mesh with the same level of accuracy [28] [29].

Since different parts of the test loop had varying circumferences and significance for the study, the mesh had to be adapted accordingly. Therefore, a combination of volume and surface refinement controls was applied to generate the desired mesh. The mesh resolution was designed and adapted to resolve the relevant physics in the different parts of the domain, with a focus on the parts investigated in this study.

Apart from the mesh adaptions for the varying area of the piping, the boundary layers at the walls must be accounted for. In the test-loop high fluid velocities were present, and possibly a liquid film had to be resolved. In order to achieve this, a boundary layer mesher was needed to be utilized. The boundary layer mesher was used to capture the behavior of the flow near the solid walls of the domain. Due to the no-slip condition at the wall there were also large velocity gradients present in this region. Due to high flow velocities and the potential formation of a liquid film, these layers become even more important as they ensure the mesh is refined enough to capture the necessary details. For this model a wall treatment model was used, which ensured that the prism layers generated were within an acceptable range. The

first accepted mesh generated can be seen in Figure 3.5.

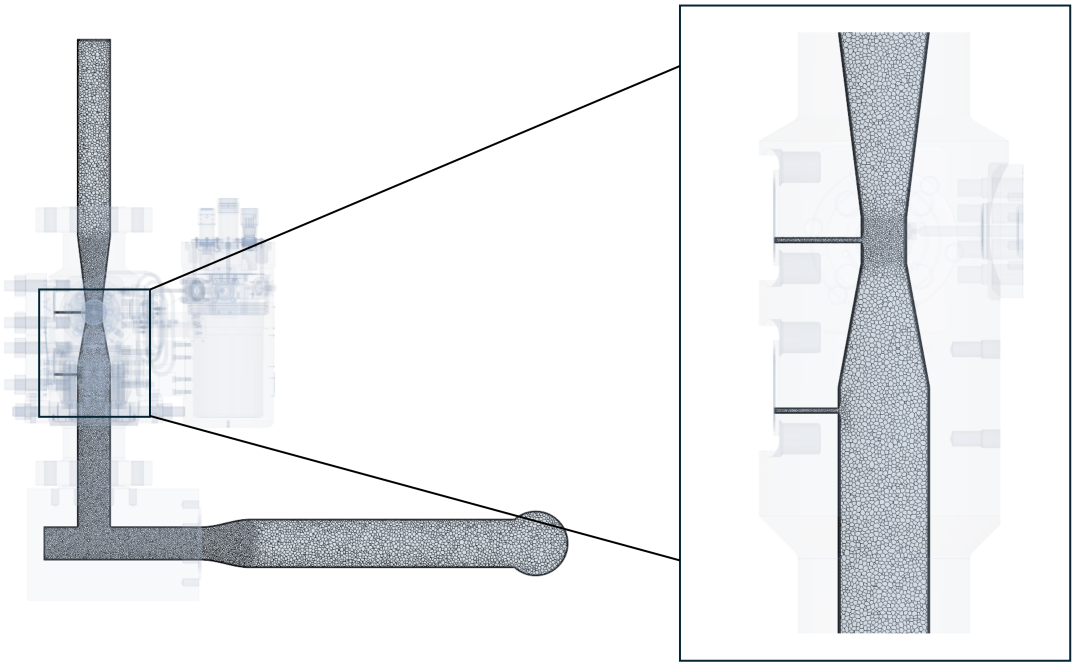

Figure 3.5: Mesh before refinement study

In order to evaluate whether the mesh generated is of good quality, the skewness angle, face validity, cell aspect ratio, and volume change are examined. These parameters were evaluated using the built-in field functions in STAR-CCM+, ensuring that they conform to appropriate values as explained in Section 2.3.1. In-house studies have conducted benchmarking studies to ensure the mesh has good quality. The study suggests that there should be no cell that has:

- Cell aspect ratio < 0.01
- Skewness Angle $> 85°$
- Volume Change < 0.001
- Face Validity < 0.9

The resulting mesh did not violate any of these benchmarking values. The histogram plots of the quality parameters can be seen in Appendix A. In Table A.1 the total cell count, base size and CPU time is presented for Mesh 1.

3.3.5 Mesh Refinement Study

In order to validate the mesh and the solutions grid independence, a mesh study was completed. In addition to this, since the mesh generated was very fine and thus costly to simulate, the goal was to find a coarser mesh size to minimize computational cost. The mesh refinement method and results are elaborated in depth in Appendix A. The mesh refinement study indicates that the time-averaged mean values computed are independent from the different mesh sizes. Additionally, all tested meshes had a similar periodic behavior with the same dominant frequency

and minor variations in RMS magnitude. It could be concluded that the choice of mesh from the pool of tested meshes did not have a significant influence on the solution. Based on the results from the mesh refinement study, Mesh 2 in Table A.1 was selected.

The mesh selected based on the results from the mesh refinement study is shown in Figure 3.6.

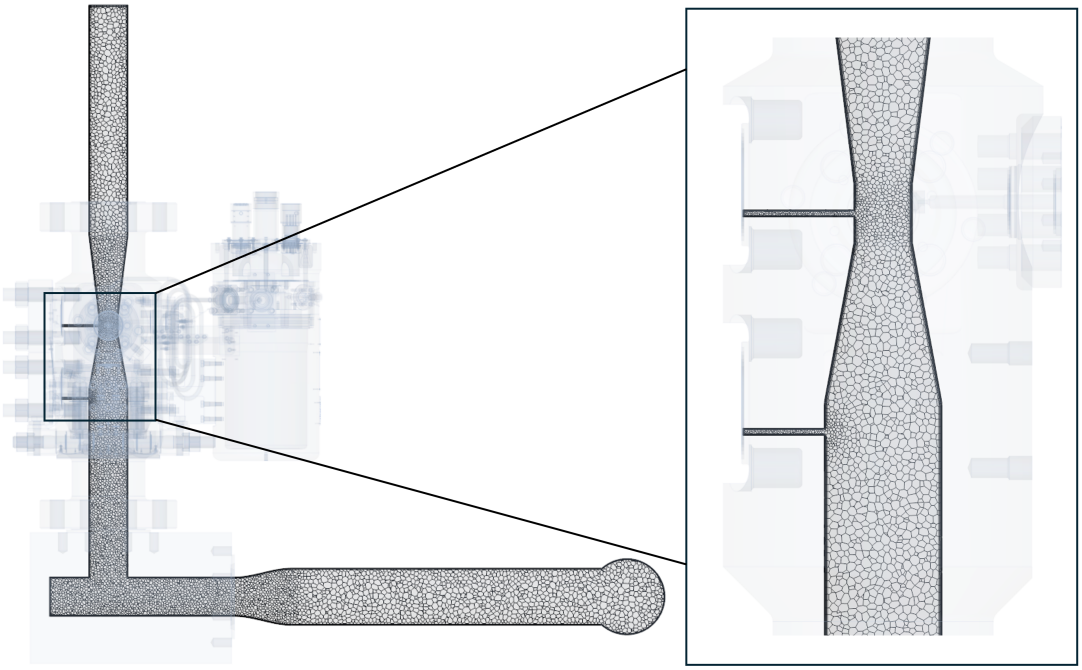

Figure 3.6: Final Mesh

3.3.6 Modeling of gamma-beam

The gamma-beam is represented in the model to review any differences between the measured phase fractions and the true phase fractions occupying the Venturi throat. The modeled gamma-beam is shown in Figure 3.7. In addition to the original gamma-beam as it was oriented in the physical test-loop, a second beam rotated by 90° was also added to evaluate any sensitivity in measurement accuracy related to gamma-beam orientation. In this model, control volumes of the same size as the actual gamma-beams were used to compute volume-averaged solutions for the measured hold-up.

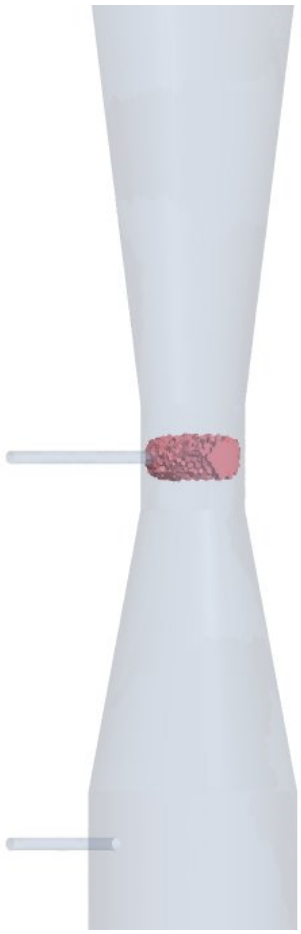

Figure 3.7: γ-beam modeled in CFD

3.4 Simulation validation

Before completing simulations with varying design parameters, the model had to be validated. In order to validate the CFD model, its results were compared to measurements from the physical test loop. This comparison ensured that the CFD model provided reliable results that accurately represented real-world physics. Validating the CFD model also reveals any limitations it may have. Additionally, comparing the CFD model to experimental data allowed for the customization of simulation parameters to achieve accurate results. Once the CFD model is validated and its results corresponded well with the test-loop measurements, it was considered trustworthy for continued simulations.

3.4.1 Selection of Experimental Data

To validate the CFD model, three experimental cases measured in the test- loop were selected featuring varying GVF, velocities, and pressures to ensure the simulations include different flow characteristics. Different operating conditions were selected to develop a robust CFD model capable of simulating flows under various scenarios. Given the project's limitation to simulate two-phase flow, test cases with two-phase

flow were chosen. However, the liquid phase in the test varied to capture different liquid properties in the validation study. Nitrogen gas was used as the gas phase for all test cases. The mean flow characteristics for these three test cases are summarized in Table 3.2. The pressures in the table are measured at the locations indicated in Figure 3.1.

Table 3.2: Validation cases measured in test-loop experiments

Case	Liquid Phase	ρ_{liquid} [kg/m^3]	$V_{mix,throat}$ [m/s]	p_0 [bar]	p_1 [bar]	p_2 [bar]
A	Oil	809	54.0	27.41	27.28	26.53
B	Water	999	80.1	29.48	29.03	25.50
C	Oil	809	113.6	29.38	28.71	25.05
Case	GVF [%]	$\dot{m}_{gas}$ [kg/s]	$\dot{m}_{liquid}$ [kg/s]	T [K]	ν_{liquid} [Pa s]	
A	97.29	3.40	2.47	289.05	0.00173	
B	91.59	4.53	14.02	290.95	0.00106	
C	96.53	6.68	6.64	290.0	0.00169	

3.4.2 Convergence

In the simulation, convergence was monitored in order to ensure stability and accuracy in the solution. It was based on the residuals of the governing equations such as continuity and momentum. In this project the time-step is considered converged when the residuals show no significant fluctuations over several iterations and the residuals have dropped to low values after each time-step. To achieve this, a high amount of inner iterations was set at the first second of the simulation, and was subsequently lowered. Additionally, iteration error estimates for the conservation of mass were examined for both the liquid and gas were used to evaluate convergence.

3.4.3 Comparison to Empirical data

In order to validate the simulation, flow cases and boundary conditions matching the selected experimental test cases in Table 3.2 were simulated. Here the simulated geometry closely resembles the test loop piping. The simulation result from the monitoring probes was then compared to the empirical data from the sensors in the test loop. When an acceptable match was achieved the model was considered validated. The CFD model was compared to the test-loop measurements in terms of mean values, as well as in the spectral analysis.

Mean values

When comparing the mean values, quantities listed in section 3.2 were compared between the CFD model and the experimental measurements from the test-loop. Since multiphase simulations are very sensitive to the simulation set-up and have a lot of uncertainty, a maximum of 10% error margin was allowed between the CFD

simulation and experimental measurements. If all simulation quantities compared conform to this requirement, the simulation set-up could be considered validated in terms of mean values.

Spectral analysis

Spectral analysis was completed for the validation cases, where measurements from both the test-loop and the CFD simulations were analyzed and compared. This is in order to evaluate how well the CFD-model captures oscillatory flow phenomena observed in the test-loop. In the test-loop the pressures were sampled at a too low frequency to be compared to the CFD data. This is discussed in further detail in section 5.3.1. Therefore, only the GVF spectrum was compared between the test-loop and the CFD validation cases. The method for obtaining the spectra from the physical test-loop and CFD data is described in sections 3.2.3 and 3.6.4 respectively.

3.5 Design Simulations

Once the model was validated the geometry and operating conditions could be manipulated in order to investigate the sensitivity of the MPFM to these parameters. The parameters that were controlled are summarized in below 3.3. All other parameters and settings were kept the same as in validation case A. The Blind-T and VEL parameters tested are in units of pipe inner diameters (ID). Parameters marked with * have the exact same value as in validation case A.

Table 3.3: Test matrix for Design Simulations

Design Parameter	Tested values	Test name
Blind -T depth	0.5 ID	0.5 ID blind-T
	1 ID*	1 ID blind-T
	3 ID	3 ID blind-T
VEL	3 ID	3 ID VEL
	4.8 ID*	4.8 ID VEL
	7.2 ID	7.2 ID VEL
Pressure	29 bar*	Low Pressure (LP)
	75 bar	Intermediate Pressure (IP)
	150 bar	High Pressure (HP)
Liquid Viscosity	1.7 cP	Low viscosity (Lmu)
	17 cP	Intermediate viscosity (Imu)
	117 cP	High Viscosity (Hmu)

In the above cases, a cross-section of the Venturi throat was monitored to evaluate the position of the gamma-beam in relation to the phase fraction distribution ,

both instantaneously and in the mean field. The blind-T's were also monitored to investigate their influence on flow behavior, specifically in terms of vortex shedding and plugging.

3.6 Post processing

In order to evaluate the results, and draw conclusions based on these, some post processing of the CFD results was required. The post-processing methods used for this are elaborated in this section.

3.6.1 Evaluating MPFM accuracy

In the control volumes representing the gamma-meters, the hold-up was computed for two gamma-beams. The first beam was oriented as in the original MPFM geometry, while the second was with an angle of 90°, as explained in section 3.3.6. To evaluate how well the gamma-beams capture the fluid composition in the throat, the measured hold-up was compared to the GVF in the Venturi throat. The GVF was computed by evaluating the mass flow and phase densities passing through a plane located in the center of the gamma-beams to generate the volumetric flows, which then were converted into GVF. The comparison was done by taking the percentage difference between the gas hold-up of the fluid occupying the gamma-beam control volume and the GVF computed from the plane in the gamma-beams. Using this comparison, the accuracy of the gamma-beam could be evaluated for the different flow and design test cases.

In the above described method, gas hold-up and GVF are compared, which is not entirely accurate due to their differing definitions. However, given the constraints of this study and the absence of alternative methods, this approach is deemed acceptable.

3.6.2 Angle of liquid distribution in Venturi throat

The homogeneity and distribution of the liquid phase in the throat will significantly affect the MPFM accuracy in capturing the flow conditions. Therefore, evaluating the time-averaged mean distribution angle of the liquid in the throat was crucial to determine the optimal placement of the gamma-beam. To compute this angle, the coordinates of the liquid's center of gravity in the Venturi throat were assessed. This centroid represents the average position of the weighted distribution of the liquid. The centroid was weighted by the mean volume fraction of liquid, which accounts for the varying cell sizes. Consequently, cells of different sizes with the same liquid volume fraction were weighted by their size, ensuring that their importance is accurately represented.

After establishing the coordinates of the centroid, trigonometry was employed to calculate the angle where the highest concentration of liquid was located. Additionally, by considering time, a time-averaged displacement angle was determined

to indicate the typical angle at which the liquid was situated. This method provides a reliable suggestion for the optimal angle at which the gamma meter should be placed. The same kind of approach was done in order to evaluate at what radius the centroid is located. By evaluating both the angle and the radius from the center of the throat it was possible to predict whether the flow showed homogeneous behavior or not.

3.6.3 Slip-Ratio

To gain insight into the slip between the gas and liquid phases, the Venturi throat was monitored for slip between these phases. Differentiation is made between slip in the liquid film on the wall and the dispersed liquid. The slip ratios evaluated are defined below:

$$SR_{overall} = \frac{V_{gas}}{V_{liquid}}$$

$$SR_{liquidfilm} = \frac{V_{gas}}{V_{liquid,film}}$$

$$SR_{dispersedliquid} = \frac{V_{gas}}{V_{liquid,dispersed}}$$

The continuous phase, i.e. the liquid film, is defined in the CFD model using a threshold where, if the LVF is higher than 0.7, the liquid phase is considered continuous. Conversely, if the LVF is below 0.7, the liquid is considered to be in the dispersed phase.

3.6.4 CFD Spectral Analysis

The spectrum for the CFD data was obtained the same way for all CFD simulation cases, regardless if it was a validation case, mesh refinement study or a design simulation. From the simulation file, a sample of the quantity of interest in time was extracted excluding the initial transient at the start of the simulation run. The extracted samples were within the interval 4.5-12 s (45000-120000 samples). Using Welch's method and a flat top type window using Python's built-in function *scipy.signal.welch*, the signals were transformed to the frequency domain spectrum. Since the CFD simulation time step was 0.1 ms, the sample frequency becomes 10kHz. Considering that the sample frequency was very high, the loss in frequency resolution from the use of Welch's method and the flat top window was considered negligible. The selected number of signal segments was 2 with the default 50% overlap, as this gave a satisfactory amount of smoothing of the spectrum without too much smearing. Typically in multiphase flow, oscillations between 0-10 Hz are of interest, therefore frequencies in this interval were studied here.

All spectrum plots shown in the Results section are normalized using the maximum amplitude recorded in the study in question. For cases compared within a single spectrum, the same amplitude is used for normalization.

3.6.5 Visualization

In this paper, various visualization techniques were used to analyze the computed solutions effectively. The primary methods for presenting the results included vector scenes, scalar scenes, and resampled volumes. Vector scenes were used to evaluate the flow direction inside the blind-T, helping to better understand flow patterns and the impact of design changes. However, these scenes do not account for the magnitude of the vectors but instead provide insight into the flow behavior. Scalar scenes were used to visualize quantities such as LVF and slip velocities, among others. In these scenes, the color bar, which represents the range of magnitude for values, was adjusted to simplify the representation of the solution. Specifically, the color bar for LVF was set to display values between 0 and 0.2. This adjustment was necessary because the GVF is very high, and lower values of LVF would otherwise be barely visible. Lastly, resampled volumes were used to enhance the visualization of volumetric data, such as displaying the flow of liquid in 3D.

4

Results

In this chapter the results gathered in this project are elaborated. Results pertaining to the simulation methodology and validation are presented, as well as the MPFM sensitivity study. The slip observed in the MPFM is also presented.

4.1 Review of experimental data

In this section, the results gathered from the experimental measurements in the test-loop are elaborated.

4.1.1 Extraction of Experimental data

For each test-case, the raw test-data is post-processed as described in section 3.2.2 in order to extract the GVF. In Figure 4.1, a short time interval of the detected GVF for case A is shown. The blue dots represent instantaneous GVF readings, while the red line indicates the GVF rolling average with a 1 second window. As can be seen, the signal is very noisy for reasons explained in section 2.2.3. Some averaging is therefore necessary to obtain a meaningful GVF output.

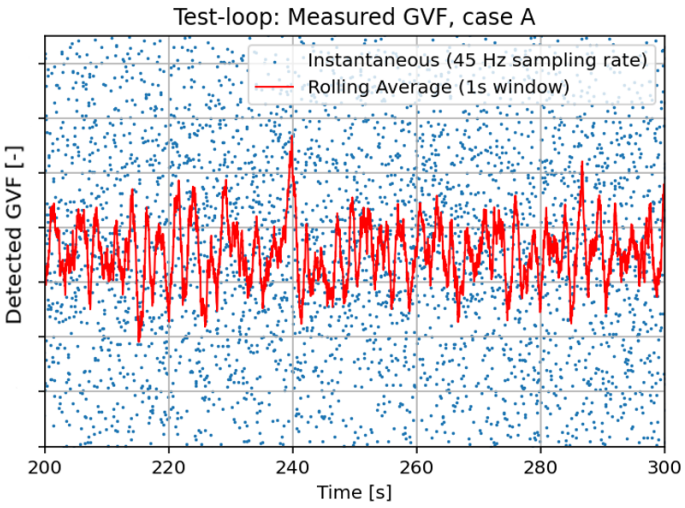

Figure 4.1: Validation case A in the test loop, detected GVF plotted in time

4.1.2 Spectral Analysis

The detected GVF for all three validation cases measured in the test-loop are plotted in the frequency domain in Figure 4.2. The GVF is transformed to the frequency domain using the method described in section 3.2.3. The spectrum is then normalized by the maximum amplitude recorded in the GVF spectrum in Figure 4.5 obtained from the CFD simulation of the validation cases, for comparison purposes. As shown in Figure 4.2, there are clear peaks for the dominant frequencies. Case A has a dominant frequency at approximately 0.4 Hz, and Case C at approximately 0.7 Hz. Case B does not exhibit dominant frequencies with amplitudes as high as those in the other cases.

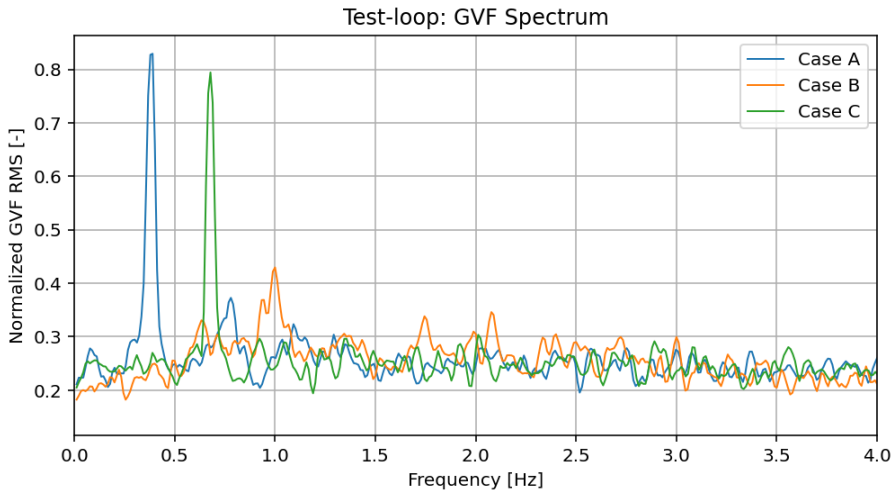

Figure 4.2: All validation cases in the test loop, detected GVF spectrum normalized together with Figure 4.5

4.2 Simulation Validation

In this section, the results regarding the simulation validation are elaborated. The validity of the simulation is evaluated by comparing the mean values of selected flow parameters to the test-loop measurements, as well as comparing the simulation- and test-loop data in the frequency spectra.

4.2.1 Quality of CFD model

The mesh refinement study shows that all meshes generated followed good practice and did not violate any mesh quality threshold values based on skewness angle, cell aspect ratio, face validity and volume change. The results from this quality and refinement study are displayed in figures A.4, A.3c, A.4c and in Appendix A.1.2.

When running the simulations, convergence of the residuals were carefully monitored. As simulation time progresses and the initial state relaxes the number of inner iterations was gradually reduced. Continuity was monitored by evaluating the total error of mass per phase together with the error in mass per iteration. The resulting mass error plots for Case A are displayed in Figures 4.3 and 4.4.

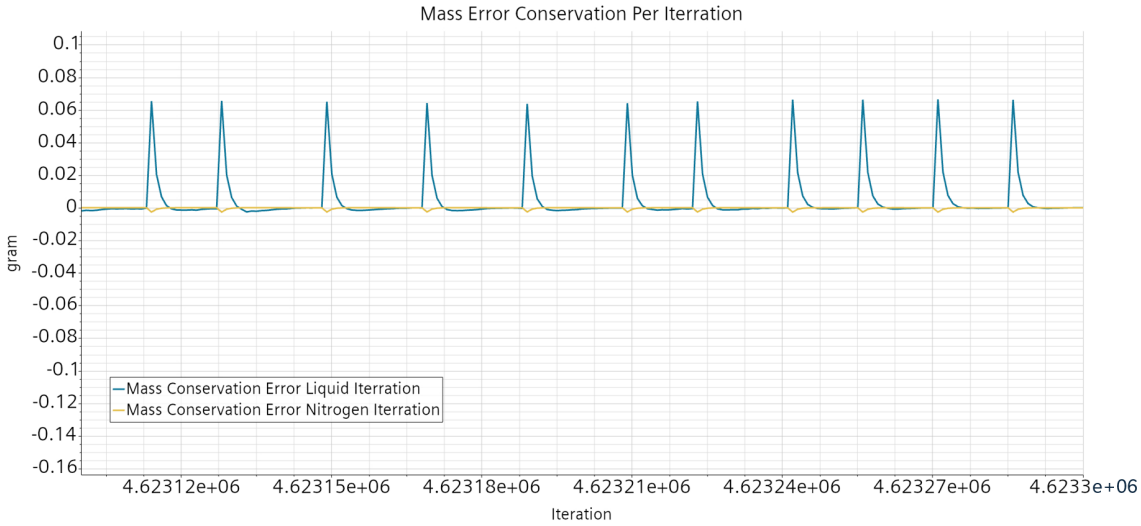

Figure 4.3: Overview of mass error per iteration.

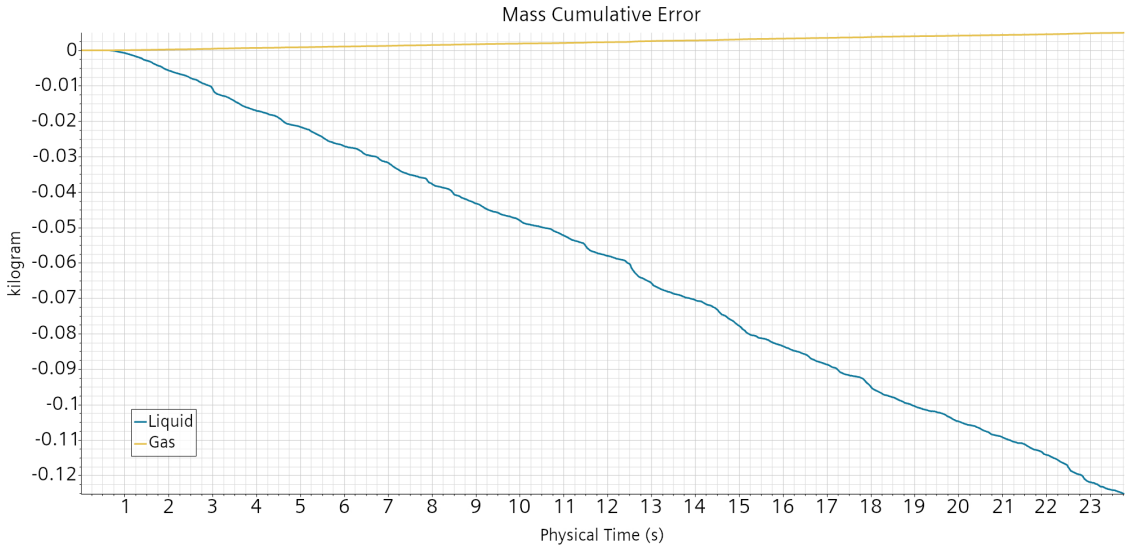

Figure 4.4: Cumulative error in mass.

For case A, the total loss in liquid mass was, 0.125 kg, this corresponds to a change in mass by 0.21% compared to the total inflow of liquid during this period of time. The gas instead increased in mass with 0.0045 kg which corresponds to an increase

of 0.0056% compared to total inflow of gas. All simulations showed the same behavior, minimal error in mass and valid error in mas per iteration.

In order to validate the CFD-model to physical measurements the simulation results are compared to results from experimental testing. The results from the comparison study between flow-loop experimental data and the time-averaged mean values from the CFD solution is presented below in Table 4.2.1.

Quantity	Case A	Case B	Case C
p_{Inlet}	0.27 %	0.34 %	-0.71 %
p_1	0.26 %	1.72 %	-1.11 %
p_2	0.44 %	3.15 %	-0.84 %
Δp	-7.37 %	-8.78 %	-2.99 %
GVF_{inlet}	0 %	0.14 %	0.05 %
$\rho_{\text{gas, inlet}}$	1.90 %	-1.43 %	-1.04 %
$\rho_{\text{gas, throat}}$	1.6 %	-0.36 %	-0.29 %
$\dot{Q}_{\text{gas, inlet}}$	-1.94 %	1.46 %	1.20 %
$\dot{Q}_{\text{liquid, inlet}}$	0 %	0.06 %	0.03 %
$\dot{Q}_{\text{gas, throat}}$	-1.33 %	-1.81 %	-1.62 %
$\dot{Q}_{\text{liquid, throat}}$	-2.46 %	1.48 %	-0.10 %

In order for the CFD-model to be considered validated, the maximum difference a time-averaged value was allowed to have was a magnitude of above 10% compared to the experimental data. As seen in the Table 4.2.1 all compared quantities conform to this requirement.

4.2.2 Spectral Analysis

The GVF spectrum in Figure 4.5 is extracted from the CFD simulation using the method described in section 3.6.4. The GVF spectra obtained from both the physica l test-loop and CFD simulation are normalized together using the highest amplitude recorded between the two spectra, which in this case is the GVF for case A simulated in CFD. The GVF in the CFD simulations is sampled across the entire throat, while in the experimental cases it is measured within the beam. Therefore, the comparison is not directly equivalent, but still indicative of the flow behavior and considered sufficient for the purpose of this study. Validation cases A and C exhibit clear dominant frequencies at approximately 0.75 Hz and 1.75 Hz, respectively. Case B also shows a dominant frequency at approximately 2.5 Hz, although its amplitude is lower than that of the other cases.

When comparing to the GVF spectrum for the physical test loop in Figure 4.2, it is evident that the amplitudes of the dominant oscillations obtained from the CFD-simulation have higher amplitude than recorded in the test-loop. Additionally, the frequencies for the physical test loop measurements are significantly lower,

below 1 Hz, compared to the dominant frequencies from the simulation data, which range between 0.75 and 2.5 Hz. It cannot be excluded that, with a longer simulation time the lower frequencies would be visible also in the CFD simulation results. This topic is further discussed in section 5.3.1. In summary, the simulation captures oscillations of similar amplitude as the test-loop, although at higher frequencies. Some trends are similar between the CFD and test-loop GVF measurements. In both the test-loop and CFD simulation, case A has the lowest dominant frequency and case B has the highest dominant frequency. Additionally, in both the simulation and test-loop, case C has a lower amplitude than the other test cases.

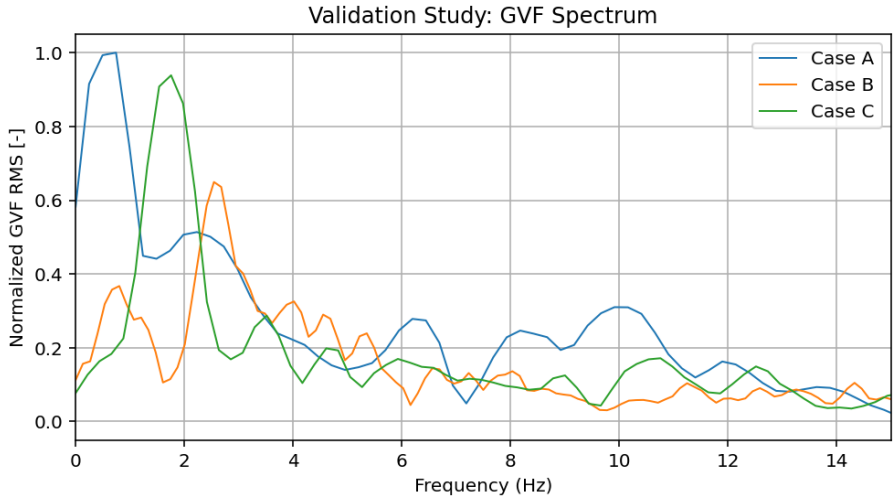

Figure 4.5: All validation cases simulated in CFD-model, GVF of fluid occupying Venturi throat spectra

4.3 Flow Characteristics in Original MPFM

In this section the general flow characteristics in the MPFM are described, both mean of field and instantaneous behaviors. Here validation case A, which is the basis for all design simulations, is discussed in further detail, so that all flow characteristics from the design simulations then can be compared to this case. Using the comparison, the MPFM sensitivity to the flow- and design parameters can be evaluated.

In Figure 4.6 the mean volume fraction of liquid over time is shown. Stratification of the flow is observed, as well as liquid accumulation in both blind-Ts. The liquid traveling up along the VEL from the downstream blind-T also shows stratification, with the liquid phase leaning towards the blind-T direction. Due to the liquid's significantly higher density compared to the gas phase, each turn in the flow risks separating the liquid from the gas, thereby hindering the desired mixing. The purpose of the blind-Ts is in part to mix the flow, but as can be seen only minimal mixing is achieved.

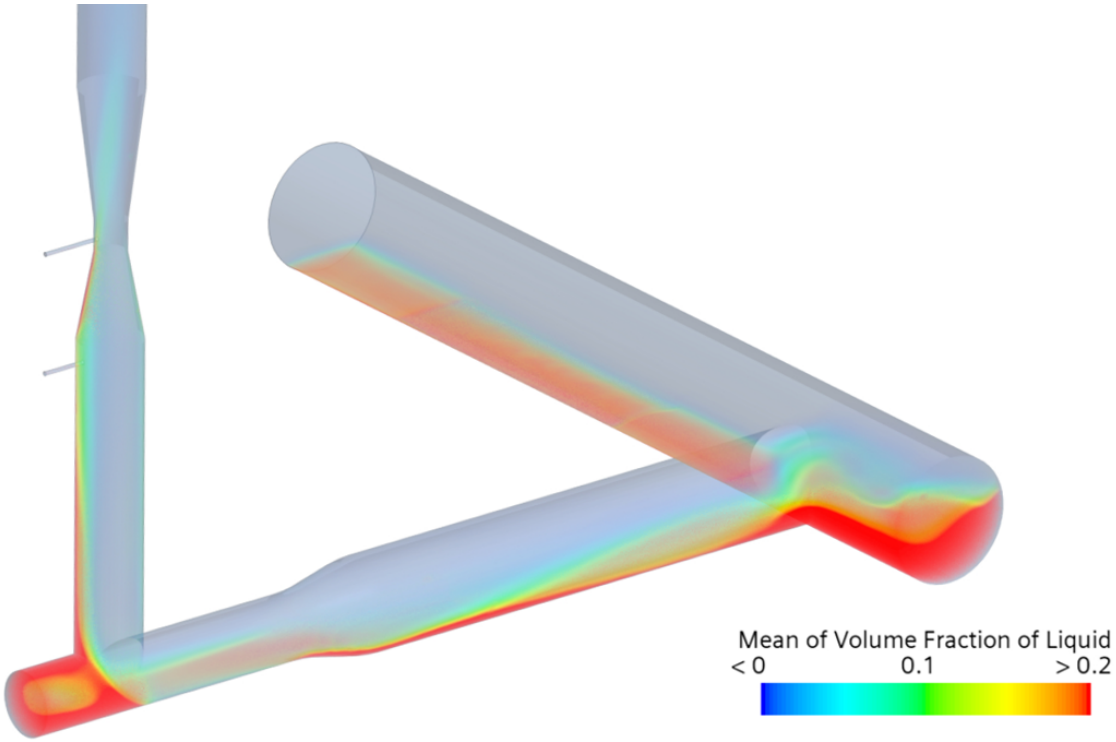

Figure 4.6: Liquid volume fraction mean of field, validation case A

In Figure 4.7, the instantaneous velocity field in the blind-T is shown. The blind-T is occupied by a vortex, which together with the accumulated liquid in the blind-T causes the shedding of plugs which travel upwards towards the Venturi throat. The liquid in the blind-T is close to stagnant as seen by the velocity magnitude in the recirculation zone.

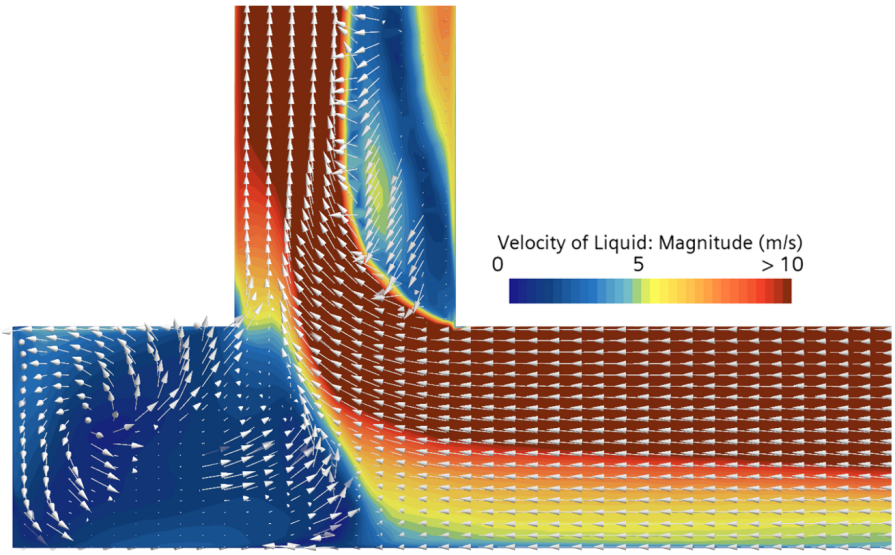

Figure 4.7: Instantaneous velocity field in the blind-T, validation case A

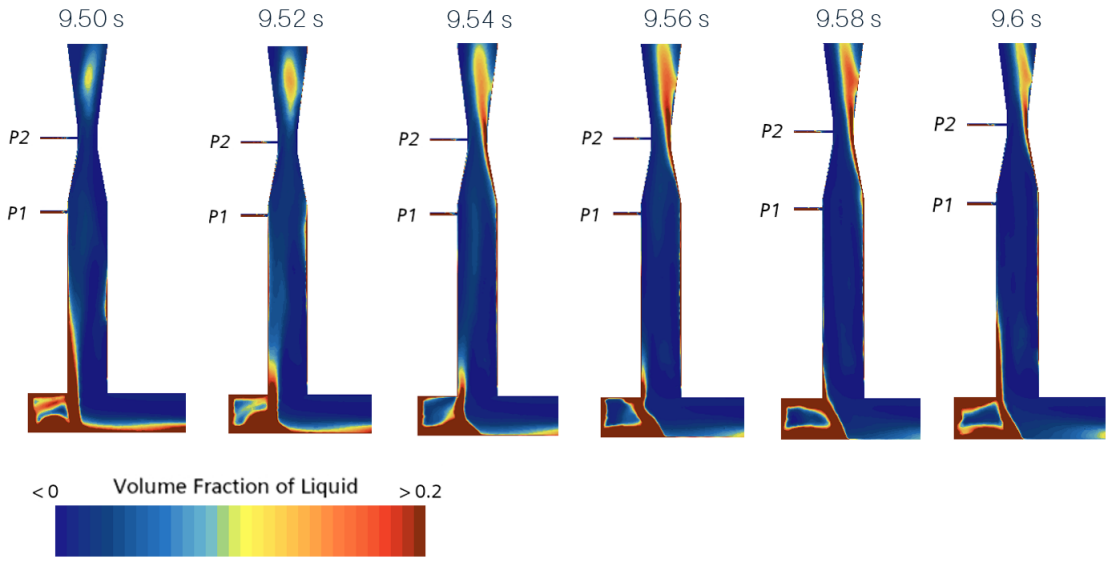

Figure 4.8: Instantaneous volume fraction of liquid over time, at a cross-section in proximity to the blind-T and Venturi throat, validation case A

In Figure 4.8 the instantaneous liquid volume fraction in the blind-T and VEL is shown. Accumulation of liquid in the downstream blind-T can be observed, as well as the liquid sloshing due to the circulation in the blind-T. The sloshing releases plugs of liquid traveling along the VEL into the throat. The plugs in the throat are visible in Figure 4.9, where the instantaneous LVF in the Venturi throat is visualized. The location of the plug varies substantially with time, although the plugs are always sticking to the pipe wall. The gamma-beam position is visible in the figures, and in some instances the gamma-beam completely fails to capture the plug.

The upstream blind-T significantly influences plug shedding in the downstream

blind-T. Due to its larger size, the upstream blind-T can accumulate more liquid volume, causing any released plugs to quickly overfill the downstream blind-T. This overfilling results in large plugs passing directly to the Venturi throat without initial mixing. This behavior is partially observed in Figure 4.8, where the instantaneous LVF in a cross-section of the Venturi throat is shown in time. At 9.50 - 9.54 seconds, the tail of a large incoming plug from the upstream blind-T can be observed bypassing the downstream blind-T mixing.

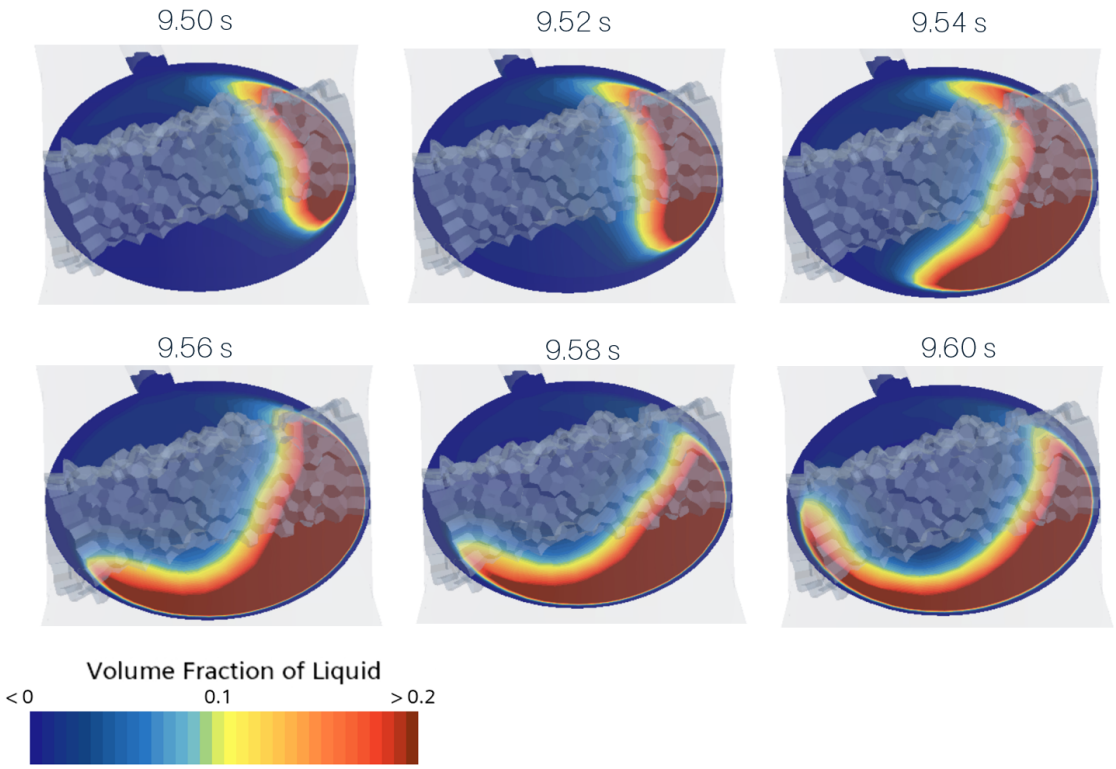

Figure 4.9: Instantaneous volume fraction of liquid in Venturi throat cross-section over time, validation case A

In Figure 4.10 the mean liquid volume fraction field, averaged over the entire simulation time is shown at a cross-section of the Venturi throat. The orientation of the gamma-beam is indicated with the light blue arrow in the throat, and the direction of the blind-T is indicated by the black arrow. The direction of the average liquid center of gravity is also indicated by the black arrow. The mean field indicates that the liquid phase is not homogeneous, with its center of gravity offset by 306° relative to the manometer and blind-T. Furthermore, the centroid was found to be located at 21.22% of the pipe radius away from the ideal center point of the throat. Ideally, the flow should be homogeneously distributed across the throat. Despite this, the gamma-beam captures most of the liquid phase, providing a representative measurement of the fluids in the throat.

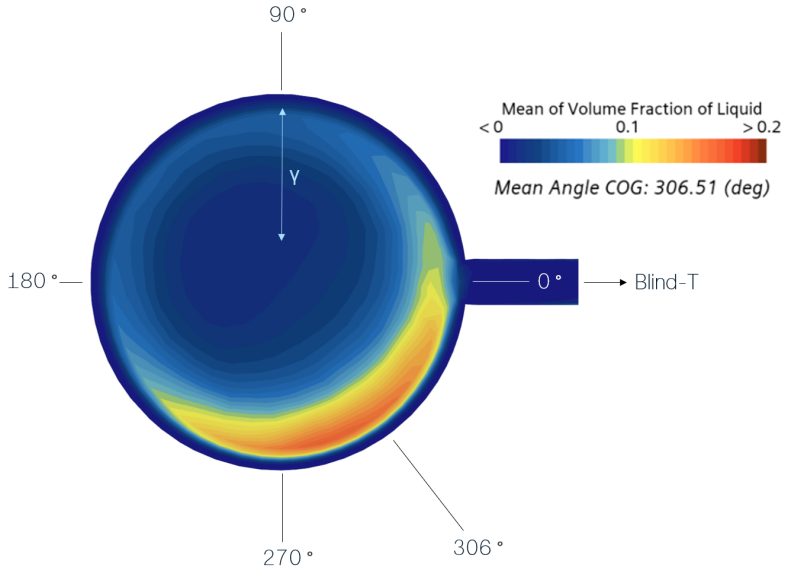

Figure 4.10: Liquid volume fraction mean of field in Venturi throat cross-section, validation case A

In Figure 4.11, the spectra of the GVF in the Venturi throat is plotted together with the gas hold-up spectra as detected by the gamma-beams. As observed, the gamma-beam oscillations are at higher amplitude than the GVF oscillations for the fluid occupying the entire throat. This is expected, as the sampling of fluid from a smaller control volume makes the measurement more sensitive to the local fluid composition. Sampling from a larger control volume will apply an averaging effect, thereby reducing the fluctuations in the measurement. However, the spectrum indicates that the orientation of the gamma-beam does not significantly influence the frequency or magnitude of oscillations in detected gas hold-up.

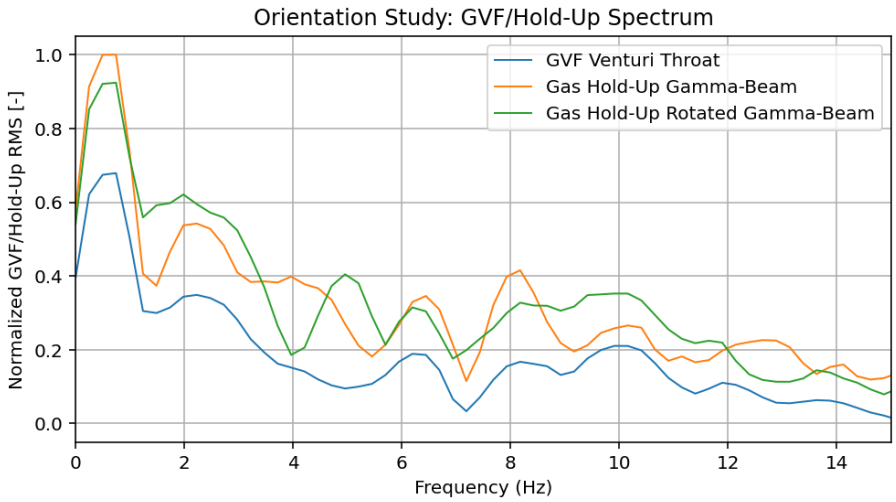

Figure 4.11: GVF and Gas Hold-Up spectra of fluids occupying Venturi throat at Gamma-beams

Slip-Ratio

The three different slip-ratios investigated and the results from the simulation is presented below in Table 4.1.

Table 4.1: Slip-Ratio Results.

Quantity	Value
Slip-Ratio Dispersed Liquid	1.38
Slip-Ratio Continuous Liquid Film	1.69
Overall Slip-Ratio	1.38

From the results it can be observed that the slip-ratio between the total gas velocity and the velocity of the dispersed face and the overall slip-ratio is the same. This suggests that the flow regime for the liquid phase is most likely dominated by dispersed liquid. The slip-ratio between the liquid film velocity and the total gas velocity is higher than both the overall and dispersed slip-ratio, but its contribution to the overall-slip ratio is insignificant due to low abundance of liquid in film.

4.4 Flow- and Design Simulations, Sensitivity Study

In this section, the results from the design-simulations are elaborated. The flow characteristics in the different test cases are compared to the original MPFM in validation case A in section 4.3, in order to evaluate the MPFM sensitivity to geometry and flow parameters.

4.4.1 Blind-T Depth Study

The GVF signals resulting from the CFD simulations are transformed to the frequency domain using the method described in section 3.6.4. The GVF signal is for the fluid occupying the entire Venturi throat control volume, i.e not as measured by the gamma-ray system but rather the true GVF. The * indicates the blind-T depth that matches the depth in validation case A, which corresponds to the original MPFM geometry. The resulting spectra are shown in Figure 4.12. As can be seen from the figures, the depth of the blind-T has some influence on the oscillatory behavior of the flow. The dominant frequency remains the same (approximately 0.75 Hz) regardless of blind-T depth, but the amplitude decreases with a deeper blind-T.

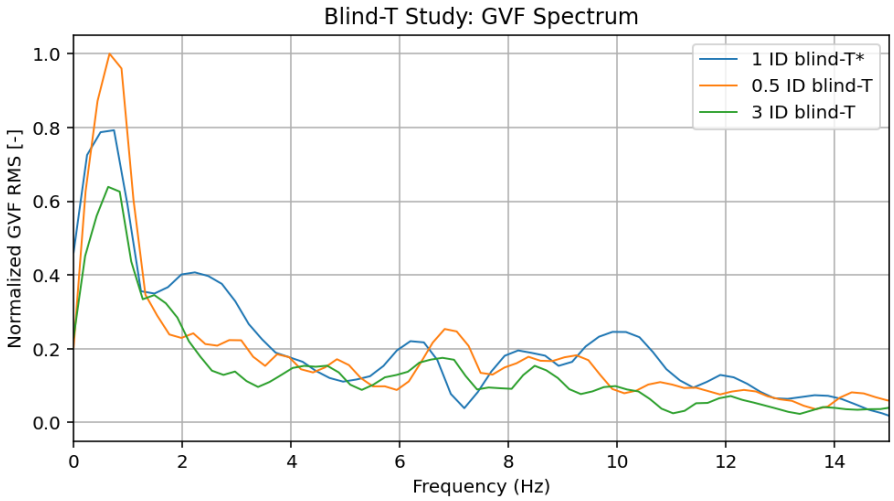

Figure 4.12: Spectra of GVF of fluid occupying Venturi throat, blind-T study

Table 4.2 presents the relative deviation between the measured volume-averaged hold-up value in the gamma-beam and the true value in the whole throat section. A mild trend is apparent, where the original beam has increased accuracy with a more shallow blind-T. The rotated beam, demonstrates an overall greater accuracy than the original beam.

Table 4.2: Results Blind-T depth study

Case	Hold-up Gamma Beam	Hold-up Rotated Gamma Beam
0.5ID	-1.14 %	-1.00 %
1ID	-1.20 %	-0.83 %
3ID	-1.22 %	-0.70 %

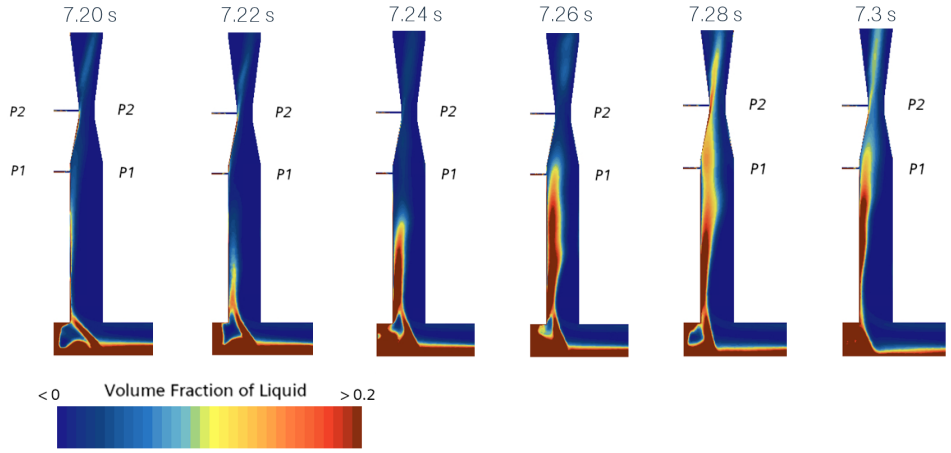

(a) 0.5 ID Blind-T

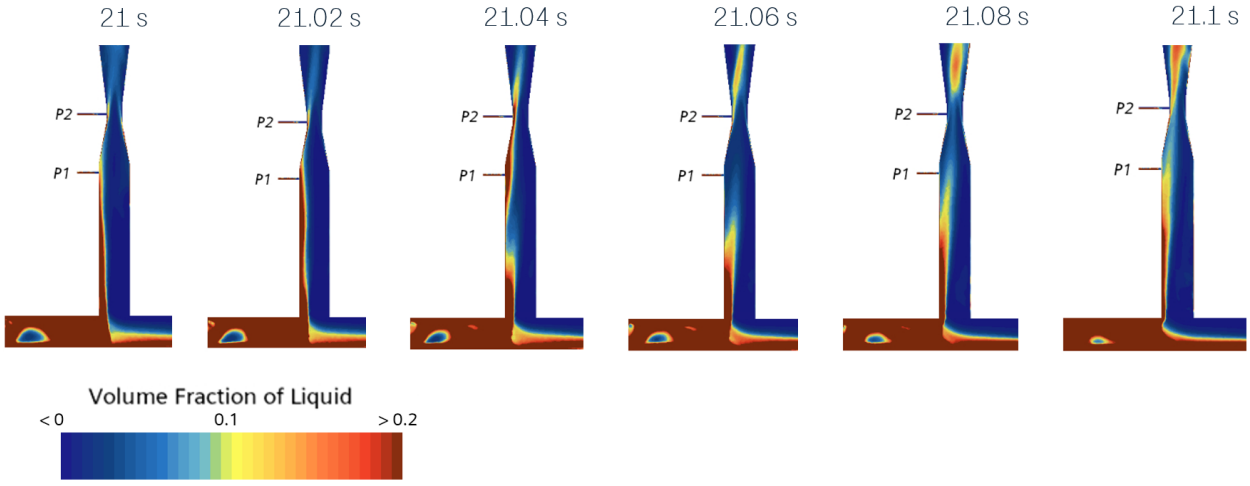

(b) 3 ID Blind-T

Figure 4.13: Instantaneous volume fraction of liquid over time, at a cross-section in proximity to the blind-T and Venturi throat, blind-T study

In Figures 4.13b and 4.13a, the instantaneous liquid volume fraction around the downstream blind-T is shown over time. As can be seen from the figures, the deep blind-T accumulates substantially more liquid than the shallow blind-T as expected. The center of the circulation zone in the shallow blind-T sits very close to bulk flow, and the plug shedding also occurs further out into the main bulk of the flow compared to the deep blind-T. This may cause greater instability in the flow and may explain the increased amplitude in the GVF spectra observed in Figure 4.12.

4.4.2 Vertical Entrance Length Study

The GVF signals of the fluid occupying the Venturi throat control volume obtained from the CFD simulations are transformed to the frequency domain using the method described in section 3.6.4, and are shown in Figure 4.14. The * indicates the vertical entrance length that matches the length in validation case A, which corresponds to the original MPFM geometry. As can be seen the VEL has some influence on the oscillatory behavior of the flow. The dominant frequency remains the same, although the GVF amplitude of the oscillations decreases slightly with a shorter VEL.

Table 4.3 presents the relative deviation between the measured volume-averaged hold-up value in the gamma-beam and the true value in the whole throat section. No clear trends are apparent for both meters, regardless of vertical entrance length or beam orientation. However, the rotated gamma-meter seems to more accurately capture the flow conditions with increased VEL.

Table 4.3: Results VEL study

Case	Hold-up Gamma Beam	Hold-up Rotated Gamma Beam
3ID	-0.91 %	-1.63 %
4.8ID	-1.20 %	-0.83 %
7.2ID	-1.14 %	-0.79 %

As can be seen from Table 4.3

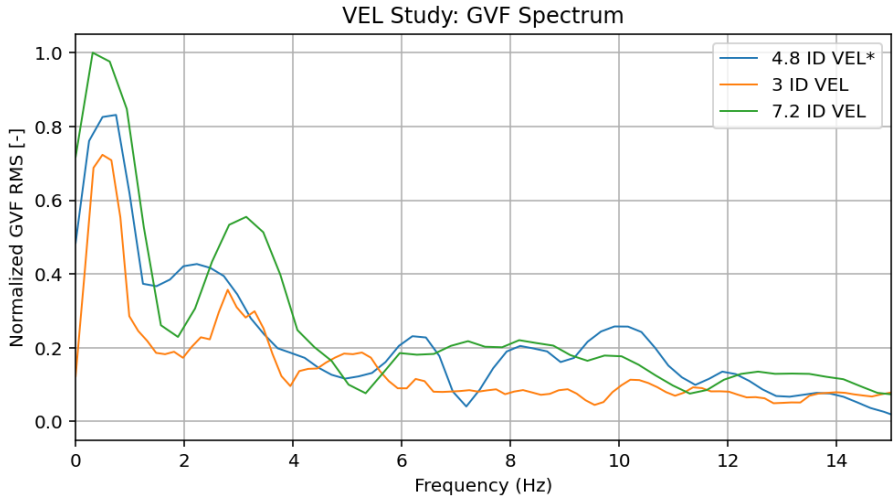

Figure 4.14: Spectra of GVF of fluid occupying Venturi throat, VEL study

4.4.3 Pressure Study

In Figures 4.15a and 4.15b, the mean volume fraction of liquid over time is shown for the intermediate- and high-pressure case respectively. By increasing the pressure, the gas density is much closer to the liquid density due to compressibility effects. Therefore, a much more homogeneous blend between the gas- and liquid phase is expected, which can also be observed in the figures.

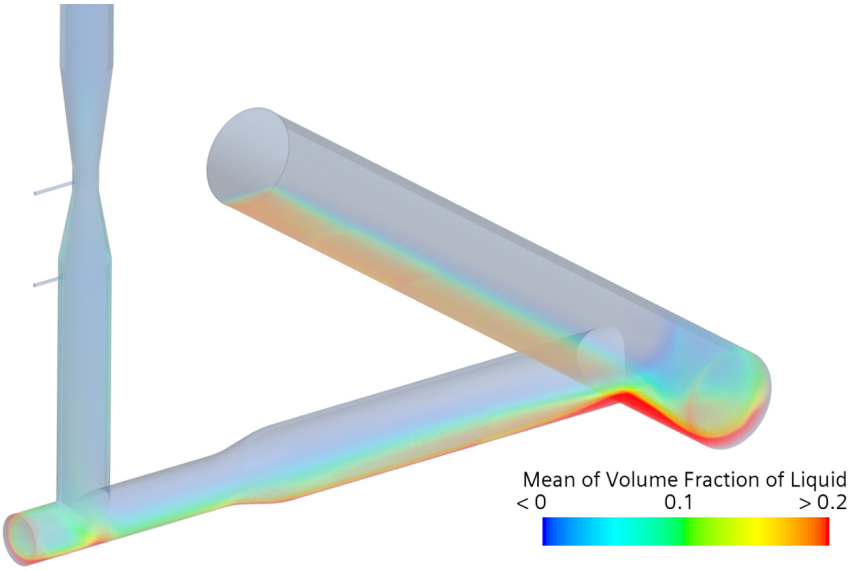

(a) Intermediate pressure test case

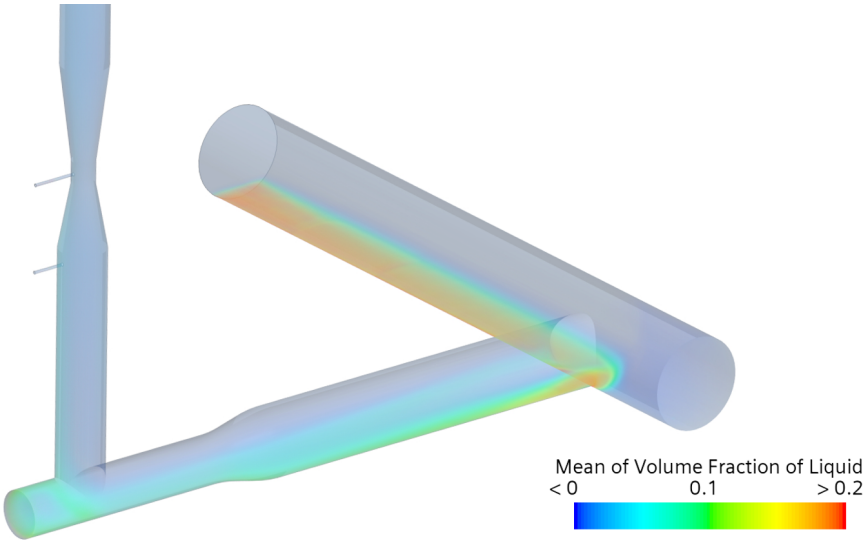

(b) High pressure test case

Figure 4.15: Liquid volume fraction, mean of field, pressure study

The intermediate pressure case shows more mixing in the two blind-T's compared to validation case A in Figure 4.6. In the VEL, greater homogeneity is observed in the intermediate pressure case compared to case A. In the high-pressure case, the fluid is even more homogeneous, and the plug shedding from both blind-T's has completely ceased. Both blind-T's mix the flow well, and less stratification is observed after the upstream blind-T compared to the intermediate pressure case. In the intermediate pressure case, some plugs can still be observed traveling downstream from the upstream blind-T.

Table 4.4 presents the relative deviation between the measured volume-averaged hold-up value in the gamma-beam and the true value in the whole throat section. It is observed that, regardless of beam orientation, accuracy increases with higher pressure. This trend aligns with the more homogeneous flow, enhancing the accuracy of the MPFM.

Table 4.4: Results Pressure study

Case	Hold-up Gamma Beam	Hold-up Rotated Gamma Beam
29 bar	-1.20 %	-0.83 %
75 bar	-0.02 %	-0.01 %
150 bar	0.14 %	-0.02 %

In Figure 4.16 the GVF spectra from the pressure study is shown. The * indicates the pressure that matches the pressure in validation case A. The increased homogeneity with higher pressure can also be observed in the GVF spectra, which manifests as an absence of a dominant frequency in the high-pressure case. A clear trend is evident: the high-pressure case exhibits significantly lower amplitude oscillations and no visible dominant frequency. The low- and intermediate-pressure cases have a dominant frequency at 0.75 Hz, with the intermediate-pressure case showing a lower RMS amplitude.

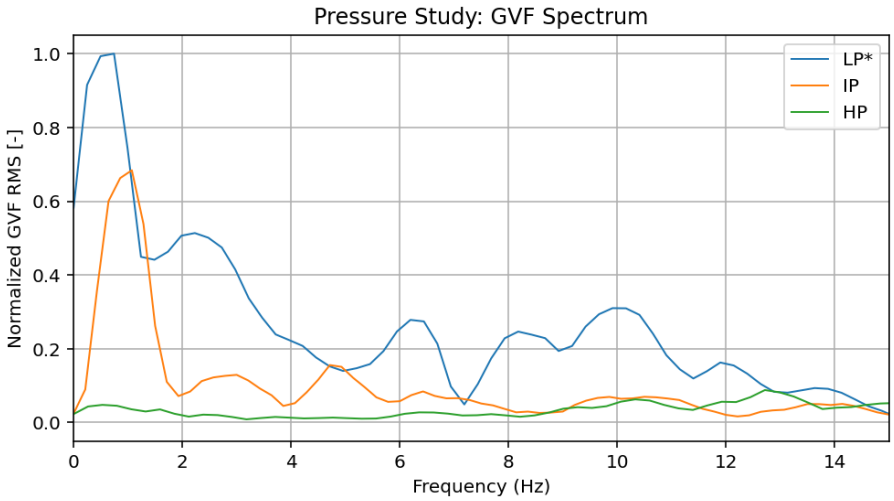

Figure 4.16: Spectra of GVF of fluid occupying Venturi throat, pressure study

In Figures 4.17a and 4.17b the LVF field is plotted in a throat cross-section for the intermediate- and high pressure cases respectively. The gamma-beam position is also visible in the figures. In the intermediate pressure case, the plugs can be seen sticking to the wall. The location of the plug varies substantially with time, and in some instances the gamma-beam completely fails to capture the plug. The overall flow characteristics are similar to the original validation case seen in Figure 4.8. In the high pressure case, the LVF field in the throat is significantly more homogeneous, which improves the performance of the MPFM. This can be attributed to the lack of plugs, and the liquid phase being dispersed in the gas.

This phenomena can also be observed when studying the Venturi throat in the mean LVF fields. The mean liquid volume fraction fields in the Venturi throat are plotted in Figures 4.18a and 4.18b. The direction of the average liquid center of gravity is indicated by the black arrow, and the direction of the gamma-beam and the blind-T are also indicated in the figures. As can be seen, the mean field of the intermediate-pressure case is more homogeneous than validation case A in Figure 4.10, although the LVF is still higher at the wall towards the manometer and blind-T direction. In the high-pressure the fluid mixture is significantly more homogeneous, with a slightly higher LVF towards the blind-T direction, similar to the other cases. In addition to this, the mean radial position of the liquid centroid from the center of the throat was evaluated. For the intermediate pressure case, the centroid was located at 6.29% of the throat radius, while for the high pressure case, it was slightly closer at 5.98% of the radius, also indicating a more uniform distribution.

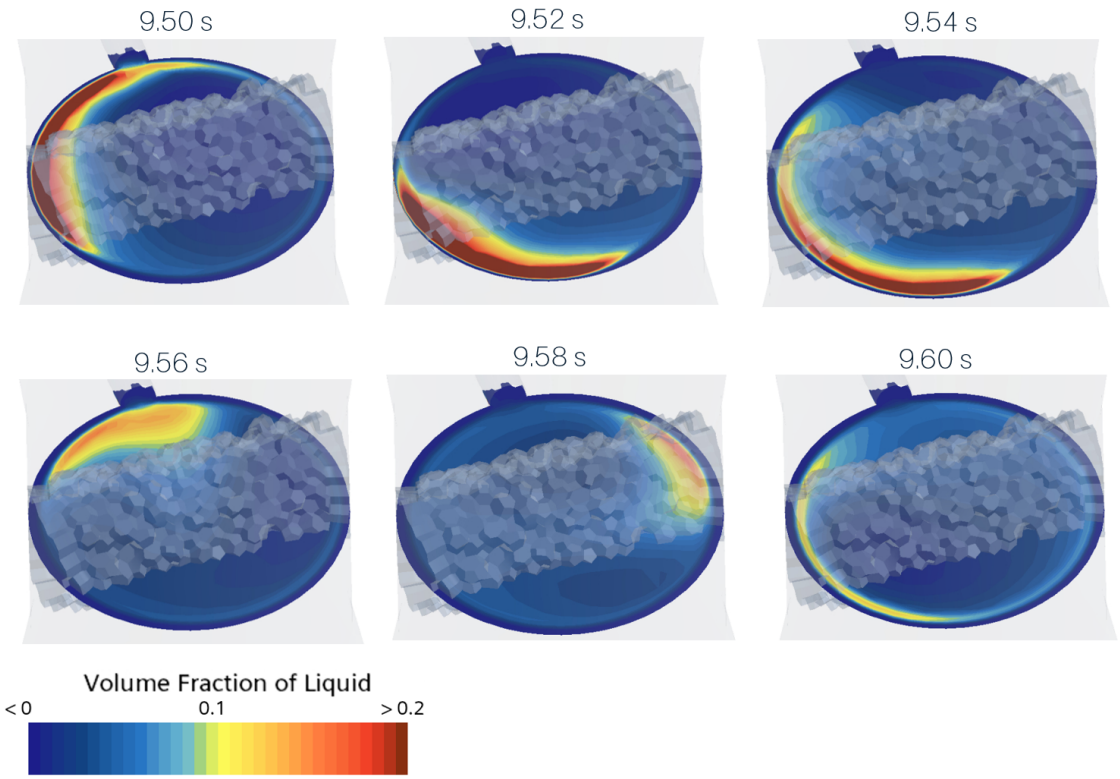

(a) Intermediate pressure test case

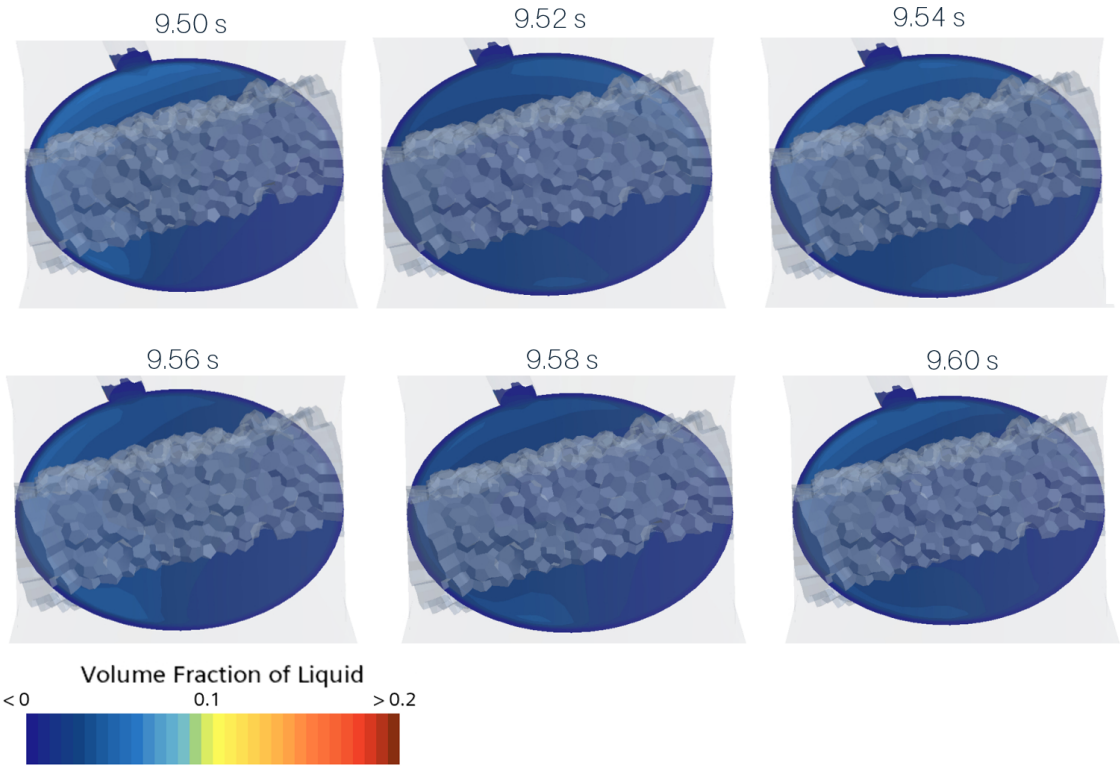

(b) High pressure test case

Figure 4.17: Instantaneous volume fraction of liquid at a cross-section in the Venturi throat

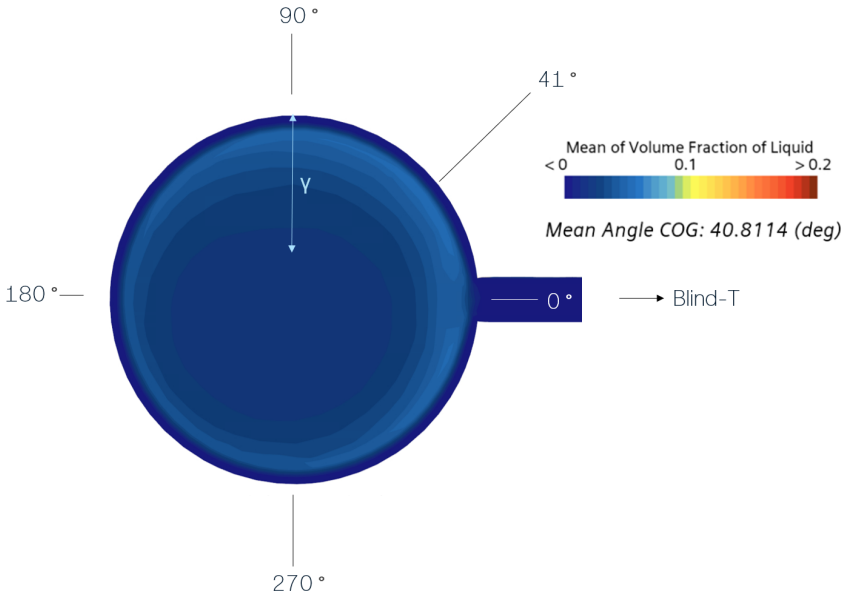

(a) Intermediate pressure test case

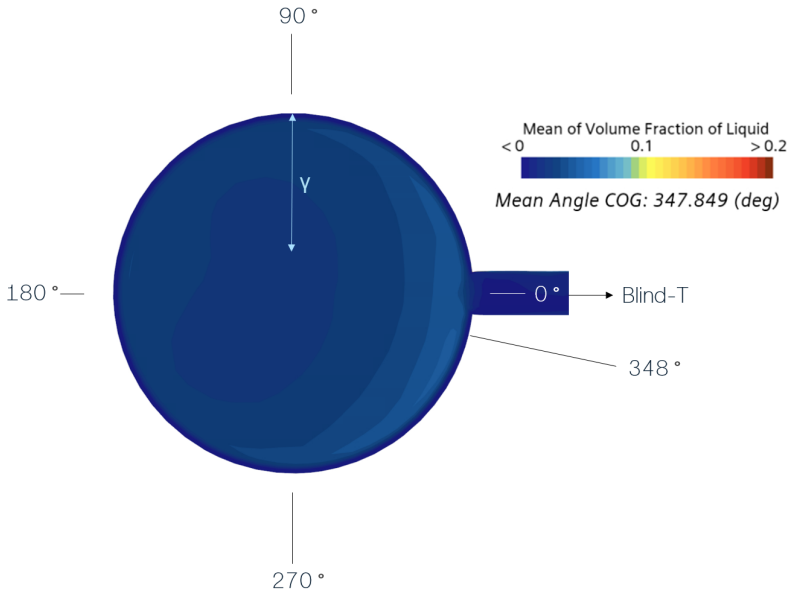

(b) High pressure test case

Figure 4.18: Liquid volume fraction mean of field, at a cross-section in the in Venturi throat

4.4.4 Liquid Viscosity Study

In Figures 4.19a and 4.19b, the liquid volume fraction mean of field is shown for the intermediate- and high viscosity cases respectively.

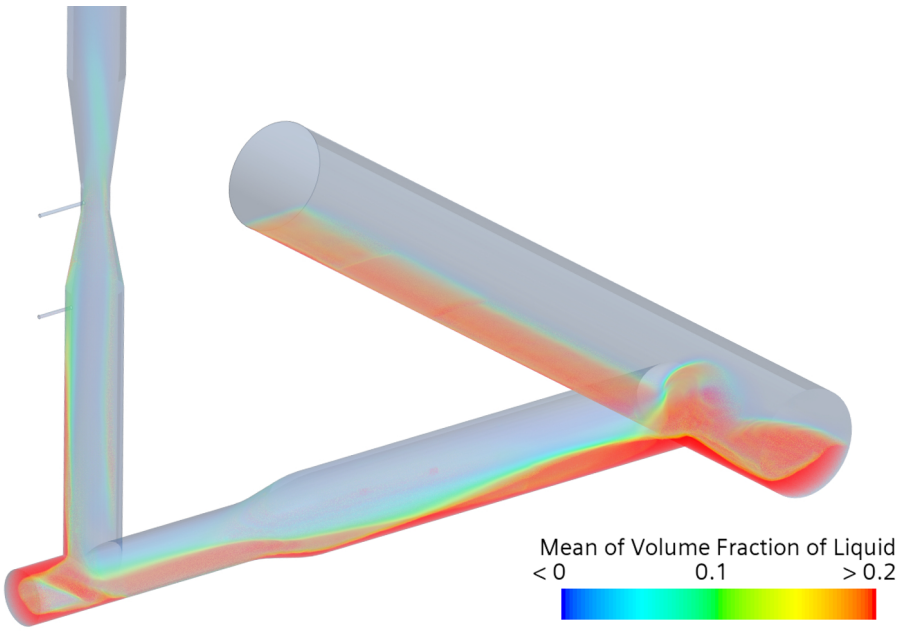

(a) Intermediate viscosity test case

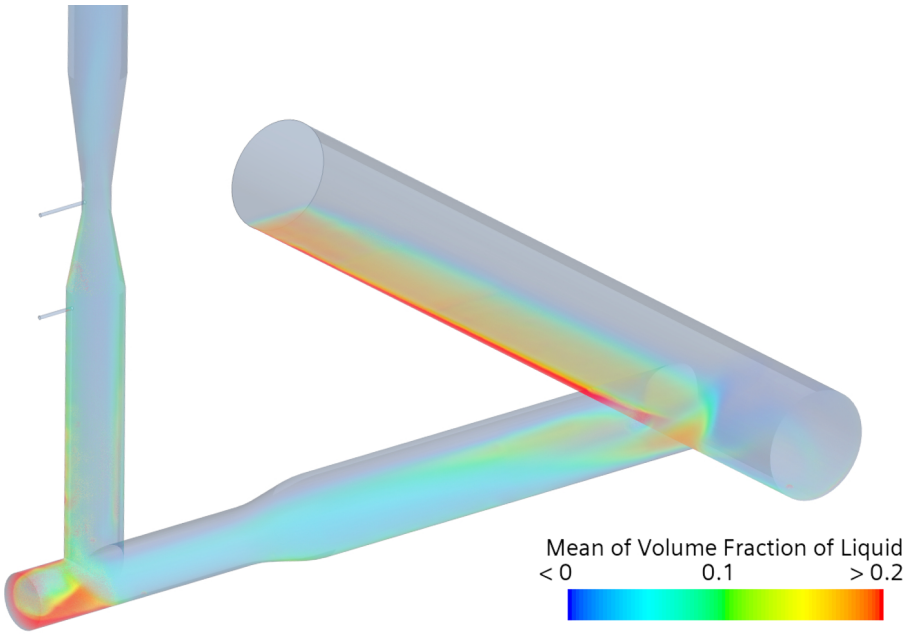

(b) High viscosity test case

Figure 4.19: Mean liquid volume fraction field, viscosity study

Comparing to the LVF mean of field for case A in Figure 4.6, the intermediate viscosity case behaves very similar with only minor difference blind-T liquid accumulation. However, comparing the high viscosity case to case A reveals significant

differences in mean flow behavior. With a high viscosity, there is substantially less liquid accumulation in both blind-T's but especially in the upstream blind-T. The liquid traveling up the VEL in the high-viscosity case is also more uniformly mixed and homogeneous compared to case A.

In Figure 4.20 the spectra of the GVF as measured in the entire Venturi throat is shown for the viscosity study. The * indicates the pressure that matches the viscosity in validation case A. In the spectra it can be observed, that as liquid viscosity increases, the amplitude of the oscillations decreases significantly. In the high-viscosity case, practically no oscillation in the GVF are observed. In the low- and intermediate-viscosity cases, the dominant frequency remains steady at approximately 0.75 Hz.

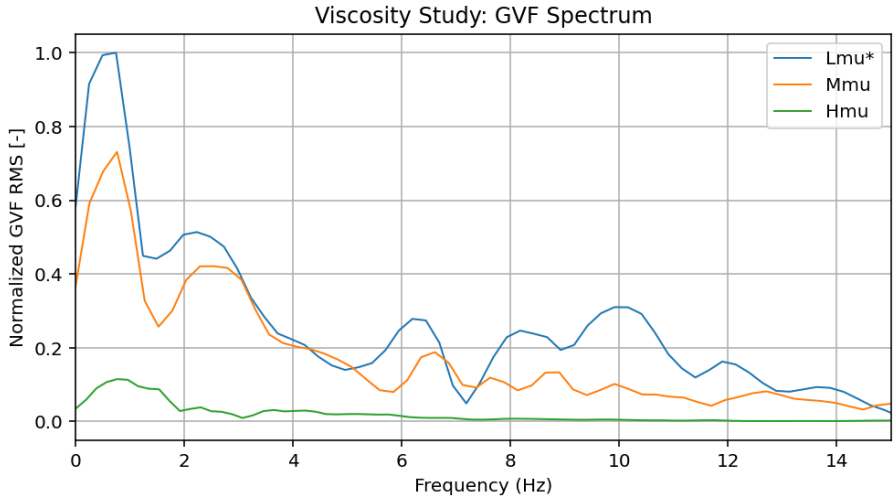

Figure 4.20: Spectra of GVF of fluid occupying Venturi throat, viscosity study

In Figures 4.21a and 4.21b the LVF field is plotted in a throat cross-section for the intermediate- and high viscosity cases respectively. The gamma-beam position is also visible in the figures. The intermediate viscosity case displays the presence of plugs, the location of which varies significantly with time. Overall the behavior is very similar to case A in Figure 4.9. The high-pressure case exhibits a much more homogeneous phase distribution in the throat, and no presence of plugs. The liquid distribution in the throat remains fairly constant over time, which coincides with the reduced amplitude in the oscillatory behavior observed in the GVF spectrum.

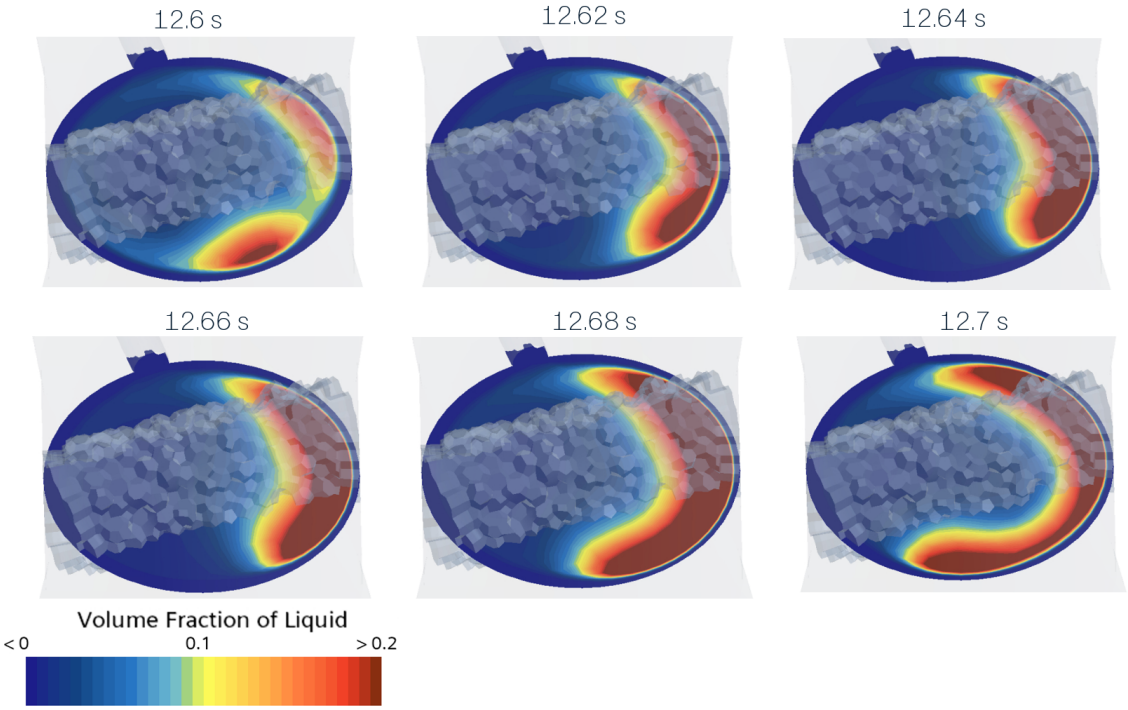

(a) Intermediate viscosity test case

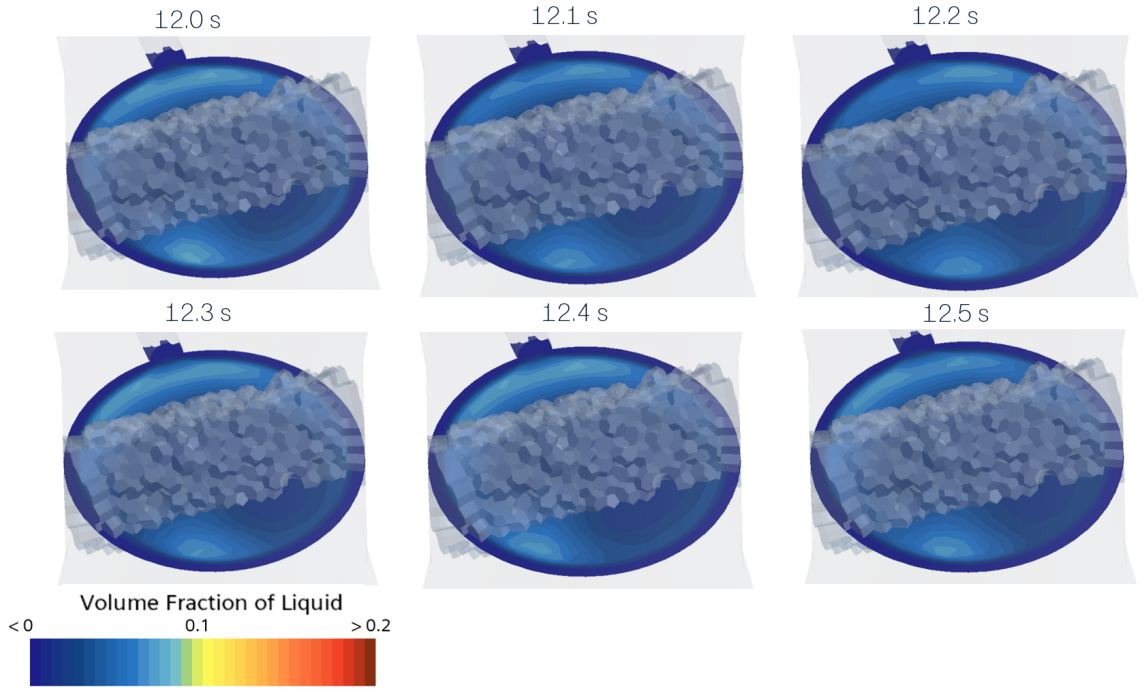

(b) High viscosity test case

Figure 4.21: Instantaneous liquid volume fraction field in Venturi throat cross-section, viscosity study

In Figures 4.22a and 4.22b the LVF mean of field is plotted in a throat cross-section for the intermediate- and high viscosity cases respectively. The direction of the average liquid center of gravity is indicated by the black arrow, and the direction

of the gamma-beam and the blind-T are also indicated in the figures. As can be observed, the high-viscosity case is significantly more homogeneous compared to the intermediate viscosity case. The mean of field for the high-pressure case is also very similar to the instantaneous LVF distributions shown in Figure 4.21b, indicating that the liquid distribution in the throat is very steady in nature. The mean radial location of the liquid centroid for the intermediate viscosity case is at 18.17% of the throat radius. Conversely, for the high viscosity case it is significantly closer at 7.81% of the radius, indicating a more uniform liquid distribution in the throat.

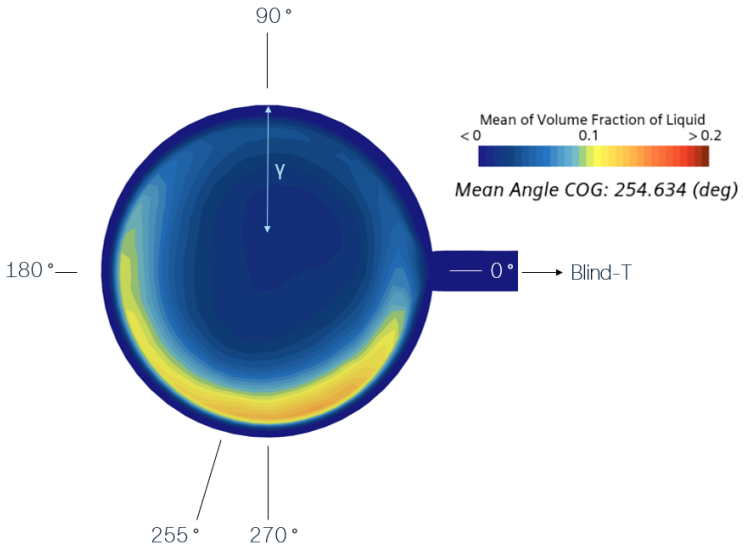

(a) Intermediate viscosity test case

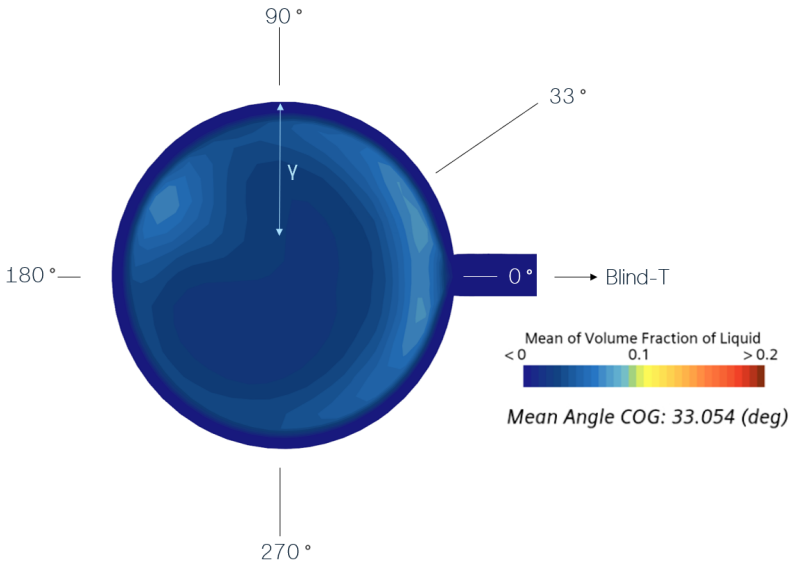

(b) High viscosity test case

Figure 4.22: Liquid volume fraction mean of field in Venturi throat cross-section, viscosity study

Table 4.5 presents the relative deviation between the measured volume-averaged

hold-up value in the gamma-beam and the true value in the whole throat section. As can be observed, the gamma-beam measures more accurately with an increased liquid viscosity. Additionally, the rotated gamma-beam accuracy is increased compared to the original orientation of the beam.

Table 4.5: Results Viscosity study

Case	Hold-up Gamma Beam	Hold-up Rotated Gamma Beam
1.7 cP	-1.20 %	-0.83 %
17 cP	-1.01 %	-0.75 %
117 cP	-0.57 %	0.03 %

4.5 Slip Study

The thesis conducted a slip-ratio study in order to evaluate if manipulation of design and flow parameters would affect the slip-ratio between the gas and liquid phases in the throat. As mentioned in section 3.6.3, three different slip-ratios were evaluated as summarized the list below;

- Dispersed liquid velocity against gas velocity
- Continuous liquid film against gas velocity
- Total liquid velocity (both film and dispersed) against total gas

When post processing the results, the computed slip-ratio was compared to the slip-ratio acquired from Case A. The results from this comparison is presented in Figure 4.23.

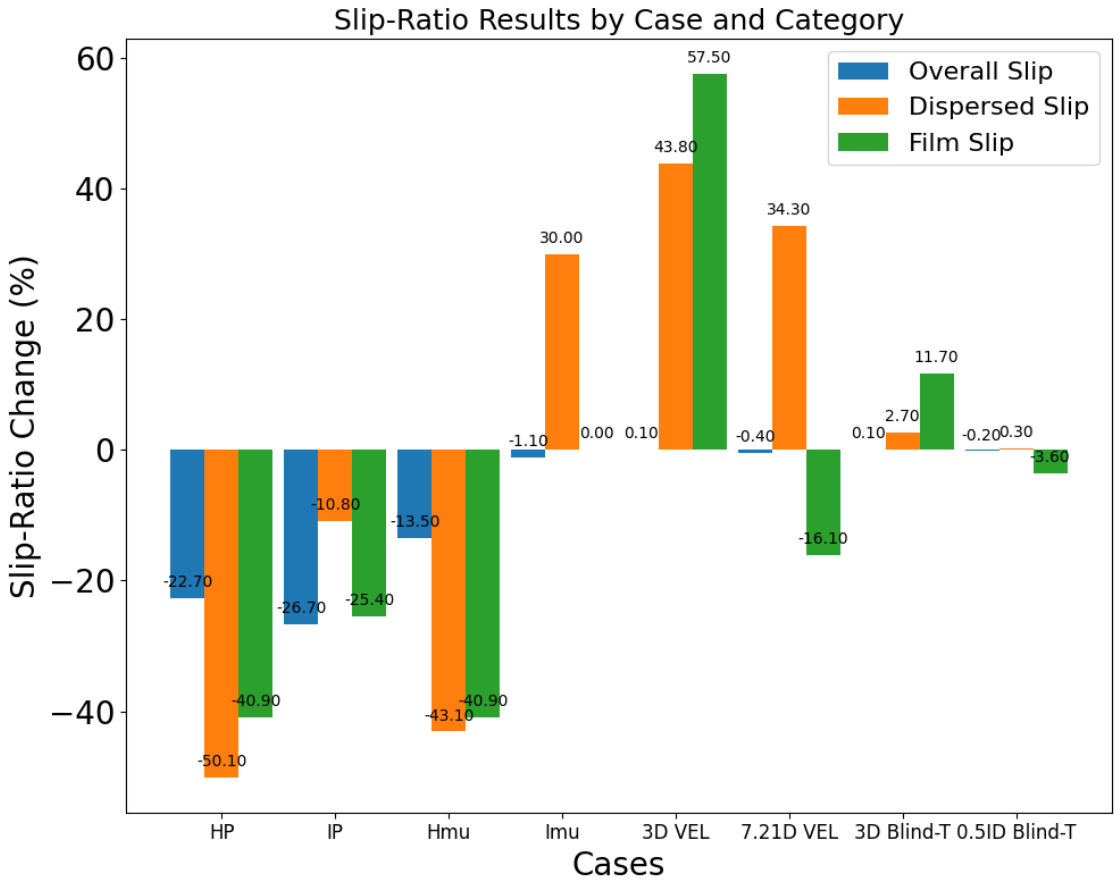

Figure 4.23: Histogram of the slip-ratio change.

As seen in the histogram plot, the high pressure (HP) and intermediate pressure (IP) cases display a decrease of slip-ratio, compared to the base case (Case A). In the viscosity study, the high viscosity (Hmu) case also shows a notable decrease in slip-ratio, whereas the intermediate viscosity (Imu) case remains close to the reference. For the geometrical design cases, the blind-T manipulations show the least deviation in slip-ratio, while the Vertical Entrance (VEL) cases generally display an increase in slip-ratio across the evaluated categories.

5
Discussion

In this chapter, the results gathered in this project are discussed, interpreted and analyzed. Additionally, any potential sources of error are elaborated in this chapter. Where relevant, suggestions for future work are proposed to further develop the understanding of the topic.

5.1 Simulation Method

In this section, the CFD model and the quality of the solution in regards to mesh, solver set-up and convergence is discussed and analyzed.

5.1.1 Mesh and Grid Independence

The mesh refinement and grid independence study shows that the solution generated was grid independent. The time-averaged mean values did not change significantly when different grid sizes were tested, and the FFT analysis did not show any significant deviations in signal behavior. Additionally, the mesh quality was thoroughly evaluated in terms of skewness angle, cell aspect ratio, face validity, and volume change, as presented in Appendix A. These evaluations showed that the mesh was of good quality. Thus, the mesh followed good practice and was more than sufficient for this study.

However, even though a coarser mesh (Mesh 1) was evaluated and considered good, it was decided to use the more refined mesh (Mesh 2). The decision to use Mesh 2 was based on previous work with mesh generation. While Mesh 1 was a coarse mesh that met this studies metrics for a good mesh, it might have failed to capture critical flow features such as vortices and turbulent structures accurately. Additionally, the coarser mesh could cause numerical issues and instability in regions with high gradients. Since the study aimed to evaluate different flow conditions that might enhance gradients, it was concluded that the coarser mesh might not be suitable. The final argument in favor of using Mesh 2 was that the CPU time was significantly lower compared to Mesh 3 and not much higher than that of Mesh 1.

From the slip-ratio study, it can be concluded that the boundary layer mesh may be insufficient. Experimental studies in the test loop have shown that there is always a liquid film present in the throat, whereas from the simulations the liquid film is only present occasionally. This might be due to a too coarse resolution of the wall

boundaries, which ultimately loses important information about the continuous liquid film. However, it might also be due to the definition of a liquid film in this report, which will be further discussed in section 5.5.

5.1.2 Solver set-up

The solver setup was mainly evaluated based on the results from the validation study and convergence. Table 4.2.1 presents the percentage difference between the experimental results from the test loop and the computed mean values from the CFD simulation. Based on these results, it is clear that the solver setup is suitable, as it computes very similar values. The only value with a significant deviation is the pressure drop Δp, even though the pressure measured from the CFD manometers align very well with the experimental values. This deviation is due to the pressure drop being a small compared to the manometer readings, so even a slight deviation in manometer pressure causes a significant percentage difference. Pressure calculations depend on the solver settings, mesh, and computational domain. Thus, another reason for the deviation might be the use of a pressure outlet as a boundary condition. The boundary was set to 0 Pa, meaning the reference pressure was supposed to be the outlet pressure. If the boundary is too close to the domain of interest, this might lead to the solution being forced to adapt according to the set target output, thus impacting the pressure computations. Additionally, the choice of turbulence models might be the cause of the deviation. There was no time to evaluate the sensitivity to other turbulence models, so this theory cannot be investigated further in this study.

5.1.3 Convergence

The convergence criteria used in the project followed the set target limitations, with no significant fluctuations and low residual values after each time step. In Figure 4.4, the cumulative error in mass for both phases is presented. The total loss of liquid in relation to the total mass of liquid that has passed through the system is 0.21%, which is quite low. The gas shows an increase in mass compared to the total mass of gas passed through the system of 0.0056%, which is very low. Furthermore, in Figure 4.3, it can be seen that per timestep, the mass error is very close to zero, which further explains the low mass errors. Both of these mass errors are not significant, and the continuity can be considered satisfied.

5.2 Sensitivity Study of MPFM accuracy

The results of this project indicate that the geometry of the piping upstream of the MPFM has minimal impact on the homogeneity of the fluid in the throat. Consequently, the piping geometry is observed to have only a minor influence on measurement accuracy, as can be observed in Tables 4.2 and 4.3 However, an influence on the oscillatory behavior is observed in both the blind-T and VEL studies, as illustrated in Figures 4.12 and 4.14.

Evaluating the MPFM sensitivity to flow properties such as pressure and viscosity reveals that these factors have a more significant impact than piping geometry, both on measurement accuracy and on oscillatory behaviors. Increased pressure reduces the surface tension between gas and liquid and makes their densities more similar, facilitating better mixing and increased homogeneity. At low pressure, as seen in validation case A in Figure 4.6, minimal mixing occurs in both blind-T's. In contrast, high pressure results in significant mixing already at the upstream blind-T, as can be observed in Figure 4.15b. Therefore, increased pressure positively affects mixing and flow homogeneity, thereby increasing MPFM accuracy.

Based on the results gathered in this study, an increase in viscosity also facilitates better mixing in the blind-T's and a more homogeneous distribution between the phases. Intuitively, the trend should be the opposite, that a decrease in viscosity facilitates better flow mixing and uniformity. A lower viscosity liquid is less resistant to shear- and turbulent forces which would promote mixing. When completing the sensitivity study in this project, only the viscosity was varied, and no other flow properties were changed. For example, surface tension remained constant throughout the sensitivity study. However, this does not necessarily capture characteristics of real liquids in the pipe, because typically when viscosity varies other properties vary with it. Therefore the study completed is limited to the sensitivity of viscosity only, but doesn't really capture the flow characteristics when using 'real' liquids. This may also explain the counterintuitive trends indicated by the results of the viscosity study. Another probable explanation for these results is the choice of multiphase topology modeling. The topology selected for this study was continuous-dispersed, which means that the liquid is always dispersed in the domain as droplets. Since the liquid is dispersed as droplets, the Eulerian approach cannot fully interpret the liquid viscosity as such, since the model does not 'see' individual droplets with internal liquid viscosity.

In this thesis, the gamma-meters placement was evaluated to compare the measured hold-up in control volumes corresponding to the gamma-beams and the actual GVF in the throat at the same time. It is important to be aware that these two quantities are not strictly equivalent. However, to be able to recreate the actual gamma-meter, which measures hold-up, this approach was necessary. The comparison done still provides valuable insight into the gamma-meters representativeness and their ability to evaluate the flow characteristics. The results show that the there is a small relative deviation between the measured hold-up and present GVF in the throat indicating the gamma-beam captures the flow conditions well. However, there are tendencies that show that the rotated gamma-meter measures more accurately for all studies except the VEL study, indicating that changing the gamma-meter placement may be favorable.

In this study, it is observed that the MPFM is sensitive to the flow regime present in the flow. The main observable flow regimes in this study are plug- and annular flows. In test-cases where the MPFM accuracy is improved and oscillations reduced,

it is observed that the flow regime has changed from plug to annular. These results indicate that it is not necessarily the changes in operating conditions or geometry that improve MPFM performance, but rather the change in flow regime.

5.3 Oscillatory flow behavior

In this section the oscillatory behavior of the flow in the CFD domain and experimental test-loop are discussed. The sampling frequency and measurement time, and their influence on the results gathered in this project are discussed. Additionally, potential sources of the oscillations are discussed for both the test-loop and the CFD simulations.

5.3.1 Sampling frequency and measurement time

In the test loop, the pressure sampling frequency is 1 Hz, allowing frequencies below 0.5 Hz to be observable. The GVF is sampled at 45 Hz, making the highest observable frequency 22 Hz. With a measurement time of 30 minutes, low-frequency oscillations can be resolved and are visible in the spectrum.

In contrast, the CFD sampling frequency is 10 kHz with a measurement time of approximately 5-12 seconds. Due to the computational expense, extending the measurement time to capture low-frequency oscillations is challenging. Consequently, low-frequency oscillations cannot be resolved, but high-frequency oscillations are visible. This discrepancy makes it difficult to compare the test-loop flow behavior to the CFD simulations, as the observable frequencies differ. While CFD simulations provide valuable insights into high-frequency oscillations, resolving the low-frequency behavior observed in the test loop remains difficult. Therefore, matching periodic phenomena in the CFD domain to low-frequency oscillatory behaviors in the physical test loop is also challenging.

5.3.2 Sources of oscillatory behaviors

There are two main sources for oscillatory behaviors in the flow; the blind-T and the outlet piping. In the blind-T's the mixture circulates in stationary vortices. Liquid accumulates in the blind-T's, which then sheds with the vortices into plugs. These plugs are visible as oscillations in the measured GVF. The other possible source of oscillatory behavior is the outlet piping straight leading to the separator. Based on findings from the experimental test-loop, it is believed that this can cause low frequency oscillations in the pressure which also may manifest in the GVF measurements. Other possible sources are flow induced vibration in the piping.

Experimental test-loop

The experimental data measured in the test-loop exhibits periodic and oscillatory behaviors, with clear peaks above the background noise level as can be seen in Figure 4.2. The source of these oscillations is likely the outlet piping section leading

to the separator. The other possible source is the blind-T's, although it is believed that they would generate higher frequency oscillations than those observed. The dominant frequency peaks for the measured GVF shown in Figure 4.2 may be due to the plug shedding in the blind-T although this is not possible to confirm.

CFD simulations

The main observable source of oscillatory behavior in the GVF signal in the CFD simulations is the plug shedding in both the upstream and downstream blind-T's. This is also supported by the observation that all tests where the flow is practically homogeneous, such as the high-pressure and high-viscosity tests, have a substantial decrease in oscillatory behavior. This can be observed in figures 4.16 and 4.20.
The nature of the plug shedding depends on the flow regime, fluid characteristics, and geometry. However, the frequency of plug shedding is independent of these factors. The constant frequency observed in all test cases is likely connected to the liquid accumulation rate in the blind-T's, where a deeper blind-T should allow more liquid accumulation and lower frequency oscillations. Since the downstream blind-T sensitivity study showed no significant change in frequency between the tested cases, it is believed that the upstream blind-T significantly impacts the plug shedding process and the observed GVF oscillations. This, in turn, influences the mixing and homogeneity of the flow, and consequently, the MPFM accuracy. The variation in amplitude observed in GVF spectra is thought to be related to the level of mixing achieved in both blind-T's, as well as the location of the recirculation zone in relation to the bulk flow. The influence of the upstream blind-T has not been studied in further detail in this project, and it is suggested that this should be studied further.

It cannot be excluded that the outlet piping contributes to flow oscillations in the CFD model, similar to the physical test loop where the outlet piping is thought to cause oscillations in the flow. In the CFD fluid domain used in this project, the outlet pipe length was selected to sufficiently avoid interference with the solution in the volume of interest, the Venturi throat. However, to increase the chances of capturing realistic oscillations caused by the outlet piping, an even longer outlet could be used. The shorter outlet used in this project risks suppressing oscillations such as those observed in the physical test loop. The effect of outlet piping on the oscillatory behaviors of the flow is therefore suggested to be studied further.

5.4 Slip

From the results presented in Figure 4.23 some reflections can be made. From the pressure and viscosity study it can be seen that the relative velocity between the phases is the most influenced by manipulation of flow parameters. The pressure study, displays the most substantial negative change of all simulations. This is most likely an indication of the increased drag between the phases, which increases with higher pressure, since the density of the gas increases. As a result, an increased drag force acts to equalize the velocities, thereby reducing the slip-ratio. Additionally,

the higher pressure cases shows a more homogeneous flow which also contributes to the decrease in slip. The slip decreases with higher viscosity as well, however, these results were not as expected. The reason for this is further explained in section 5.5. Viscous fluids tend to resist deformation and shear better than low viscosity fluids, which should instead increase the slip.

The design cases yield a more varied outcome in the slip-ratio study. The blind-T study shows much smaller deviation from the base case compared to the other studies, especially the 0.5ID Blind-T case. This suggests that the impact from a changed blind-T depth is limited. In contrast, the change in vertical entrance length shows a general increase in slip-ratio, especially for the dispersed slip. The shortest VEL shows that all investigated slip-ratios increase. This could be explained by slowly moving liquid plugs from the blind-T being present at the throat. In contrast, for the increased VEL only the dispersed slip increases, whereas the film slip decreases. This was not expected since increased VEL most likely would increase the gravitational effect on the flow, slowing both liquid film and dispersed film down resulting in higher slip.

5.5 Sources of Error

In this section, any possible sources of error that may influence the results gathered in this study are elaborated.

5.5.1 Mean fields

In order to ensure that any mean computed is accurate and representative of the flow in the domain, sufficient simulation time for the averaging is required. This is applicable for the mean of fields in the entire domain, but especially of the mean of liquid volume fraction fields in the Venturi throat. Even with a long sampling time, gradual changes in the flow regime and liquid distribution risk not being captured in the sampling time, and may therefore not be represented in the mean of field. In other words, there is a risk that the mean of field captured is a temporary mean, and not the true mean of field. The risk of this occurring can be minimized by monitoring how the mean of field develops, and only extracting the mean of field once it has stabilized in time.

5.5.2 Liquid Viscosity

The results from the viscosity study show trends that are different than expected and difficult to explain. There may be many factors that influence the results obtained, both physical and numerical. Firstly, only the viscosity of the liquid was changed without addressing any other flow properties associated with real liquids. Therefore, the results gathered in the viscosity study are not suitable for evaluating and predicting the behavior in real life situations. In addition, there are several numerical and simulation-specific factors that also could influence the validity of

the results. For example, the simulation may be sensitive to interfacial dynamics that might not be adequately resolved in the simulations completed for this study.

5.6 Further Work

In this section, suggestions on further work are elaborated. The suggestions are based on findings in this study.

5.6.1 Liquid Viscosity

Further research is suggested to evaluate the effect of liquid viscosity on flow characteristics and mixing in MPFM applications. It is valuable to further develop an understanding of the physical phenomena and flow characteristics, particularly regarding mixing and interphase interactions between gas and liquids of varying viscosity. Additionally, it is valuable to further understand simulation- and modeling specific sensitivities when evaluating such flows.

5.6.2 Outlet piping

In the MPFM experimental test-section it is observed that the outlet piping may influence the oscillatory behavior of the flow in the Venturi throat. However, when completing the CFD simulations for the purpose of this study, the outlet piping is not sufficiently long to capture these types of oscillations, if they are present. Therefore, it is suggested to further study the MPFM sensitivity to outlet piping in regards to oscillatory behavior. It is also valuable to develop a CFD-modeling method that captures these types of oscillations.

5.6.3 Upstream blind-T

In this study, the MPFM sensitivity to the depth of the downstream blind-T was evaluated, and no significant sensitivity was observed. However, there were indications that the MPFM may be sensitive to the upstream blind-T, particularly in plug flow conditions. Therefore, it is recommended that the flow characteristics be further investigated in scenarios where multiple blind-T's are present in the piping system.

5.6.4 Turbulence models

This study has only evaluated one type of turbulence model. For further studies, evaluating how for instance the k-ϵ model would model the flow would be interesting since it might capture the liquid film behavior better and correct the pressure deviations observed in the validation study.

5.6.5 Continuous liquid

The study has showed that the accumulation of liquid in the blind-T's is significant. Therefore, the liquid might be more accurately described as a continuous phase at these locations. Since this study has assumed that the liquid always can be treated as dispersed phase this might impact the solution. Thus, for further studies, applying the multiple topology should be tested in order to see if it will have a significant impact on the liquid behavior.

6
Conclusion

In this chapter, conclusions are drawn based on the results and discussions in this project. Conclusions are drawn both in terms of the simulation technique, and the sensitivity study of the MPFM.

6.1 Summary

In this study, flow in and around an MPFM has been simulated in CFD using the EMP modeling approach. A suitable modeling technique has been developed, that has a good balance between accuracy and computational expense. This study has investigated and analyzed MPFM sensitivity to geometrical parameters and operating conditions in terms of precision and accuracy. Additionally, the slip between the phases has been investigated as well as oscillations and fluctuations in the flow.

6.2 Simulation Method

In summary, the quality of the simulation in terms of mesh, solver setup, convergence, and computational time is satisfactory. The mesh study shows that the mesh is suitable, with some concerns regarding the boundary layer mesher. Convergence is achieved for all simulations, and stability is observed in all cases. The solver setup generates accurate solutions compared to test data, all while maintaining reasonably low CPU time.

6.3 Sensitivity Study

In this study geometry changes in terms of vertical entrance length, and blind-T depth have been studied. Based on the results, it can be concluded that the upstream pipe geometry changes studied in this project do not significantly influence the MPFM measurement accuracy. Additionally, no significant changes in mixing and flow homogeneity are recorded. However, geometry has a moderate impact on the oscillatory behavior of the flow. The blind-T's significantly affect the nature of plug shedding, and the presence of upstream blind-T's also impact the flow regime. Plugs in the flow may manifest as oscillations in the detected GVF. At low pressures and liquid viscosity where mixing in in the blind-T's is minimal, the presence of any upstream blind-T's may significantly impact plug shedding characteristics. At high pressure and viscosity however, the mixing is greatly improved. In this case, the

presence of upstream blind-T's may instead improve homogeneity of the flow significantly.

The MPFM sensitivity to vertical entrance length is concluded to be minimal based on the results gathered in this study. No visible trend can be observed in the MPFM accuracy with varying VEL, but minor variations in oscillatory amplitude are observed.

The greatest sensitivity of the MPFM is concluded to be the flow regime. This is in turn influenced by flow properties and operating conditions as observed in this study, where the sensitivity to pressure and liquid viscosity was examined. An increase in pressure facilitates improved mixing, and together with the presence of blind-T's, the flow in the MPFM is homogenized. The accuracy of the MPFM increases with higher pressure, and oscillations recorded in the flow are reduced due to the absence of plugs in the flow. The same trends and characteristics were also observed when liquid viscosity was increased, although these results are counterintuitive and should be considered with some reservations. However, it can definitely be concluded that the MPFM accuracy is sensitive to liquid viscosity, and that this needs to be accounted for in the interpretation models used by the MPFM.

From the investigation of the slip-ratio some conclusions can be drawn. The manipulation of fluid parameters seems to impact the slip-ratio more significantly compared to geometry changes. However, it is hard to pin point what causes the flow to be more sensitive to changing flow parameters, especially in regards to changed viscosity which most likely is impaired by the set-up of the viscosity study simulations.

Bibliography

[1] S. Corneliussen et. al, *Handbook of multiphase flow metering*, Produced for The Norwegian Society for Oil and Gas Measurement and The Norwegian Society of Chartered Technical and Scientific Professional, 2005. [Online]. Available: https://nfogm.no/wp-content/uploads/2014/02/MPFM_Handbook_Revision2_2005_ISBN-82-91341-89-3.pdf.

[2] ABB, *Multiphase flow meters faq*, Last accessed 29 Jan 2025. [Online]. Available: https://library.e.abb.com/public/1860ce14370dc1aa85257d4f00495df1/FAQ_VIS_Final%20.pdf.

[3] M. Zhan, M. A. B. Razali, A. Moitra, C.-G. Xie, W. L. Loh, and J.-J. Shu, "Influence of design parameters of upstream venturi pipeline on multiphase flow measurement", *Engineering Applications of Computational Fluid Mechanics*, vol. 17, no. 1, 2023.

[4] I. Tyssen, *6 operational benefits of multiphase flow meters in unconventional oil production*, Last accessed 29 Jan 2025. [Online]. Available: https://www.emersonautomationexperts.com/2020/measurement-instrumentation/flow/6-operational-benefits-of-multiphase-flow-meters-in-unconventional-oil-production/?utm_source=chatgpt.com.

[5] B.T.Hjertaker, S.-A. Tjugum, A. Hallanger, and R. Maad, "Characterization of multiphase flow blind-t mixing using high speed gamma-ray tomometry", *Flow Measurment and Instrumentation*, vol. 62, no. 1, 2018.

[6] A. Kantzas, J. Bryan, and S. Taheri, *Surface and interfacial surface tension.* [Online]. Available: https://perminc.com/resources/fundamentals-of-fluid-flow-in-porous-media/chapter-2-the-porous-medium/multi-phase-saturated-rock-properties/surface-interfacial-tension/#:~:text=Saturated%20Rock%20Properties%3A-,Surface%20and%20Interfacial%20Surface%20Tension,forces%20acting%20on%20the%20interface., (accessed: 24.04.2025).

[7] S. Sasic, *Coarse in multiphase flows, lectures from course tme160 multiphase flow*, 2024.

[8] Schlumberger, *Fundamentals of Multiphase Metering* (International series of monographs on physics). SLB, 2012, ISBN: 978-1-937949-02-0.

[9] P. Daniel R. McAlister, *Gamma ray attenuation properties of common shielding materials*, 2018. [Online]. Available: https://www.eichrom.com/wp-content/uploads/2018/02/Gamma-Ray-Attenuation-White-Paper-by-D-M-rev-6-1-002.pdf.

[10] Idealsimualtions, *Cfd mesh guide*, Last accessed 24 Jan 2025. [Online]. Available: https://www.idealsimulations.com/guides/cfd-mesh-guide/.

[11] B. Andersson, R. Andersson, L. Håkansson, M. Mortensen, R. Sudiyo, and B. van Wachem, *Computational Fluid Dynamics for Engineers*. Cambridge University Press, 2011.

[12] Siemens, *What is boundary skewness angle*, Last accessed 29 April 2025. [Online]. Available: file:///soft/bin/starccm/19.06.008/STAR-CCM+19.06.008-R8/doc/en/online/STARCCMP/GUID-4320B690-0437-412B-A229-C6C9D8DD1F2E.html.

[13] Siemens, *Mesh quality*, Last accessed 29 April 2025. [Online]. Available: file:///soft/bin/starccm/19.06.008/STAR-CCM+19.06.008-R8/doc/en/online/STARCCMP/GUID-FAB6B0AA-44A6-4A7B-AA27-A2EC92918B8F.html#GUID-FAB6B0AA-44A6-4A7B-AA27-A2EC92918B8F__GUID-94999BCC-DE30-4A7B-B9EF-F715E395AD19.

[14] W. Malalasekera and H. K. Versteeg, *An Introduction to Computational Fluid Dynamics: the Finite Volume Method*. Pearson Prentice Hall.

[15] A. Bakker, *Applied computational fluid dynamics*, 2002. [Online]. Available: http://www.lcad.icmc.usp.br/~buscaglia/teaching/mfcpos2013/bakker_06-bound.pdf.

[16] L. Davidson, *An Introduction to Turbulence Models*. Department of Thermo and Fluid Dynamics at Chalmers University of Technology, 2022. [Online]. Available: https://www.tfd.chalmers.se/~lada/postscript_files/kompendium_turb.pdf.

[17] L. Davidsson, *Fluid mechanics, Turbulent flow and Turbulence modeling*. Division of Fluid Dynamics, Department of Mechanics and Maritime Sciences, Chalmers University of Technology, 2024.

[18] Siemens, *Simcenter star-ccm+ user guide, multiphase flows*, Last accessed 24 May 2025. [Online]. Available: https://docs.sw.siemens.com/documentation/external/PL20230406746979366/en-US/userManual/starccmp_userguide_html/STARCCMP/GUID-40F39626-68FC-4928-9695-77394F6B83D8.html.

[19] Siemens, *Phase interaction topology*, Last accessed 25 April 2025. [Online]. Available: file:///soft/bin/starccm/19.06.008/STAR-CCM+19.06.008-R8/doc/en/online/STARCCMP/GUID-0FCEC362-077D-45CE-BFF8-39C17ACC42DD.html.

[20] S. Brunton and J. N. Kutz, *Data driven science and engineering, machine learning, dynamical systems and control*. [Online]. Available: https://databookuw.com, (accessed: 14.04.2025).

[21] Phonical, *View of a signal in the time and frequency domain*. [Online]. Available: https://commons.wikimedia.org/wiki/File:FFT-Time-Frequency-View.png#metadata, (accessed: 14.04.2025).

[22] M. Viswanathan, "Interpret FFT results – obtaining magnitude and phase information", *GaussianWaves - Signal Processing for Communication Systems*, 2015. [Online]. Available: https://www.gaussianwaves.com/2015/11/interpreting-fft-results-obtaining-magnitude-and-phase-information/.

[23] Dynamox, *The peak, peak to peak and rms values in vibration analysis*. [Online]. Available: https://dynamox.net/en/blog/the-peak-peak-to-peak-and-rms-values-in-vibration-analysis.

[24] National Instruments, "Understanding FFTs and Windowing", [Online]. Available: https://download.ni.com/evaluation/pxi/Understanding%20FFTs%20and%20Windowing.pdf, (accessed: 16.04.2025).

[25] S. W. Smith, *The scientist and engineer's guide to digital signal processing*. [Online]. Available: https://www.dspguide.com/ch9/1.htm, (accessed: 16.04.2025).

[26] Scipy, *Scipy.signal.welch documentation*. [Online]. Available: https://docs.scipy.org/doc/scipy/reference/generated/scipy.signal.welch.html, (accessed: 17.04.2025).

[27] M. X. Cohen, *Welch's method for smooth spectral decomposition*. [Online]. Available: https://www.youtube.com/watch?v=YK1F0-3VvQI, (accessed: 17.04.2025).

[28] M. Perić, *Polyhedral grids in star-ccm+*, Last accessed 4 Mar 2025. [Online]. Available: https://support.sw.siemens.com/en-US/knowledge-base/KB000033548_EN_US.

[29] Siemens, *Simcenter star-ccm+ user guide*, Last accessed 4 Mar 2025. [Online]. Available: https://docs.sw.siemens.com/en-US/doc/226870983/PL20220717079233442.starccmp_userguide_html/3b6dfe55-f51c-4828-a593-d23f55646711.

A

Appendix A

A.1 Mesh refinement Study

A mesh refinement study is completed as a step in validating a CFD simulation set-up. The purpose is to verify that the solution is not sensitive to the selection of mesh, and to investigate if the mesh can be made coarser and thus save CPU time. In this section, the mesh refinement study that informed the mesh selection in section 3.3.4 is elaborated.

A.1.1 Method

The study consisted of evaluating three different meshes in terms of total cell count. The mesh in the manometers was not included in the study as the mesh could not be further coarsened in these areas. From the experimental data there were 3 different validation cases, A ,B and C that were used. Each one of them had different mixture velocities in the throat. To generate a mesh which would be suitable for all different cases the highest velocity case, case C was used as the base case for the mesh refinement study. To evaluate the mesh quality, the parameters compared were those measured by the actual MPFM, specifically pressure, phase velocities and hold-up derived from the gamma-system measurements. If the time-averaged mean values remain consistent across different mesh configurations, the solution can be considered grid-independent. In such a case, coarsening the mesh may be justified to reduce computational cost without compromising accuracy.

Table A.1: Meshes evaluated in mesh refinement study

Mesh	Base Size (mm)	Cell Count	CPU Time 1 Sec (h)
Mesh 1	13.5	320 015	5.49
Mesh 2	9.0	549 207	6.54
Mesh 3	6.0	1 194 287	11.64

Mean Values

With the aim to evaluate if different meshes were going to generate the same solution, time-averaged mean values were used. Surface average reports were used to determine the pressure in the manometers and the phase velocities in the throat. A volume average report was used to evaluate the hold-up in the gamma beam control volume. Once the simulation was considered to have reached a steady state, the calculation of time-averaged mean values was initiated. The simulation was then allowed to continue for several additional simulation seconds to ensure that reliable time-averaged values could be obtained.

Spectral analysis

In order to ensure that the oscillatory behavior of the flow is grid independent, a spectral analysis is completed for selected flow quantities extracted from the CFD simulation. From all 3 tested meshes, selected flow quantities are compared using spectral analysis, the method for obtaining the spectra is described in section 3.6.4.

The selected flow quantities can now be compared in the spectrum, to find any differences or similarities in oscillatory behaviors. This aids in determining the mesh influence on oscillatory behavior, and in finding a suitable mesh for the continued simulations.

A.1.2 Results

In this section, the results from the mesh refinement study are shown, both in terms of mean values as well as the overall behavior and fluctuations of the flow.

Mean Values

The results from the computed time-averaged mean values are showed in Table A.2. The corresponding difference in percentage between calculated values for each mesh is presented in Table A.3.

Table A.2: Time-Averaged Mean Values

Mesh	P1 [bar]	P2 [bar]	Hold-Up [%]	Hold-Up 90 [%]	Gas Velocity	Liquid Velocity
Mesh 1	29.32	26.06	95.5	95.78	111.04	79.82
Mesh 2	29.28	26.03	95.41	95.54	111.18	80.4
Mesh 3	29.24	26.06	95.7	95.7	110.83	81.11

Table A.3: Percentage difference in computed values between meshes

Quantity	Mesh 1 on Mesh 2	Mesh 1 on Mesh 3	Mesh 2 on Mesh 3
P1	0.13%	0.13%	0.27%
P2	0.11%	0%	0.11%
Hold-Up	0.09%	0.21%	0.30%
Hold-Up 90	0.25%	0.08%	0.17%
Gas Velocity	0.13%	0.19%	0.32%
Liquid Velocity	0.72%	1.59%	0.88%

Based on the results from the mesh refinement study, it can be concluded that the solution is grid-independent, as the computed values remain nearly identical across different mesh configurations. The difference between the meshes are minimal for all evaluated parameters. However, the liquid velocity shows the largest deviation when comparing Mesh 3 to Mesh 1. Despite this, the mean values suggest that Mesh 2 offers the best balance between accuracy and computational efficiency, making it the most suitable choice for this study. Although the differences between Mesh 1 and Mesh 3 are insignificant, Mesh 1 is notably coarse. Based on prior experience and established practices in CFD, such a coarse mesh could potentially lead to numerical instability or divergence under different operating conditions, even if it appears sufficient for the tested conditions.

Spectral Analysis

As shown in Figures A.1a and A.1b, the dominant frequency is approximately 1.7 Hz for all three meshes in both pressure and GVF, with slight variations in RMS magnitude. There is no clear trend in RMS magnitude between the meshes, and given the minor differences, these variations may be attributed to noise in the simulation data or inaccuracies in the magnitude approximation using the Welch method. Therefore, it can be concluded that the choice of mesh does not significantly affect signal fluctuations

A.1.3 Conclusion

Based on the results from the mesh refinement study, it can be concluded that the solution is grid independent. The selected mesh for the continued simulations is mesh 2 in Table A.1.

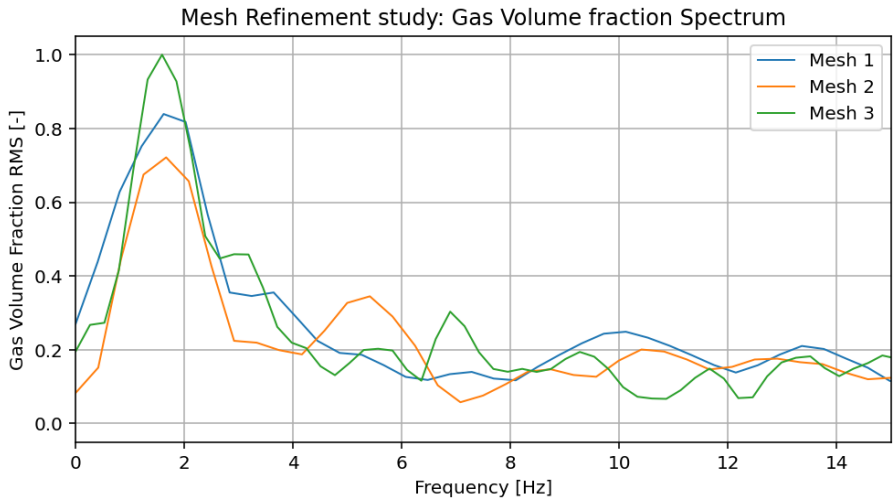

(a) GVF of fluid occupying Venturi throat

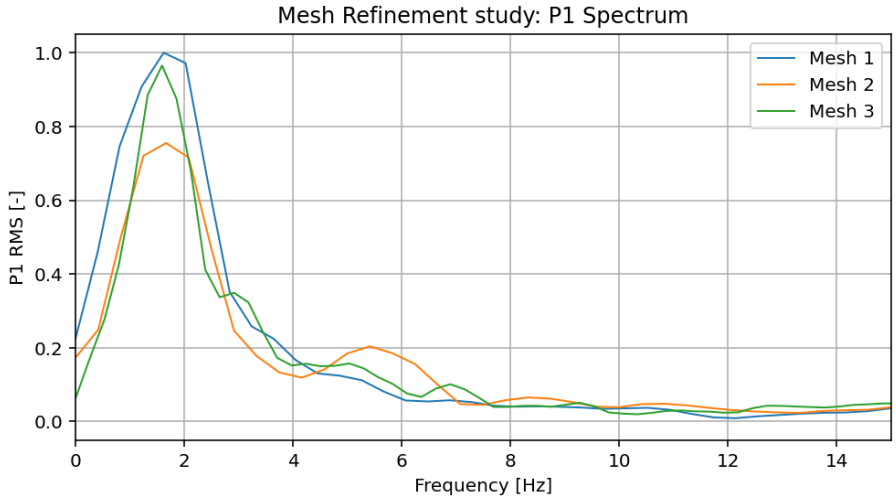

(b) p_1

Figure A.1: Frequency spectra for 3 tested meshes in mesh refinement study

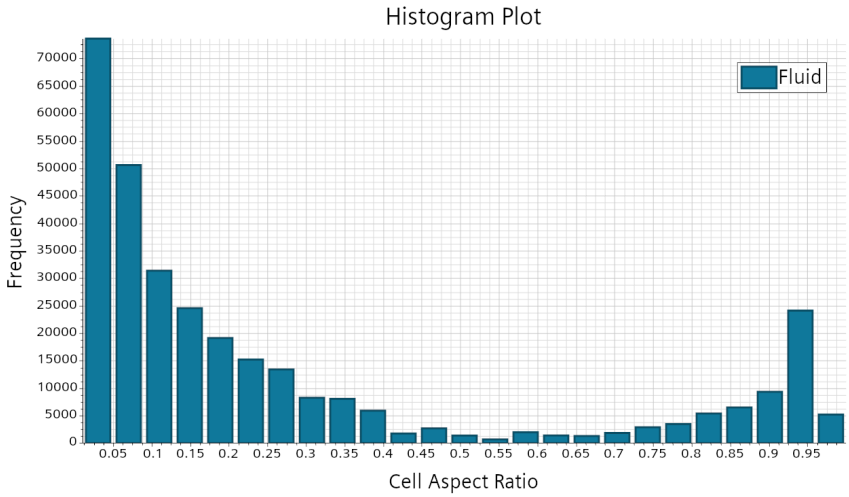

(a) Cell aspect ratio and frequency of cells

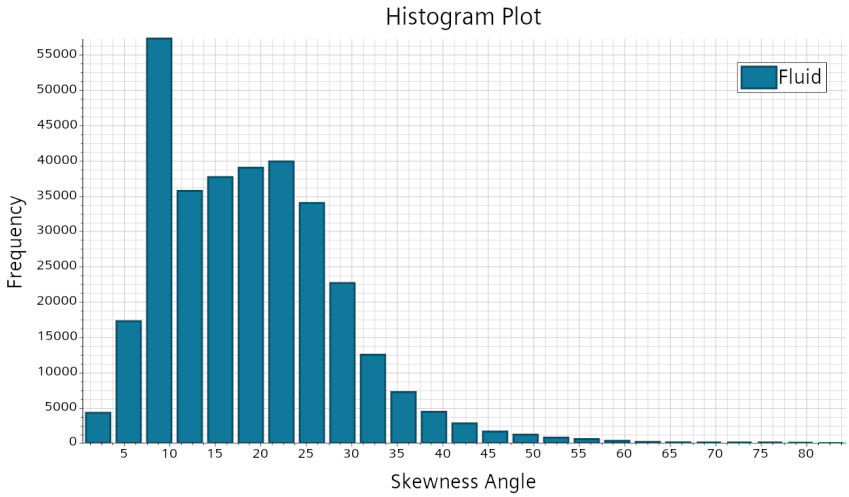

(b) Skewness angle and frequency of cells

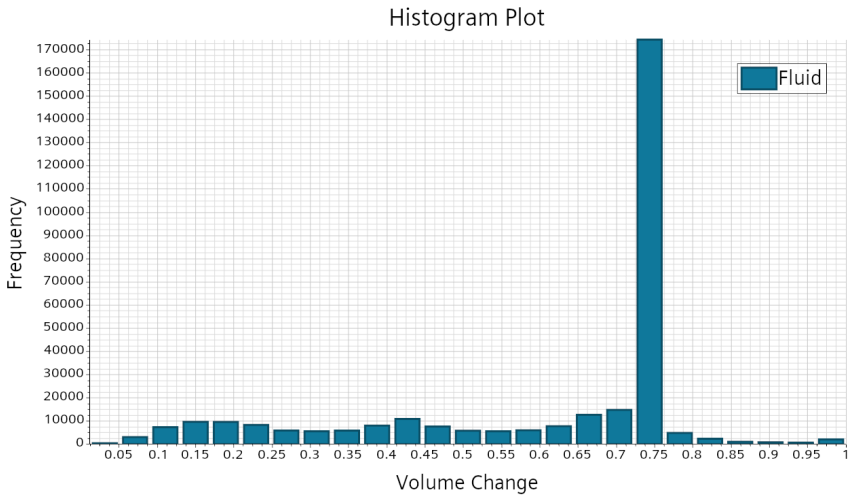

(c) Volume change and frequency of cells

Figure A.2: Quality parameters for Mesh 1. Face validity was 1 for all elements.

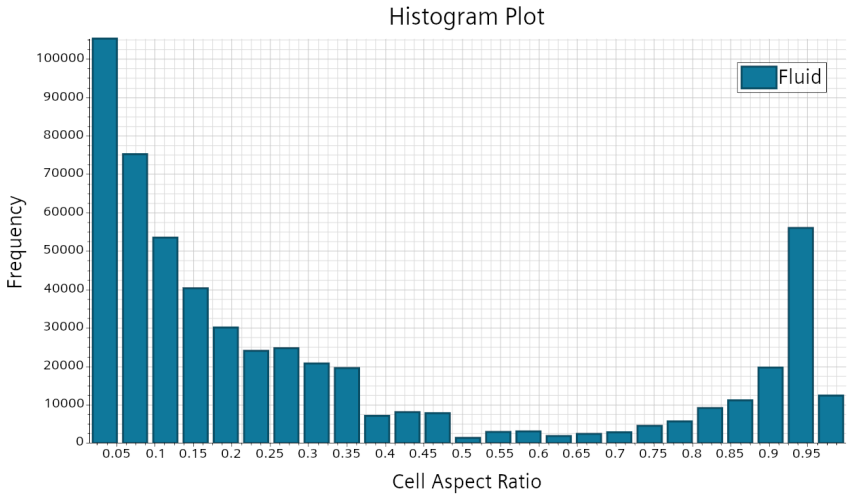

(a) Cell aspect ratio and frequency of cells

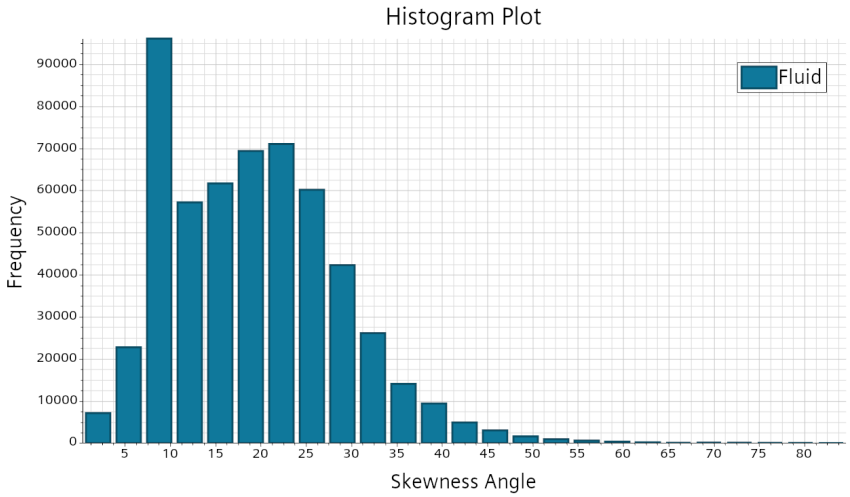

(b) Skewness angle and frequency of cells

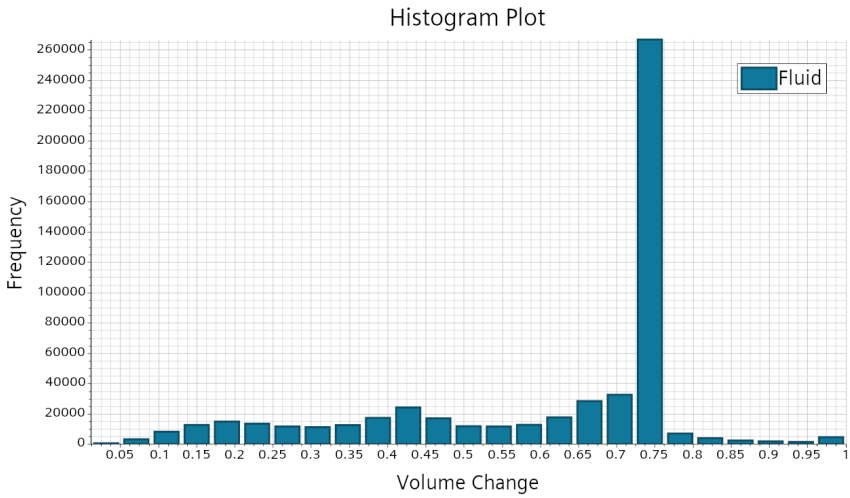

(c) Volume change and frequency of cells

Figure A.3: Quality parameters for Mesh 2. Face validity was 1 for all elements.

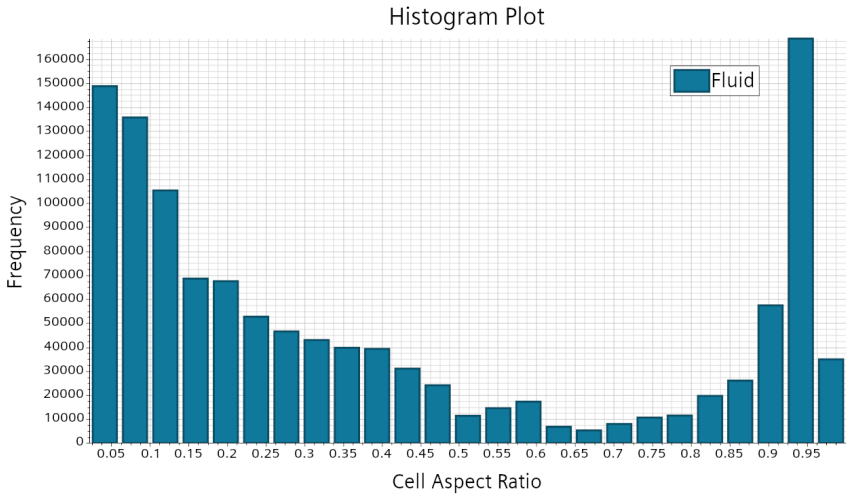

(a) Cell aspect ratio and frequency of cells

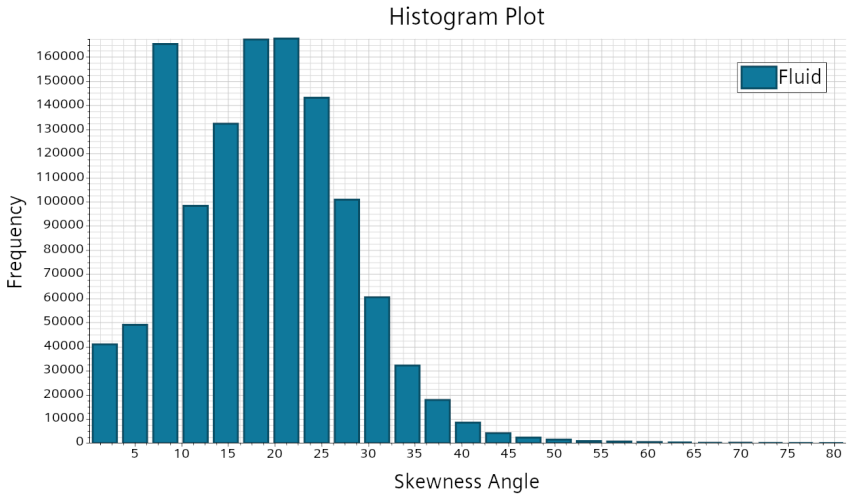

(b) Skewness angle and frequency of cells

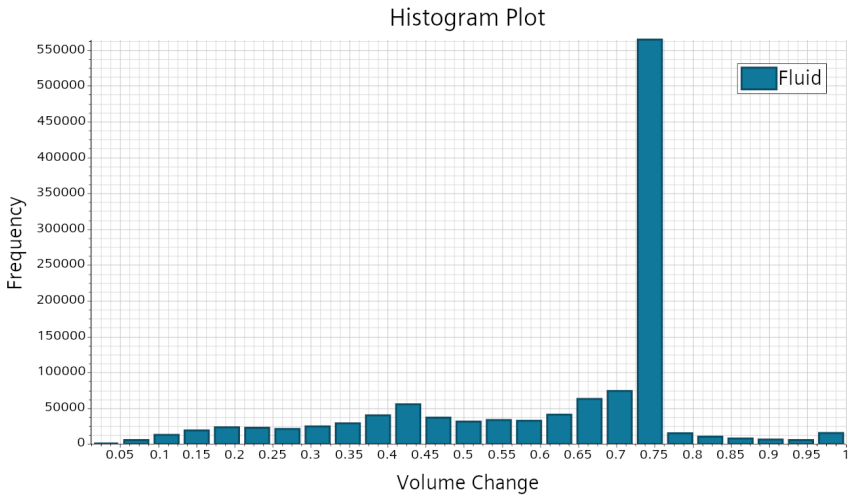

(c) Volume change and frequency of cells

Figure A.4: Quality parameters for Mesh 3. Face validity was 1 for all elements.

DEPARTMENT OF MECHANICS AND MARITIME SCIENCES
CHALMERS UNIVERSITY OF TECHNOLOGY
Gothenburg, Sweden
www.chalmers.se

CHALMERS
UNIVERSITY OF TECHNOLOGY